

Universidade de São Paulo
Instituto de Astronomia, Geofísica e Ciências Atmosféricas

University of St. Andrews
School of Earth and Environmental Sciences

Vinicius Hector Abud Louro

Geophysical, Geochemical and Isotopic Analysis
of the Figueira Branca Suite, Mato Grosso, Brazil.

Análise Geofísica, Geoquímica e Isotópica
da Suíte Figueira Branca, Mato Grosso, Brasil.

São Paulo
2017

Vinicius Hector Abud Louro

Geophysical, Geochemical and Isotopic Analysis
of the Figueira Branca Suite, Mato Grosso, Brazil.

Análise Geofísica, Geoquímica e Isotópica
da Suíte Figueira Branca, Mato Grosso, Brasil.

Tese apresentada ao Departamento de Geofísica do Instituto de Astronomia, Geofísica e Ciências Atmosféricas da Universidade de São Paulo e à School of Earth and Environmental Sciences da University of St. Andrews como requisito parcial para obtenção do título de Doutor em Ciências.

Área de Concentração: Ciências da Terra.
Orientadores: Profa. Dra. Marta Silvia Maria Mantovani e Prof. Dr. Peter Anthony Cawood

São Paulo
2017

LOURO, V.H.A. Geophysical, Geochemical and Isotopic Analysis of the Figueira Branca Suite, Mato Grosso, Brazil.. 2017. 120 f. Tese (Doutorado em Ciências da Terra) – Instituto de Astronomia, Geofísica e Ciências Atmosféricas, Universidade de São Paulo, São Paulo, 2017.

Aprovado em/Approved in:

Banca Examinadora / Examiners

Prof. Dr. _____

Instituição/Institution: _____

Julgamento/Decision: _____

"It ain't about how hard you can get hit,
It's about how hard you can get hit and keep moving forward.
How much you can take and keep moving forward.
That's how winning is done"

Rocky Balboa (2006)

ACKNOWLEDGEMENTS

I would like to thank my supervisors Marta Mantovani and Peter Cawood, my mentor Tony Prave (Oh Captain, my Captain), my partner and friend Vanessa B. Ribeiro, and my good friends in Brazil and in Scotland, who pushed me and kept me going. My big family, especially, for the love, support and care. Thank you to the several professors and professionals who contributed considerably not only to this research, but to teach me science, geology, humility and to never give up.

ABSTRACT

The Figueira Branca Suite is a layered mafic-ultramafic complex in the Jauru Terrane, southwest Amazon Craton. New lithological, geochemical, gamma-ray and potential field data, integrated with geological, isotope and paleomagnetic data are used to characterize this pulse of Mesoproterozoic extension-related magmatism. The Figueira Branca Suite formed through juvenile magma emplacement into the crust at 1425 Ma, coeval with the later stages of the Santa Helena Orogen. In three papers, this suite was studied from microscopic to continental scales. First, the Figueira Branca suite was analysed through thin sections to determine the influence of inaccurate constraints in magnetic and gravity field modelling. Then, the extent of magmatism within the suite was delimited to four bodies to the north of Indiavaí city, MT - Brazil, with potential fields and gamma-ray data. Modelling gravity and magnetic field data indicated that the anomalous sources are close to the surface or outcropping. These intrusions trend northwest over 8 km, with significant remanent magnetization that is consistent with published direction obtained through paleomagnetic data. The increasing enrichment of LREE in the gabbroic bodies of the suite was interpreted as evidence of progressive fractionation of the magma. The emplacement, mineralogy and geochemical signature point towards a back-arc extension tectonic framework in the later stages of the Santa Helena Orogen. The third part of the work consisted on evaluating reconstructions of the Paleo-Mesoproterozoic supercontinent Nuna with magnetic field data. The global magnetic anomaly map, EMAG2, allowed to observe continuity of magnetic lineaments and regimes in domains of similar ages in different cratons (Amazon, Baltica, West Africa and North China). These magnetic features indicated the theory which the magnetic field best supported, and suggested the regional environment where the Jauru Terrane was inserted by the time of the intrusion of the Figueira Branca Suite.

Keywords: Amazon Craton, Mafic Suite, Potential Fields, Geochemistry, Nuna

RESUMO

A Suíte Figueira Branca é um complexo máfico-ultramáfico no Terreno Jauru, sudoeste do Cráton Amazônico. Novos dados litológicos, geoquímicos, de raios gama e de campos potenciais, integrados com dados geológicos, isotópicos e paleomagnéticos, foram utilizados para caracterizar o pulso magmático Mesoproterozóico da suíte vinculado a um ambiente distensivo. A Suíte Figueira Branca foi formada pela intrusão na crosta de um magma juvenil em 1425 Ma, mesma idade dos estágios tardios da orogenia Santa Helena. Em três artigos, esta suíte foi estudada em escalas desde microscópicas a continentais. Primeiramente, a Suíte Figueira Branca foi analisada através de lâminas para determinar a influência da utilização de vínculos errados ou inadequados na modelagem de dados de campos magnéticos e gravimétricos. Em seguida, a extensão do magmatismo pertencente à suíte foi delimitado, via campos potenciais e gamaespectrometria, a quatro corpos ao norte da cidade de Indiavaí, MT - Brasil. A modelagem dos dados de campos gravimétrico e magnético indicaram que as fontes dos sinais geofísicos se encontram em horizontes rasos ou aflorantes. Estas intrusões apresentam um alinhamento noroeste por mais de 8 Km, com magnetização remanente significativa consistentes direções publicadas em estudos paleomagnéticos. O crescente enriquecimento de Elementos de Terras-Raras leves em corpos gabróticos da suíte foi interpretado como evidência de fracionamento progressivo do magma. A intrusão, a mineralogia e a assinatura geoquímica indicaram um ambiente de extensão de retro-arco durante os estágios finais da orogenia Santa Helena. A terceira parte deste trabalho consistiu na avaliação de reconstruções através de dados de campo magnético do supercontinente paleo- a mesoproterozóico Nuna. O mapa global de anomalia magnética, EMAG2, permitiu observar continuidades de lineamentos e regimes magnéticos em domínios de idades similares em diferentes crátons (Amazônico, Báltico, Oeste Africano, do Norte da China). Estas propriedades magnéticas indicaram a teoria que melhor se adequava aos dados de campo magnético, e sugeriram o ambiente regional onde o Terreno Jauru se encontrava na época da intrusão da Suíte Figueira Branca.

Palavras-Chave: Cráton Amazônico, Suíte Máfica, Campos Potenciais, Geoquímica, Nuna

Summary

1. Introduction.....	1
2. Manuscript 1: Effects of inaccurate constraints in magnetic and gravity field modelling	6
Summary	9
1. Introduction.....	9
2. Methodology	10
3. Synthetic Model.....	12
4. Real Case	22
4.1. Geological Context	22
4.2. Data.....	24
4.3. Samples and Thin Sections	26
4.4. Potential Fields Modelling.....	28
5. Discussion.....	34
6. Conclusions.....	36
7. Acknowledgements.....	38
8. References.....	38
3. Manuscript 2: Tectonic insights of the Southwest Amazon Craton from geophysical, geochemical and mineralogical data of Figueira Branca Mafic-Ultramafic Suite, Brazil.....	41
Abstract.....	48
Keywords	47
1. Introduction.....	49

2. Geologic and Tectonic Framework.....	51
3. Data.....	54
4. Results & Discussion.....	56
4.1. Typical Magnetic Field Signature and Bodies Associated with the Suite.....	56
4.2. Gravity Field.....	60
4.3. Mineralogy and Geochemical Signature.....	61
4.4. Magnetic and Gravity Modelling.....	66
5. Conclusions.....	72
6. Acknowledgements.....	73
7. References.....	73
4. Manuscript 3: Magnetic Amazon: where was the Amazon Craton in Nuna?.....	78
Abstract.....	83
Keywords.....	83
1. Introduction.....	84
2. Geology of the Cratons.....	87
2.1. Amazon Craton.....	87
2.2. West African Craton.....	88
2.3. Baltic Craton.....	89
2.4. North China Craton.....	91
3. Methodology.....	92
3.1. Data.....	92

3.2.	Magnetic Field Techniques.....	92
4.	Magnetic Signatures.....	95
4.1.	Amazon Craton	96
4.2.	West African Craton	98
4.3.	Baltic Craton	100
4.4.	North China Craton.....	102
5.	Results.....	104
5.1.	Mertanen and Pesonen (2012)	104
5.2.	Pisarevsky et al. (2014).....	107
5.3.	Pehrsson et al. (2015).....	109
6.	Discussion	112
7.	Conclusions.....	113
8.	Acknowledgements.....	114
9.	References.....	115
5.	Conclusions.....	121
6.	References.....	125
	Attachment 1	126

1. Introduction

How much a single and considerably small intrusive suite can tell with geology and geophysics? How much can it tell about common mistakes done even by specialists in geophysical modelling? What can it reveal about its own features and history? About the environment that hosts it and, ultimately, lead to better understand the Earth evolution? This thesis brings a set of three correlate studies seeking to answer these questions.

The studies that compose this thesis evaluate the Figueira Branca Mafic-Ultramafic Suite, from microscopic to continental scale. These studies were submitted to peer-reviewed journals, and are currently under review. The first manuscript discusses the influence of inaccurate constraints in magnetic and gravity field modelling, and why analysing samples microscopically is not only recommendable, but of major importance for a reliable geophysical modelling. The Figueira Branca Suite was used as background for this analysis, given the variable condition and petrophysical properties of its samples.

The Amazon Craton is divisible into six geochronological provinces: the Archean Central Amazon, and the Proterozoic provinces of Maroni-Itacaiúnas, Ventuari-Tapajós, Rio Negro-Juruena, Rondonian-San Ignácio and Sunsás-Aguapeí (Fig. 1.1a) (Tassinari & Macambira, 1999; Teixeira et al., 2010). The southern portion of the Rio Negro-Juruena (1.78 – 1.55 Ga) province includes the Jauru Terrane (1.78 – 1.40 Ga), which contains Paleoproterozoic basement rocks and the Mesoproterozoic Cachoeirinha and Santa Helena orogens (Fig. 1.1b) (Bettencourt et al., 2010). The Alto Jauru Group, part of the Paleoproterozoic basement of the Jauru Terrane, hosts the Figueira Branca Mafic-Ultramafic Intrusive Suite.

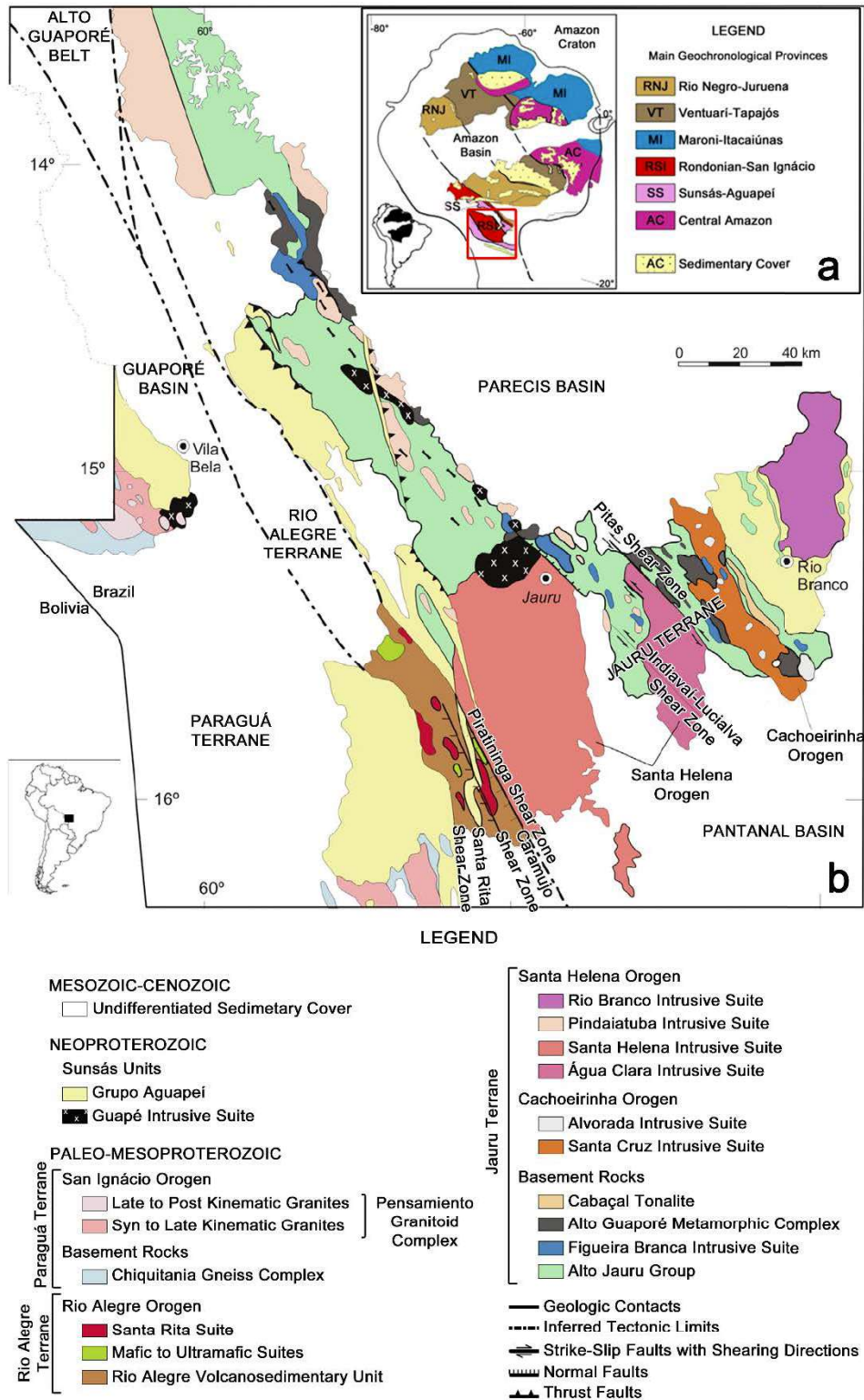


Fig. 1.1 - (a) Main geochronological provinces of Amazon Craton (Bettencourt et al., 2010). The red polygon delimits the area of Fig. 1b. (b) Southwest of the Rio Negro-Juruena and Rondonian-San Ignácio provinces of the Amazon Craton. The Figueira Branca Suite is represented in dark blue.

The Figueira Branca Intrusive Suite is a 1425 ± 8 Ma layered mafic-ultramafic complex composed from bottom to top of dunite, pyroxenite, gabbro-norite, anorthosite, thin layers of troctolite, and olivine-gabbro (Teixeira et al., 2011). Isotope data from its southern body indicate a juvenile source that crystallized during the later stages of the Santa Helena Orogeny (Tassinari, Bettencourt, Geraldés, Macambira, & Lafon, 2000; Teixeira et al., 2016; Teixeira et al., 2011).

The second work describes the Figueira Branca Intrusive Suite geophysical signature through potential field models, and geochemically with major, trace and Rare-Earth element analyses. It explores the magnitude of the magmatism that generated the suite, analysing the terrane that hosts it, the parental magma, and the tectonic framework involved. The potential field models displayed a northwest-southeast elongation in four bodies immediately to the north of Indavaí city. Geochemical data confirmed the extensional setting proposed by Teixeira et al. (2011) through isotope data.

The third part of the thesis develop a continental scale analysis of the Amazon Craton by the time of the development of the Santa Helena Orogen and intrusion of the Figueira Branca Suite, from 1.6 to 1.4 Ga (Fig. 1.1b). The location of the Amazon Craton during the Paleo- to Mesoproterozoic supercontinent Nuna gave insights of the tectonic framework that the craton was subjected during the intrusion of the Figueira Branca Suite. This location is currently under debate, so as the configuration of the Nuna supercontinent. Three reconstructions of Nuna were chosen to evaluate the position of the Amazon Craton, of Mertanen and Pesonen (2012), which is based on paleomagnetic data; of Pisarevsky, Elming, Pesonen, and Li (2014), based on paleomagnetic and geological constraints; and of Pehrsson, Eglington, Evans, Huston, and Reddy (2015) who integrated paleomagnetic and geological data with ore deposit features (Fig. 1.2). Using magnetic field data, it was possible to recognize magnetic regimes and lineament patterns in the Amazon Craton, and nearby blocks according with the reconstructions. This

dataset was the basis to evaluate which theory was better supported by the magnetic field. The better supported theory, by consequence, proportionated evidences about what was occurring with the southwest of the Amazon Craton when the Figueira Branca Suite intruded the Jauru Terrane.

Nuna Reconstructions

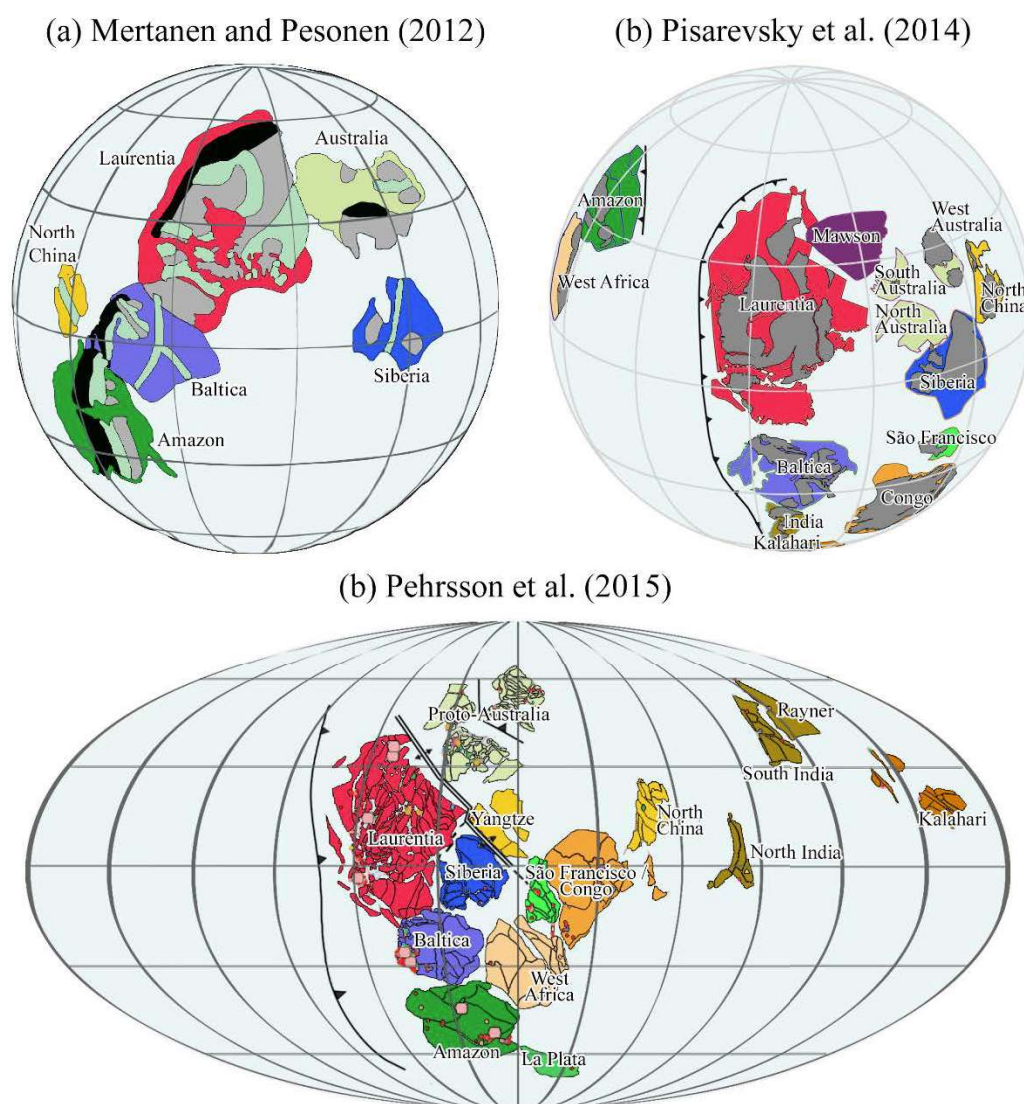


Fig. 1.2 - Reconstructions of Nuna proposed by (a) Mertanen and Pesonen (2012), (b) Pisarevsky et al. (2014), and (c) Pehrsson et al. (2015).

The scale of the problems and the proposed answers increase from the first to the third part of the thesis. The three manuscripts that compose this thesis were submitted to the journals Tectonophysics, Geophysical Journal International and Precambrian Research. The final chapter presents the major conclusions obtained through the results generated, arguing about the questions raised here.

In parallel to this project, the PhD student worked in different projects and published as author and co-author four papers. A fifth paper was submitted and is currently under review. The published and submitted papers are available in the Attachment 1 of this thesis.

2. Manuscript 1: Effects of inaccurate constraints in magnetic and gravity field modelling

Starting in small scales, this chapter presents the importance of not only having constraints for modelling, but having them accurate. Measuring the properties that are going to be modelled is the most common procedure to define constraints for modelling. However, simple measurements without a deeper mineralogical analysis can produce inaccurate constraints and compromise the modelling. This manuscript shows how inaccurate magnetic susceptibilities and densities influence in the result of a joint magnetic and gravity modelling using two datasets: one synthetic, to observe the effective difference between using the correct and the inaccurate constraints; and one real dataset, using the Indiavaí anomaly (the southern body of the Figueira Branca Suite) as background for the analysis.



Effects of inaccurate constraints in magnetic and gravity field modelling

Journal:	<i>Geophysical Journal International</i>
Manuscript ID	GJI-S-17-0112
Manuscript Type:	Research Paper
Date Submitted by the Author:	31-Jan-2017
Complete List of Authors:	Louro, Vinicius; Instituto de Astronomia, Geofísica e Ciências Atmosféricas da Universidade de São Paulo, Geophysics Department; University of St. Andrews, Department of Earth Sciences Cawood, Peter; University of St. Andrews, Department of Earth Sciences Mantovani, Marta; Instituto de Astronomia, Geofísica e Ciências Atmosféricas da Universidade de São Paulo, Geophysics Department
Keywords:	Gravity anomalies and Earth structure < GEODESY and GRAVITY, Magnetic anomalies: modelling and interpretation < GEOMAGNETISM and ELECTROMAGNETISM, Numerical modelling < GEOPHYSICAL METHODS, Magnetic mineralogy and petrology < GEOMAGNETISM and ELECTROMAGNETISM

1
2
3
4
5
6
7
8
9
10
11
12
13
14
15
16
17
18
19
20
21
22
23
24
25
26
27
28
29
30
31
32
33
34
35
36
37
38
39
40
41
42
43
44
45
46
47
48
49
50
51
52
53
54
55
56
57
58
59
60

Effects of inaccurate constraints in magnetic and gravity field modelling

Vinicius Hector Abud Louro^{1,2}, Peter Anthony Cawood², Marta Silvia Maria Mantovani¹

¹ Instituto de Astronomia, Geofísica e Ciências Atmosféricas, Universidade de São Paulo, São Paulo, Brazil.

² Department of Earth and Environmental Sciences, University of St. Andrews, St. Andrews, KY16 9AL, UK.

E-mails: vilouro@usp.br, pac20@st-andrews.ac.uk, msmmanto@usp.br

Corresponding author: Vinicius Hector Abud Louro. **E-mail:** vilouro@usp.br

Date of Submission: 29 January 2017

ORCID:	Louro, V. H. A.:	0000-0003-3430-4507
	Cawood, P. A.:	0000-0003-2357-0068
	Mantovani, M. S. M.:	n/a

1
2
3 22 ***Summary***
4
5 23
6
7
8 24

9
10 25 Modelling potential fields is a common procedure in geophysical exploration. The nature and
11 26 type of data used to constrain the model determine the feasibility and viability of the output and hence
12 27 the ability of the model to provide a valid representation of reality. This paper presents a set of
13 28 models, from synthetic and real cases that were used to investigate how poorly defined or inaccurate
14 29 constraints affect the results of potential field modelling. The staged-inversion methodology was used
15 30 in the investigation, and four approaches were modelled for synthetic data and two approaches for the
16 31 real data. The real data assessed a mafic-ultramafic intrusion in the southwest Amazon Craton.
17 32 Unsurprisingly, the results indicate that the use of the correct magnetic susceptibility and density
18 33 values, and keeping them fixed during staged inversion produces the best model. However, when only
19 34 limited data are available to constrain the modelling, acceptable results can still be achieved if the
20 35 process is rigorously executed.
21
22
23
24
25
26
27
28
29
30
31
32
33
34
35
36

37 37 ***1. Introduction***
38
39
40
41 39

42 40 Modelling of data is a common component of most geophysical studies and facilitates the
43 41 resolution of poorly, or non-, exposed geological bodies and structures. The quality of the geophysical
44 42 model (i.e. its ability to accurately represent a body or structure) is highly dependent on the quality of
45 43 data constraints. The constraints can be geological, geophysical, geochemical, or any kind of
46 44 information that limits the possibilities and/or ambiguities in the geophysical methodology. Here we
47 45 discuss the effects that inaccurate magnetic susceptibilities and densities can cause in gravity and
48 46 magnetic field modelling, respectively.
49
50
51
52
53
54
55
56
57
58
59
60

46 47 To analyse the effects of inaccurate constraints, we have worked with synthetic and real data
47 48 sets. The constraints used for the modelling were obtained from potential field data, hand samples and

1
2
3 48 thin-sections. For potential field models, the constraints were the lateral extent of a body, the depth to
4
5 49 the top of the source of the signal and, in the magnetic field case, estimates of the total magnetization.
6
7 50 For the real data sets, hand samples and thin-sections provided additional constraints.
8

9
10 51 For assessment of synthetic models using gravity and magnetic data we used two sets of
11
12 52 parameters for each case. The differences between the sets were the initial magnetic susceptibility and
13
14 53 density. In one set, we used the correct values, whereas in the second set, we used half the actual
15
16 54 value for each property (e.g. correct density contrast: 0.24 g/cm^3 , half the value: 0.12 g/cm^3). In the
17
18 55 real world, smaller values for magnetic susceptibility and density can reflect weathering, a common
19
20 56 effect on rock units, especially in tropical and equatorial areas, and alteration.
21

22
23 57 The real cases scenarios presented in this study are for the Indiavaí igneous body, from the
24
25 58 Figueira Branca mafic-ultramafic suite, Mato Grosso, Brazil. The suite lies on the southwest of the
26
27 59 Amazon Craton. Two situations were considered. In the first the available data included potential field
28
29 60 information, hand samples, and magnetic susceptibility and density measurements, which is similar to
30
31 61 parameters routinely available in the processing and modelling of potential fields. In a second
32
33 62 situation, thin-section data were used to further constraint the input data.
34

35 63

36 64

37 65 **2. Methodology**

38 66

39
40
41
42
43
44
45 67 The magnetic modelling used a fixed direction of total magnetization, estimated through the
46
47 68 MaxiMin method (Fedi *et al.* 1994). Cordani and Shukowsky (2009) implemented the MaxiMin
48
49 69 technique in a MATLAB algorithm. This algorithm selects 30 pairs of inclination and declination
50
51 70 angles and performs RTP filtering from the residual magnetic field with each pair. The resulting grid
52
53 71 that presents the most negative values is discarded, and a new iteration is initiated. This process is
54
55 72 repeated until the 30 pairs of values do not differ from each other by more than a predefined error (5°
56
57 73 in this work) or the process reaches a predefined maximum number of iterations (4000). Lateral limits
58
59
60

1
2
3 74 of the body (real and synthetic) were defined by their gradient of horizontal derivatives of the
4
5 75 magnetic field reduced to the pole. These fields were preferred over the gravity fields due the larger
6
7 76 amount, and better spaced, magnetic data than the gravity fields. The depths to the top of the potential
8
9 77 field anomaly sources, in the synthetic cases, were estimated using Euler Deconvolution (Reid *et al.*
10
11 78 1990). In the real case, the depth estimation was not necessary because the Indiavaí igneous body
12
13 79 outcrops, therefore the depth to the top of the initial model was considered zero.

14
15
16 80 The modelling was performed using the staged-inversion methodology (Foss 2006). The
17
18 81 modelling took two phases: one using a block body as the initial model, and one using prisms sliced
19
20 82 from the body modelled in the first phase as the initial model. The prisms were parallel and centred on
21
22 83 the north-south surveyed lines, with a fixed 500 m width in east-west direction. The steps of the first
23
24 84 phase of staged-inversion consisted of: (1) varying the amplitude of the total magnetization and depth
25
26 85 extent of the block model; (2) varying the amplitude of the total magnetization, depth extent and
27
28 86 horizontal position; (3) varying the amplitude of the total magnetization, depth extent, horizontal
29
30 87 position and vertex movements in the north-south direction; (4) varying the parameters of the
31
32 88 previous stage plus the position of the vertices of the model in east-west direction; and (5) varying the
33
34 89 previous parameters and the magnetic susceptibility (in the magnetic inversion), or the density (in the
35
36 90 gravity inversion). In the second phase, the modelling using the prisms had two differences: instead of
37
38 91 varying the depth extent in all stages, the vertices were allowed to vary their positions in vertical
39
40 92 direction, and stage (4) was skipped.

41
42
43 93 The quality of the modelling was assessed by the “inversion confidence” (Pratt 2006), where
44
45 94 the confidence that the modelled body exists in the studied area varies from 0 to 100%. This interval
46
47 95 of confidence is expressed by the root mean square value (rms-error).

48
49 96

50
51 97

52
53 98

54
55 99

56
57 100

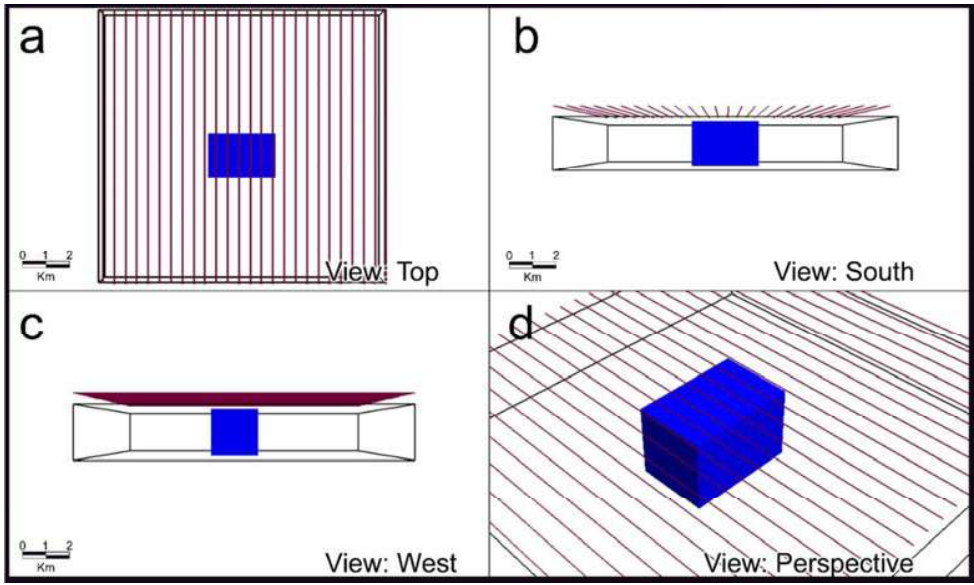
58
59 101

60
102

1
2
3
4
5
6
7
8
9
10
11
12
13
14
15
16
17
18
19
20
21
22
23
24
25
26
27
28
29
30
31
32
33
34
35
36
37
38
39
40
41
42
43
44
45
46
47
48
49
50
51
52
53
54
55
56
57
58
59
60

99 **3. Synthetic Model**

100
101 A synthetic block model was created and it's magnetic and gravity fields calculated (Fig. 1,
102 Table 1). This model presents a significant remanent magnetization, and it is exposed to an
103 environment of negligible magnetization (0.0001 S.I.) and density of 2.67 g/cm³. The calculated fields
104 were then the starting point for evaluating the effects of inaccurate constraints using the staged-
105 inversion methodology.



107
108 Fig. 1 – Synthetic model used in the experiments in the view: (a) top, (b) south, (c) west, and (d)
109 perspective. The model parameters are described in Table 1.

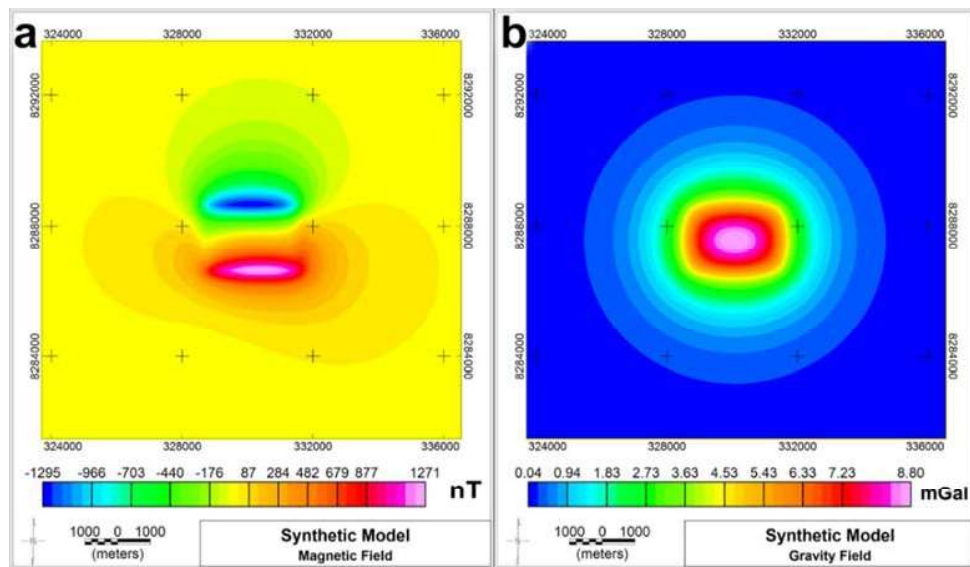
114 Table 1 – Parameters of the synthetic model. In the magnetization fields, I refers to Inclination, D to
 115 Declination and J to the Intensity.

Shape	Block		
Size (E-W) (m)	3000		
Size (E-W) (m)	2000		
Depth Extent (m)	2000		
Depth (m)	200		
Density (g/cm ³)	2.94		
Magnetic Susceptibility (S.I.)	0.05		
Magnetization	Inclination	Declination	Intensity
Induced Magnetization	-11.3°	346.9°	0.95 A/m
Remanent Magnetization	49.6°	199.4°	4.39 A/m
Total Magnetization	56°	213°	3.8 A/m

116

117 Four experiments were undertaken to model the synthetic fields (Fig. 2). In two experiments
 118 the magnetic susceptibility and density were fixed, discarding step (5) of the staged-inversion,
 119 whereas for the other two experiments, these parameters were varied. In each of the two sets of
 120 experiments, one experiment started with the correct values of magnetic susceptibility and density,
 121 and the other started with half the actual contrast of both parameters with the background (Fig. 3).

122



123

124 Fig. 2 – (a) Magnetic and (b) gravity fields of the synthetic body.

125

126

127

128

129

130

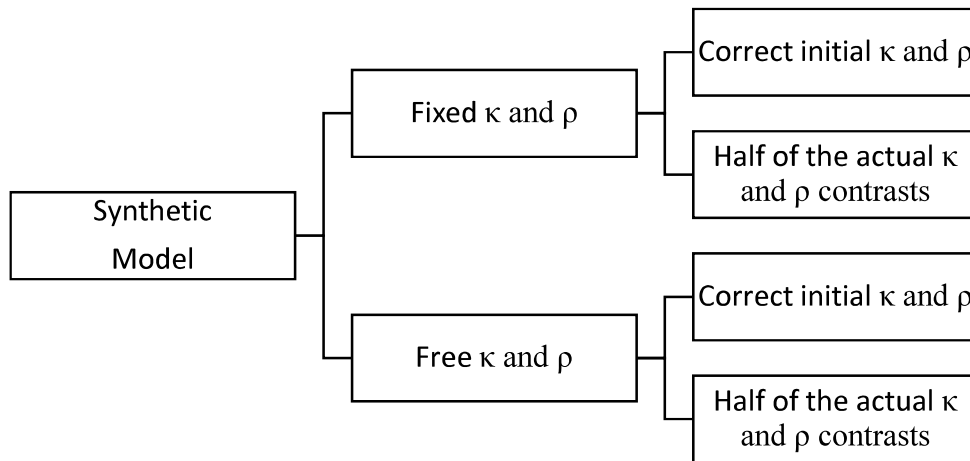
131

132

133

134

125



126

127 Fig. 3 – Scheme of the synthetic experiments treating the role of the magnetic susceptibility and
 128 densities in the staged-inversion. κ represents the magnetic susceptibility and ρ the density.

129

130 The MaxiMin method produced the inclination 55.6° and declination 201.9° ($\alpha_{95\%}=5.0^\circ$),
 131 which are 0.22% and 3.25% different respectively, from the actual total magnetization direction. The
 132 field reduced to the magnetic pole showed good approximation to the shape of the body (Fig. 4a), and
 133 was positive and centered over the location of the anomaly. The lateral limits obtained with the
 134 horizontal gradient of the RTP-filtered field showed adequate compatibility with the model lateral
 135 limits (Fig. 4b). The depths obtained through Euler Deconvolution varied from 19 m to 362 m, but
 136 had the majority of solutions around 200 m (Fig. 4c and d) consistent with the depth to the top of the
 137 original model (Table 1). The structural index used was 0, with the window size of 375 m. Table 2
 138 shows the initial model parameters used in the staged-inversion.

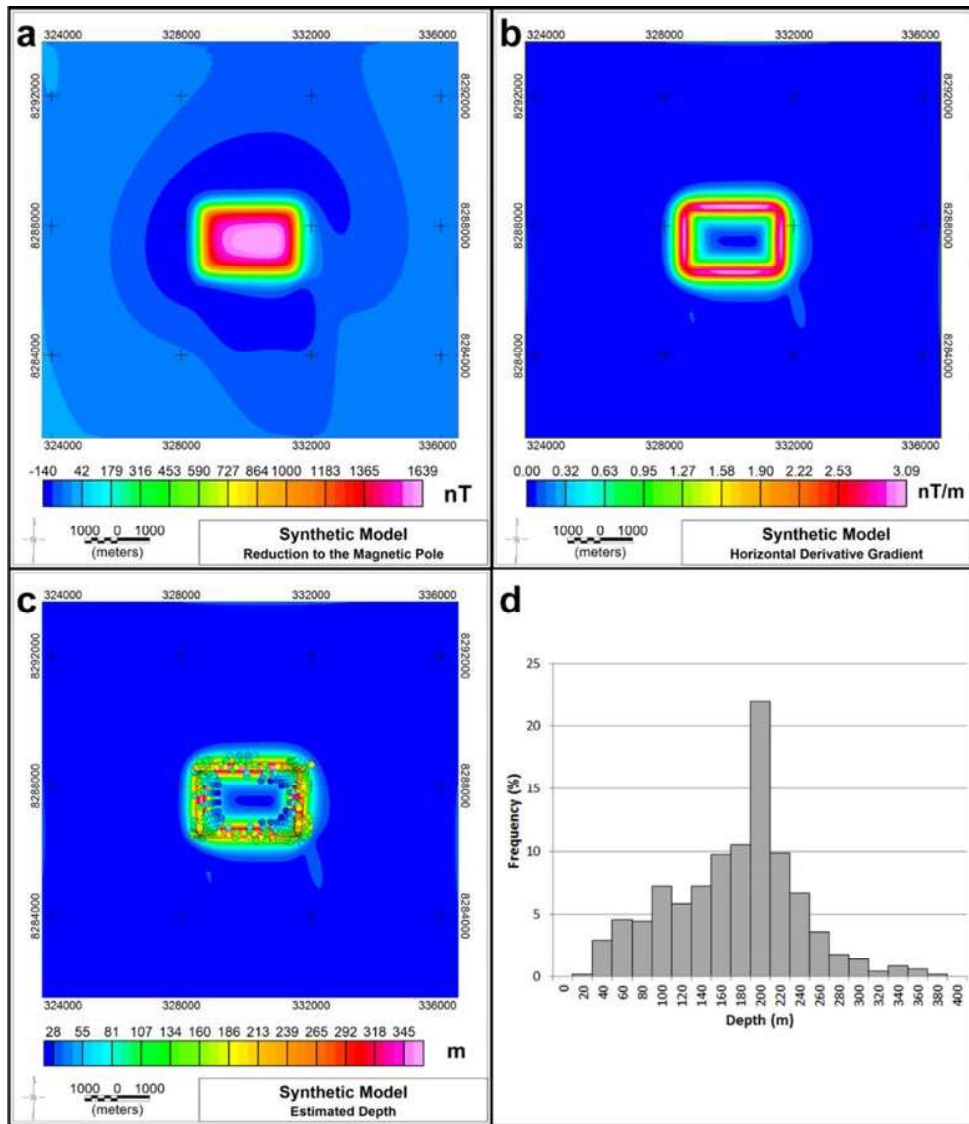


Fig. 4 – (a) RTP field, (b) horizontal derivative gradient, (c) depths estimated with the Euler Deconvolution, and (d) histogram of the solutions of the Euler Deconvolution.

139

140

141

142

143

144

145

1
2
3 146 Table 2 – Initial parameters used in the synthetic data modelling. In the magnetization fields, I refers
4
5 147 to inclination, D to declination and J to the intensity.
6
7

8 Shape	Tabular		
9 Size (E-W) (m)	3000		
10 Size (E-W) (m)	2000		
11 Depth Extent (m)	1000		
12 Depth (m)	200		
13 Density (g/cm^3)	2.94	2.805 (half contrast)	
14 Magnetic Susceptibility (S.I.)	0.05	0.025 (half contrast)	
15 Magnetization	Inclination	Declination	Intensity
16 Induced	-11.3°	346.9°	0.5 A/m
17 Remanent	43.2°	186.2°	1.3 A/m
18 Total	55.6°	201.9°	1.0 A/m

19 148
20
21
22 149 The inversions showed low residuals: 4.0% in the worst case (Table 3). However, low
23
24 150 residuals do not necessarily mean that an inversion was successful. The inverted models vary
25
26 151 significantly in their physical properties (when allowed), shape and volume (Fig. 5). Model 1 (Fig. 5a
27
28 152 and b), in which susceptibility and density were kept fixed with the correct values, reproduced the
29
30 153 original model with reduced errors. The difference between the volume of Model 1 and the original
31
32 154 model was 1.48 km^3 (12.3%) and the top of the model was kept around 200 m below the surface. The
33
34 155 magnetization vectors differed less than 8° in direction and 0.1 A/m in intensity from the original,
35
36 156 with an $\alpha_{95\%}$ of 1.27° for the remanent magnetization vector.
37
38

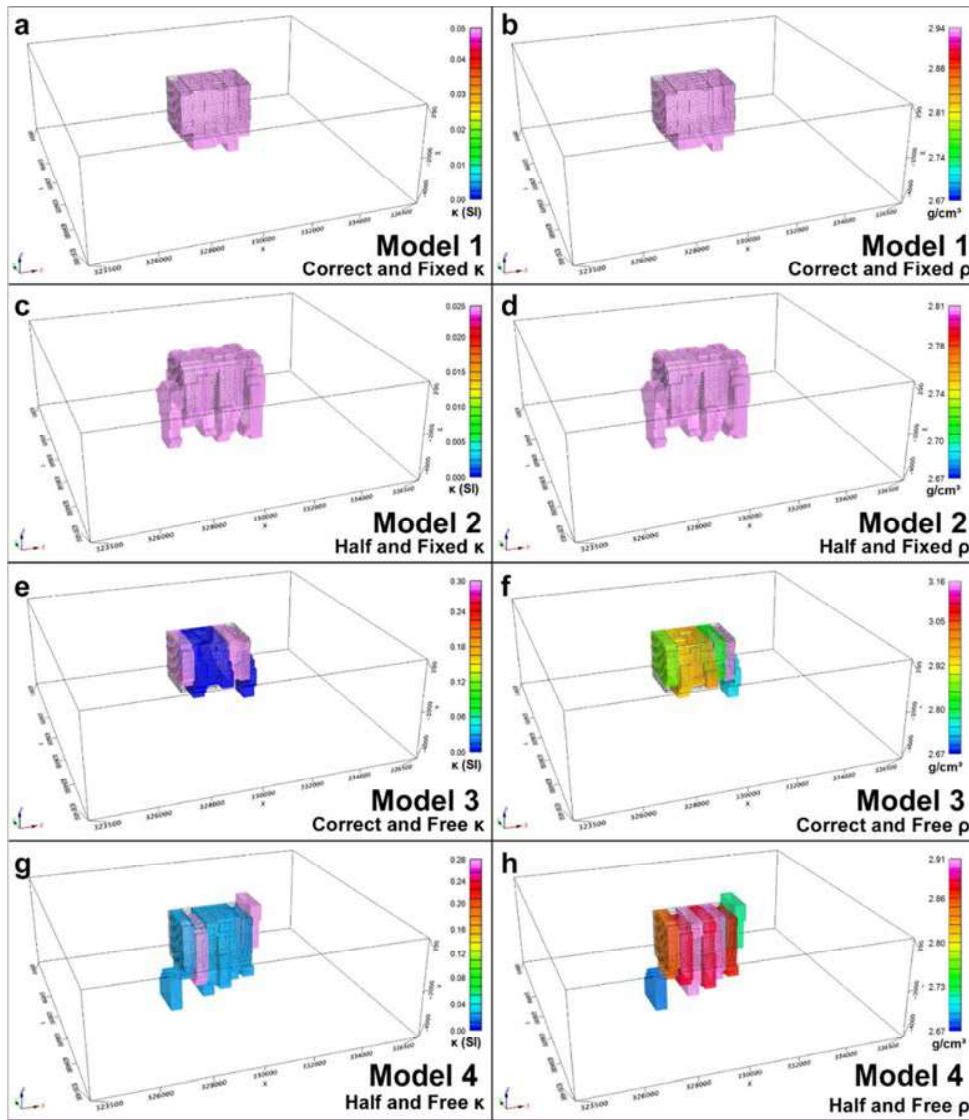
39 157 Model 2 (Fig. 5c and d), with magnetic susceptibility of 0.025 and density of 2.81 g/cm^3
40
41 158 fixed, achieved directions of the magnetic vectors as close to the original model as Model 1 (Table 3,
42
43 159 Fig 5a and b). Other features however, were not as well-resolved as in Model 1. The volume of Model
44
45 160 2 was 15.74 km^3 larger than the actual volume, and the depth extent overestimated to compensate the
46
47 161 reduced susceptibility and density (Fig. 5c and d). The block model had its vertex spread in the east-
48
49 162 west direction to an area larger than the original model after the first inversion process. This spread
50
51 163 resulted in the addition of two more sections than necessary to represent the original model, and
52
53 164 resulted in the much larger volume.
54
55

56 165
57
58
59
60

166 Table 3 – Inversion results for the models 1 to 4. κ and ρ represent the magnetic susceptibility and the
 167 density, respectively.

Geophysical Models			
Background (Host-rock)			
Avg Mag Suscep	0.001 (SI)		
Avg Density	2.67 g/cm ³		
Model 1: Fixed κ and ρ – Correct κ and ρ			
Avg Mag Suscep	0.05 (SI)	Total Volume	13.48 km ³
Avg Density	2.94 g/cm ³	Difference of Volume	1.48 km ³
Magnetic and Gravity Fields Inversions			
Magnetization	Induced	Total ($\alpha_{95\%} = 5.0^\circ$)	Remanent ($\alpha_{95\%} = 1.27^\circ$)
Inclination (°)	-11.6	55.6	48.4
Declination (°)	346.9	201.9	191.5
Intensity (A/m)	0.9	3.8	4.4
RMS-Mag (%)	0.7	# of Points	78832
RMS-Grav (%)	0.5	# of Points	78832
Model 2: Fixed κ and ρ – Half of the correct κ and ρ			
Avg Mag Suscep	0.025 (SI)	Total Volume	27.74 km ³
Avg Density	2.81 g/cm ³	Difference of Volume	15.74 km ³
Magnetic and Gravity Fields Inversions			
Magnetization	Induced	Total ($\alpha_{95\%} = 5.0^\circ$)	Remanent ($\alpha_{95\%} = 9.4^\circ$)
Inclination (°)	-11.6	55.6	49.1
Declination (°)	346.9	201.9	192.4
Intensity (A/m)	1.3	2.1	2.5
RMS-Mag (%)	1.6	# of Points	78832
RMS-Grav (%)	4.0	# of Points	78832
Model 3: Free κ and ρ – Correct κ and ρ			
Avg Mag Suscep	0.13 (SI)	Total Volume	12.98 km ³
Avg Density	2.92 g/cm ³	Difference of Volume	1.98 km ³
Magnetic and Gravity Fields Inversions			
Magnetization	Induced	Total ($\alpha_{95\%} = 5.0^\circ$)	Remanent ($\alpha_{95\%} = 13.9^\circ$)
Inclination (°)	-11.6	55.6	38.9
Declination (°)	346.9	201.9	182.7
Intensity (A/m)	2.5	3.5	5.4
RMS-Mag (%)	1.5	# of Points	78832
RMS-Grav (%)	2.1	# of Points	78832
Model 4: Free κ and ρ – Half of the correct κ and ρ			
Avg Mag Suscep	0.09 (SI)	Total Volume	19.45 km ³
Avg Density	2.81 g/cm ³	Difference of Volume	7.45 km ³
Magnetic and Gravity Fields Inversions			
Magnetization	Induced	Total ($\alpha_{95\%} = 5.0^\circ$)	Remanent ($\alpha_{95\%} = 12.2^\circ$)
Inclination (°)	-11.6	55.6	40.3
Declination (°)	346.9	201.9	183.7
Intensity (A/m)	3.1	2.7	3.9
RMS-Mag (%)	1.0	# of Points	78832
RMS-Grav (%)	1.1	# of Points	78832

1
2
3 168 The intensities of the magnetization vectors of Model 2 (Fig. 5c and d) were affected by the
4
5 169 change in the magnetic susceptibility, from 0.9 A/m to 1.3 A/m in the induced magnetization and
6
7 170 from 4.4 A/m to 2.5 A/m in the remanent magnetization. Changing the induced and remanent
8
9 171 magnetizations caused the decrease in the total magnetization intensity from 3.8 A/m to 2.1 A/m.
10
11
12 172



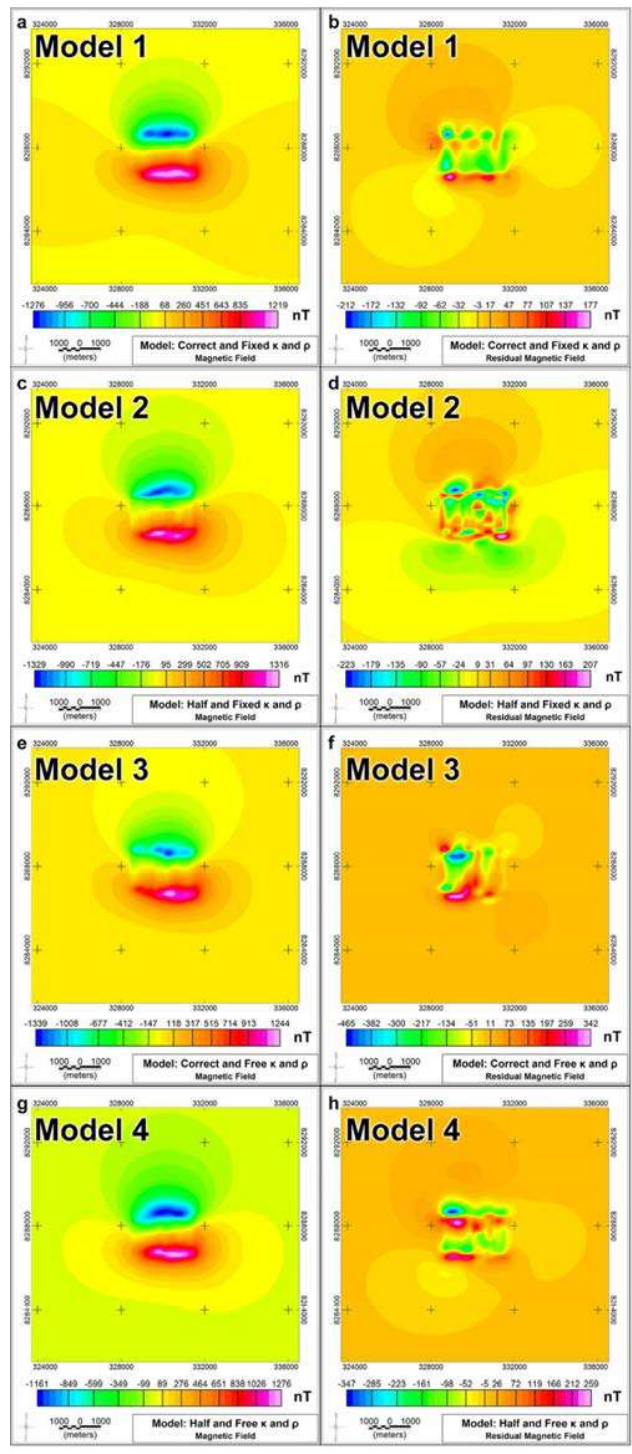
173
174 Fig. 5 – Perspective views of the modelled bodies, where (a), (c), (e) and (g) shows the magnetic
175 susceptibility models, and (b), (d), (f) and (h) the density models. The black wireframe model in each
176 of the models represents the original model (Fig. 1).

1
2
3 177 The inversion of Model 3 (Fig. 5e and f) started with the correct properties (magnetic
4
5 178 susceptibility and density), and the inversion of Model 4 (Fig. 5g and h) with magnetic susceptibility
6
7 179 of 0.025 (S.I.) and density of 2.81 g/cm³. These features were allowed to vary during the inversion.
8
9 180 The result for Model 3 was a body with volume and shape close to the original model (1.98 km³
10
11 181 larger, Fig. 5e and f). In the Model 4 inversion (Fig. 5g and h), a 7.45 km³ higher disparity to the
12
13 182 original model was found. As in Model 2, the lateral spread of the block model after the first inversion
14
15 183 process took to the creation of more north-south sections than necessary in models 3 (1 section) and 4
16
17 184 (2 sections). In both cases, the additional sections were displaced to shallower or much deeper
18
19 185 positions than the remaining sections (Fig. 5e to h). The additional section in Model 3, displaced to a
20
21 186 deeper horizon, had significantly reduced magnetic susceptibility and density, making its contribution
22
23 187 to the gravity and magnetic fields insignificant (Figs. 6 and 7).

24
25
26 188 In Model 4 (Fig. 5g and h), the western additional section had the same behaviour as the
27
28 189 additional section of Model 3 (Fig. 5e and f), whereas the eastern additional section was displaced to
29
30 190 shallower depth. The easternmost additional section, and the second westernmost section, of Model 4
31
32 191 had increased magnetic susceptibility to 0.30 (S.I.), which caused the decrease of magnetic
33
34 192 susceptibility in the remaining sections to compensate the field. The additional eastern section had a
35
36 193 decrease in density, diminishing its contribution to the gravity field, whereas the rest of the sections
37
38 194 showed minimal variation near the density value of the original model.

39
40
41 195
42
43
44
45
46
47
48
49
50
51
52
53
54
55
56
57
58
59
60

1
2
3
4
5
6
7
8
9
10
11
12
13
14
15
16
17
18
19
20
21
22
23
24
25
26
27
28
29
30
31
32
33
34
35
36
37
38
39
40
41
42
43
44
45
46
47
48
49
50
51
52
53
54
55
56
57
58
59
60

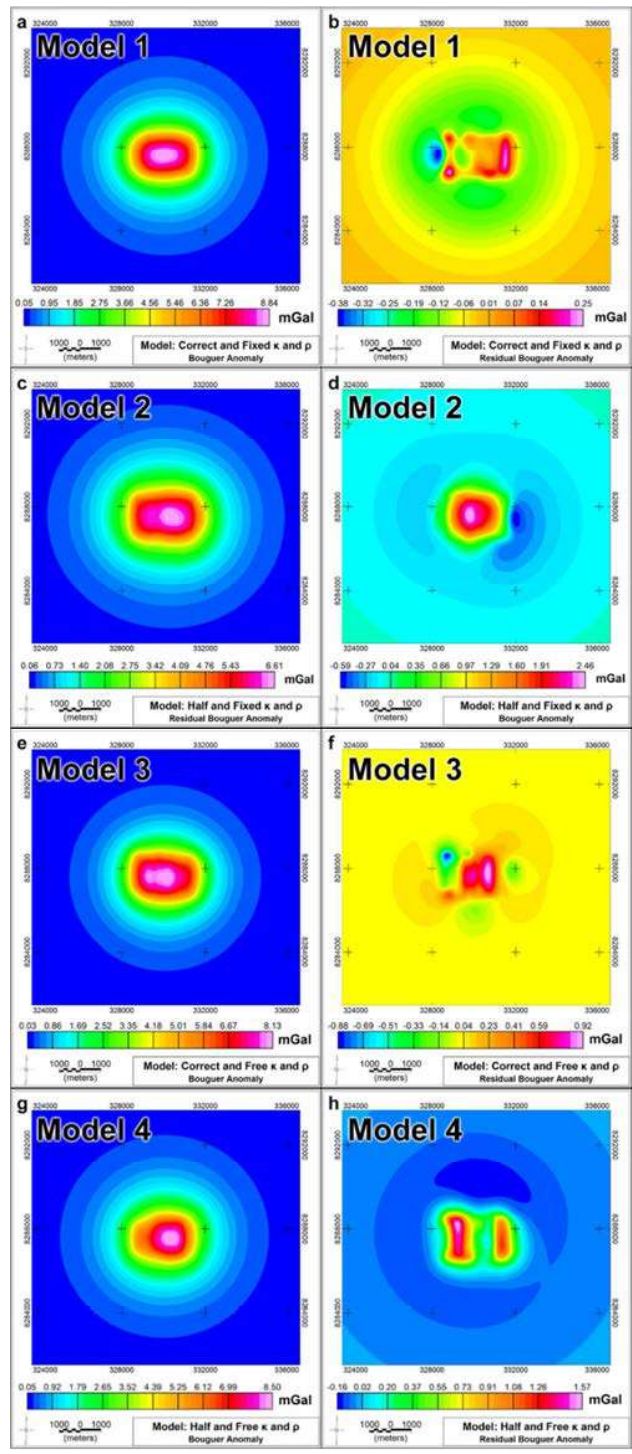


196

197 Fig. 6 – Magnetic and residual magnetic fields, respectively, of Model 1 (a and b), Model 2 (c and d),

198 Model 3 (e and f), and Model 4 (g and h).

1
2
3
4
5
6
7
8
9
10
11
12
13
14
15
16
17
18
19
20
21
22
23
24
25
26
27
28
29
30
31
32
33
34
35
36
37
38
39
40
41
42
43
44
45
46
47
48
49
50
51
52
53
54
55
56
57
58
59
60



199

200 Fig. 7 – Gravity and residual gravity fields, respectively, of Model 1 (a and b), Model 2 (c and d),

201 Model 3 (e and f), and Model 4 (g and h).

1
2
3 202 The distribution of magnetic susceptibilities, and as a consequence magnetization, were
4
5 203 severely affected in both models 3 and 4 (Fig. 5e to h). Higher magnetic susceptibilities and
6
7 204 magnetizations were concentrated in three (Model 3, Fig. 5e) and two (Model 4, Fig. 5g) north-south
8
9 205 sections. This concentration caused significant decrease in physical properties in the other sections of
10
11 206 both models. The highest values of magnetic susceptibility were up to 0.28 and 0.30 (S.I.), six times
12
13 207 higher than the original model (Table 2). The densities had less drastic lateral change, with values that
14
15 208 approximated to the original model (Table 2 and 3).

16
17 209 The residual fields (Figs. 6 and 7) indicated low values, with local significant anomalies that
18
19 210 usually represented the compensation of volume in Model 2 and the additional sections in models 3
20
21 211 and 4. The residuals of the magnetic and gravity fields of Model 1 were considerably low, indicating
22
23 212 good solutions for the modelled field.

24
25
26
27 213

28
29 214

30 31 32 215 **4. Real Case**

33
34 216

35 36 217 *4.1. Geological Context*

37
38 218

39
40
41 219 Lying in the southwest of Mato Grosso State, Brazil, the Jauru Terrane contains the Alto
42
43 220 Jauru Group and the Alto Guaporé Metamorphic Complex (Souza *et al.* 2009; Matos *et al.* 2009). The
44
45 221 Alto Jauru Group (1760 to 1720 Ma) (Monteiro *et al.* 1985; Bettencourt *et al.* 2010) comprises gneiss,
46
47 222 migmatites and the Cabaçal, Araputanga and Jauru meta-volcanosedimentary sequences. The Alto
48
49 223 Guaporé Metamorphic Complex (1790 to 1740 Ma) (Menezes 1993) is characterized by orthogneiss
50
51 224 intruded into supracrustal volcanosedimentary sequences, both metamorphosed to greenschist or
52
53 225 amphibolite facies (Bettencourt *et al.* 2010).

54
55
56 226 The Figueira Branca Suite (Fig. 8) is a layered mafic-ultramafic complex composed of dunite,
57
58 227 pyroxenite, gabbro-norite, anorthosite, troctolite, and olivine-gabbro (Teixeira *et al.* 2011). The

228 crystallization age of the Indiavaí gabbro, the southernmost intrusion of the Figueira Branca Suite,
 229 was dated by SHRIMP U-Pb zircon at 1425 ± 8 Ma. Ar-Ar dating on biotites yielded plateau ages of
 230 1275 ± 4 Ma and 1268 ± 4 Ma, which were evaluated as minimum ages for regional cooling (Teixeira
 231 *et al.* 2011).

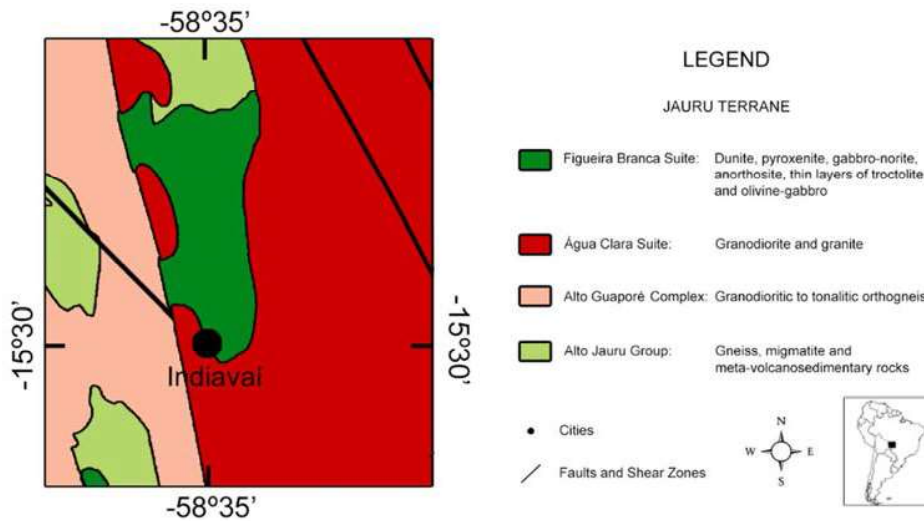
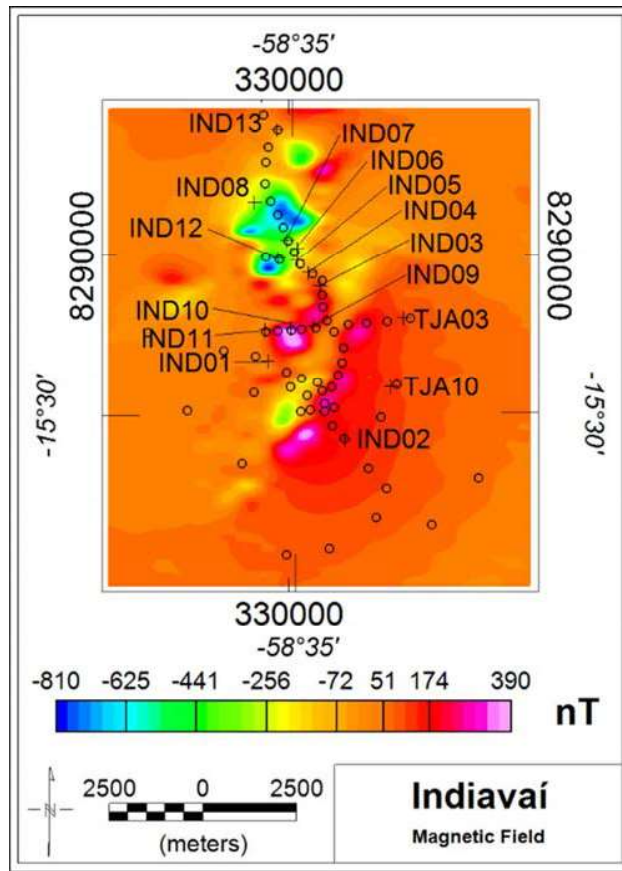


Fig. 8 – Local geological map (Saes *et al.* 1984; Nunes 2000; Teixeira *et al.* 2011).

235 In 2006, the Brazilian Geological Service (CPRM) undertook the magnetic field airborne
 236 survey “Projeto 1080 – Área 2 Mato Grosso”. This survey covers the region occupied by the Figueira
 237 Branca Suite. The collected magnetic field data revealed a magnetic anomaly coherent with the
 238 Indiavaí body outcrops. The magnetic anomaly showed a complex signature (Fig. 9), which is
 239 different from that expected for purely induced magnetic anomalies in the south hemisphere, where
 240 the positive area is to the north and the negative to the south of the centre of the magnetic source. The
 241 magnetization contrast supported a gravity ground survey and the collection of samples for
 242 geophysical and mineralogical analyses over the suite. 50 samples were collected, 15 in the Indiavaí
 243 area, of mafic-ultramafic rocks of the Figueira Branca Suite, of granitic suites adjacent to the Figueira
 244 Branca, and of the meta-volcanosedimentary Alto Jauru Group (Fig. 8).



245

246 Fig. 9 – Magnetic anomaly of Indiavaí. The black circles indicate the location of the gravity

247 stations.

248

249

4.2. Data

250

251

252 The magnetic field survey used Geometrics G-822A Cesium magnetometers with a resolution
 253 of 0.001 nT. The sampling interval of 0.1 s resulted in an approximate sample spacing of 7.8 m. The
 254 magnetic noise level is 0.5 nT after the industry standard corrections were applied. The average
 255 International Geomagnetic Reference Field (IGRF) ambient field for this period had inclination -
 256 11.6°, declination 234.9°, and intensity 23749 nT.

257 Density measurements were made on the collected samples using the “Archimedes method”.
 258 These measurements were performed with distilled water and a high-precision analytic balance.
 259 Magnetic susceptibility measures were taken using a Kappameter KT-9 magnetic susceptibility meter
 260 (Table 4). Thin sections of the samples from the intrusion and from the host-rock were prepared and
 261 analysed.

262

263 Table 4 – Densities and magnetic susceptibilities of the samples from Figueira Branca Suite area.

Sample	Lithology	Suite/Group	Density (g/cm ³)	Error (g/cm ³)	Magnetic Susceptibility (SI)	Error (SI)
IND01	Granite	Água Clara	2.63	$4.31 \cdot 10^{-7}$	0.010	0.001
IND02	Gneiss	Alto Guaporé	2.96	$3.50 \cdot 10^{-5}$	0.011	0.001
IND03	Gabbro	Figueira Branca	2.96	$2.59 \cdot 10^{-5}$	0.073	0.005
IND04	Gabbro	Figueira Branca	2.89	$2.64 \cdot 10^{-7}$	0.028	0.002
IND05	Gabbro	Figueira Branca	2.99	$2.30 \cdot 10^{-7}$	0.038	0.003
IND06	Gabbro	Figueira Branca	2.87	$3.28 \cdot 10^{-5}$	0.024	0.002
IND07	Diorite	Água Clara	2.91	$2.51 \cdot 10^{-5}$	0.002	0.000
IND08	Granite	Alto Jauru	2.66	$1.85 \cdot 10^{-5}$	0.000	0.000
IND09	Gabbro	Figueira Branca	2.92	$3.52 \cdot 10^{-5}$	0.039	0.003
IND10	Gabbro	Figueira Branca	2.93	$1.74 \cdot 10^{-5}$	0.057	0.004
IND11	Gabbro	Figueira Branca	2.76	$2.03 \cdot 10^{-7}$	0.000	0.000
IND12	Granite	Água Clara	2.76	$2.57 \cdot 10^{-7}$	0.001	0.000
IND13	Granite	Água Clara	2.69	$1.33 \cdot 10^{-5}$	0.031	0.004
TJA03	Gneiss	Alto Jauru	2.89	$2.59 \cdot 10^{-7}$	0.000	0.000
TJA10	Gneiss	Alto Jauru	2.82	$2.17 \cdot 10^{-7}$	0.010	0.000

264

265

266 The samples were divided in two groups: one comprising specimens from the Figueira Branca
 267 Suite, and one from the adjacent lithologies that host the suite. The limits of Figueira Branca Suite
 268 have been defined since the 1980's. Rocks assigned to the suite and to the country rock were based on
 269 field and thin-section analysis. The density and magnetic susceptibility measurements for the samples
 270 collected in the suite domain showed a large variation. The densities varied from 2.63 g/cm³ to 2.99
 271 g/cm³, whereas the magnetic susceptibility ranged from 0 to 0.073 (S.I.). Averages for the density and
 272 magnetic susceptibility of the mafic rock samples were, 2.89 g/cm³ and 0.027 (S.I.) respectively. The

1
2
3 273 average values are low for a mafic-ultramafic suite, so thin section analyses were taken to evaluate the
4
5 274 cause.

6
7
8 275

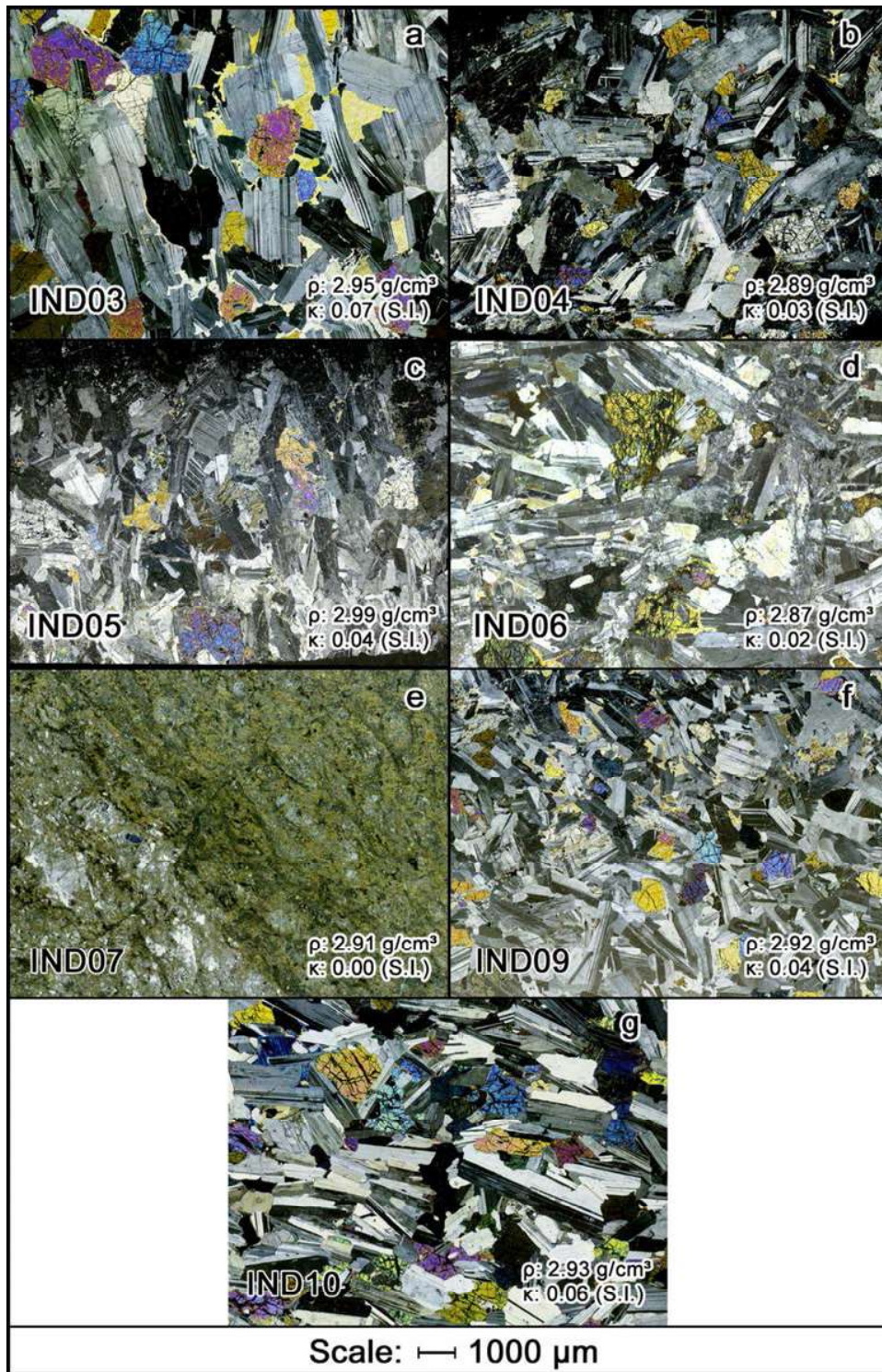
9
10 276

11
12
13 277

4.3. Samples and Thin Sections

14
15 278

16
17 279 Despite the apparent freshness of the hand samples, the thin sections showed variable degrees
18
19 280 of alteration and weathering. Seven thin sections of samples collected from the Indiavaí body (Fig.
20
21 281 10) revealed plagioclase to be the dominant mineral phase (c.a. 70%), followed by olivine (c.a. 20%)
22
23 282 and pyroxene (c.a. 10%). The samples IND01, IND08 and IND13 were recognized as granitic rocks
24
25 283 and considered as part of the host-rock. The samples IND03 and IND10 were the least affected by
26
27 284 weathering or alteration, and maintained higher values of density and magnetic susceptibility. These
28
29 285 two samples were coarse grained, with plagioclase crystals reaching 5 mm and olivine crystals of 2
30
31 286 mm. Samples IND04, IND05, IND06 and IND09 showed signs of weathering along fractures of
32
33 287 olivine grains, and more significantly in plagioclase grains in sample IND06, which displayed both
34
35 288 weathering and alteration. The weathering was present on a smaller scale than in IND05, but it is
36
37 289 possible to observe serpentinization along olivine fractures. IND07 displayed intense weathering, and
38
39 290 it was impossible to identify primary igneous crystals.
40
41
42
43
44
45
46
47
48
49
50
51
52
53
54
55
56
57
58
59
60



291

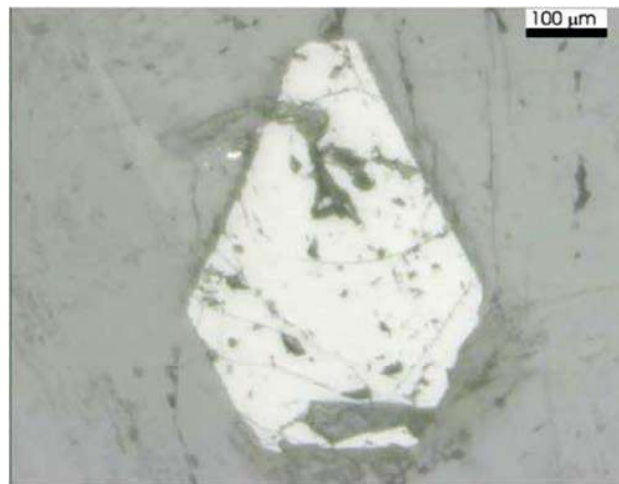
292 Fig. 10 – Thin sections from the Indiavaí body (a) IND03, (b) IND04, (c) IND05, (d) IND06, (e)

293 IND07, (f) IND09 and (g) IND10. ρ indicates the measured density, whereas κ represents the

294 magnetic susceptibility. The images were produced with cross-polarized light.

1
2
3 295 The presence of opaque oxide crystals occurs in a number of samples (e.g., IND03 and
4
5 296 IND10). D'Agrella-Filho et al. (2012) identified euhedral magnetite crystals (Fig. 11) up to
6
7 297 approximately 0.5 mm in samples from the same outcrop as sample IND03. The higher content of
8
9 298 opaque crystals in IND03 and IND10 can be associated with the considerably higher magnetic
10
11 299 susceptibility, when compared with other Indiavaí samples.

12
13
14 300



32
33

34 302 Fig. 11 – Euhedral magnetite crystal from the Indiavaí body (D'Agrella-Filho *et al.* 2012).

35
36 303

37
38
39 304

40
41
42 305

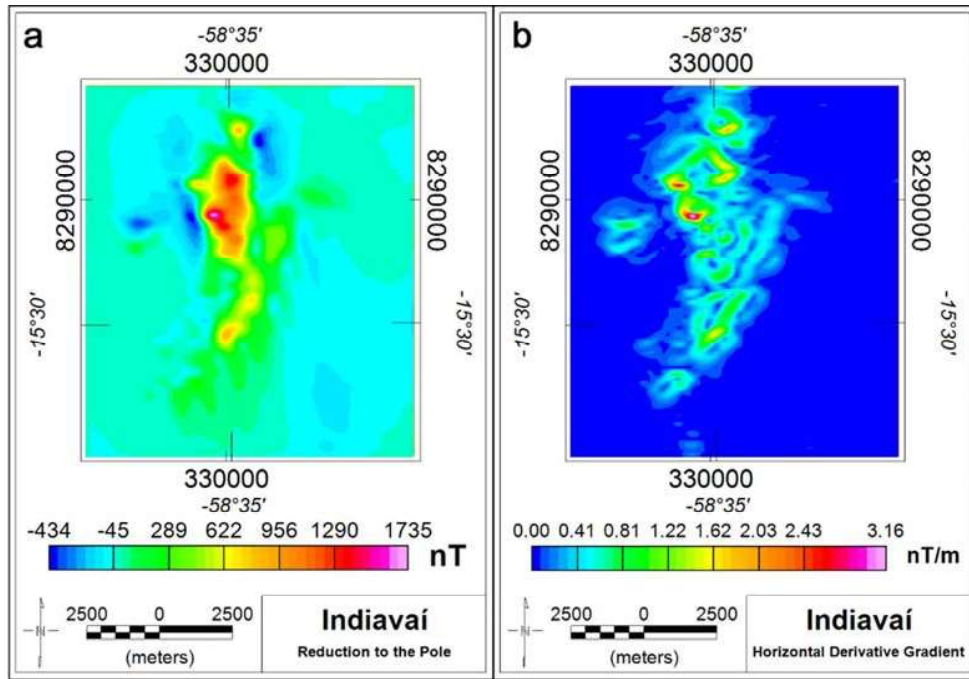
4.4. Potential Fields Modelling

43
44 306

45
46
47 307 The outcrops of the Indiavaí body indicate the body extends to the surface. The complex
48
49 308 magnetic anomaly pattern of the body, likely reflecting different sources, impeded the MaxiMin
50
51 309 method to reduce the field to the pole with minimum negative values (Fig. 12a). The best
52
53 310 approximation was an inclination of 56° and declination of 213° ($\alpha_{95\%}=5^\circ$, 386 iterations). The
54
55 311 inclination 56° and the declination 213° were used as fixed total magnetization directions during the
56
57
58
59
60

312 whole staged-inversion. The lateral limits were assessed through horizontal gradient derivatives of the
 313 field reduced to the pole (Fig. 12b).

314



315

316 Fig. 12 – (a) Reduction to the pole and (b) horizontal derivative gradient of the Indiavaí
 317 anomaly.

318

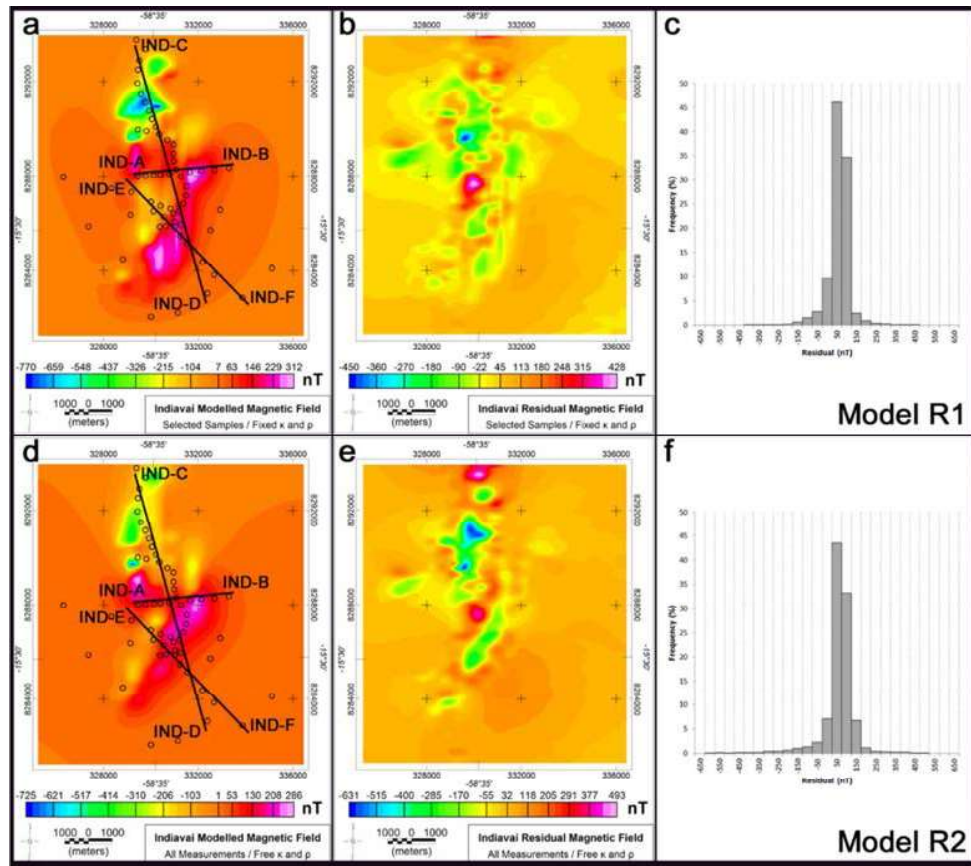
319 Two inversions were performed following the same principles as applied to the synthetic
 320 models. Model R1 (Fig. 14a to c) used only measurements from samples considered fresh on the basis
 321 of the thin section analysis, and kept them fixed during the inversion; the best case scenario. Model
 322 R2 (Fig. 14d to f) used all density and magnetic susceptibility measurements and let them vary during
 323 the inversion, as is generally used in exploration projects. Table 5 shows the characteristics and rms-
 324 errors for the two real-case models. The inversion of the magnetic field happened in the two phases
 325 described in the methodology section, whereas the gravity field inversion occurred only in profiles
 326 (second phase of the staged-inversion) due to the reduced number and restricted spread of gravity
 327 stations.

328 Table 5 - Inversion results for the model considering all the magnetic susceptibilities and density
 329 measurements, and for the model with the magnetic susceptibilities and densities from samples
 330 considered fresh after the thin sections analyses. κ and ρ represent the magnetic susceptibility and the
 331 density, respectively.

Geophysical Models			
Background (Host-rock)			
Average Magnetic Susceptibility		0.007 (SI)	
Average Density		2.70 g/cm ³	
Model R1: Fixed κ and ρ – IND03, IND05, IND09 and IND10			
Average Magnetic Susceptibility		0.05 (SI)	
Average Density		2.94 g/cm ³	
Total Volume		9.35 km ³	
Magnetic and Gravity Fields Inversions			
Magnetization	Induced	Total ($\alpha_{95\%} = 5.0^\circ$)	Remanent ($\alpha_{95\%} = 8.9^\circ$)
Inclination (°)	-11.6	56	49.6
Declination (°)	346.9	213	199.5
Intensity (A/m)	0.9	3.8	4.4
RMS-Mag (%)	4.9	# of Points	29003
Average RMS-Grav (%)	8.6	# of Points	60
Model R1: Free κ and ρ – Samples IND02 to IND07 and IND09 to IND12			
Average Magnetic Susceptibility		0.29 (SI)	
Average Density		2.83 g/cm ³	
Total Volume		22.23 km ³	
Magnetic and Gravity Fields Inversions			
Magnetization	Induced	Total ($\alpha_{95\%} = 5.0^\circ$)	Remanent ($\alpha_{95\%} = 13.6^\circ$)
Inclination (°)	-11.6	56	27.7
Declination (°)	346.9	213	207.7
Intensity (A/m)	4.2	1.4	4.7
RMS-Mag (%)	7.4	# of Points	29003
Average RMS-Grav (%)	11.0	# of Points	60

332

333 The inversion using magnetic susceptibility and density measurements on samples IND03,
 334 IND05, IND09 and IND10 (Model R1) achieved a rms-error of 4.9% in the magnetic case and 8.6%,
 335 on average for the Bouguer anomaly profiles (Table 5). The maximum absolute residuals were 450 nT
 336 (Fig. 13a to c) and 0.6 mGal (Fig. 14a). The highest residual amplitudes are centred in two spikes.
 337 The modelled body had 10500 m in north-south direction and 4000 m in the east-west. The maximum
 338 vertical extension achieved was 1000 m (Fig. 15). The remanent magnetization obtained for this
 339 model had an inclination 49.6°, declination 199.5° and intensity 4.4 A/m ($\alpha_{95\%} = 8.9^\circ$).



340

341 Fig. 13 – Model R1 (a) modelled and (b) residual magnetic fields, (c) histogram of residual values.

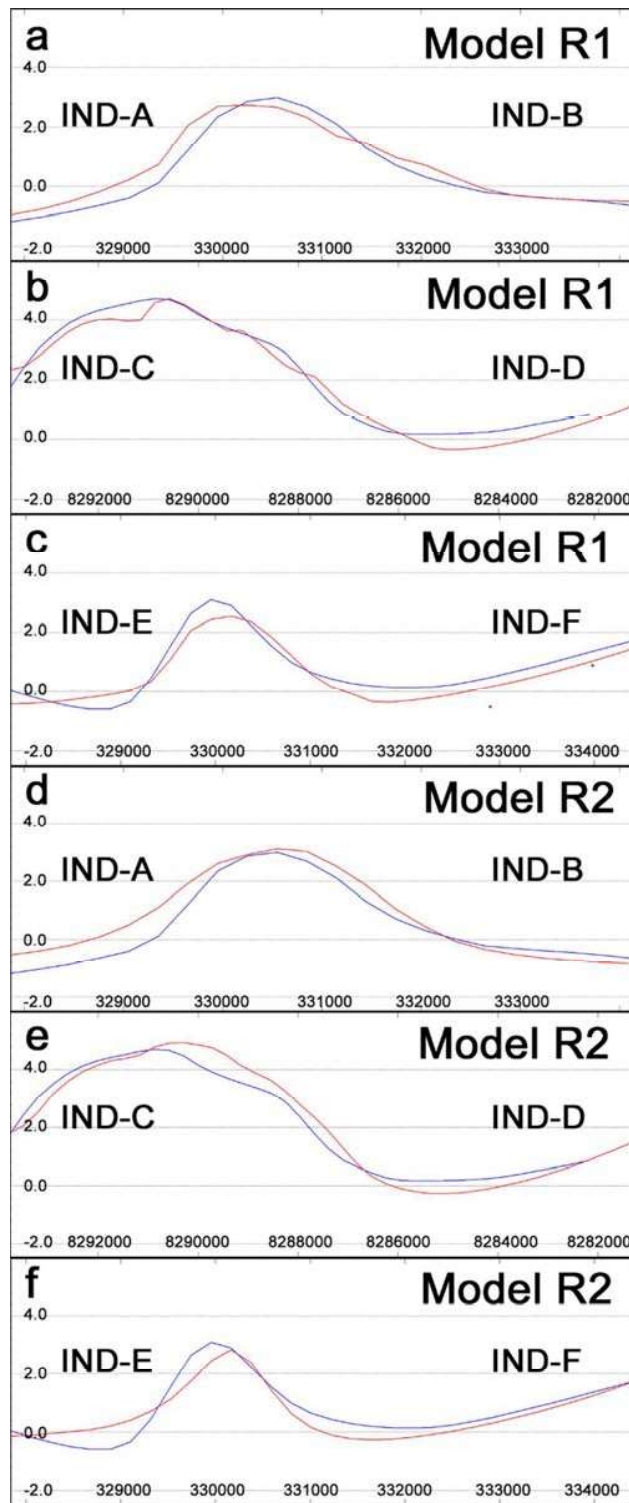
342 Model R2 (d) modelled and (e) residual magnetic fields, (f) histogram of residual values. The black
 343 circles indicate the location of the gravity stations and the black lines the profiles used for gravity
 344 modelling.

345

346

347 Model R2 (Fig. 14d to f) used all the available measurements (samples IND02 to IND07 and
 348 IND09 to IND12), and let them vary during the staged-inversion. The modelled magnetic field had
 349 rms-error of 7.4%, and the average rms-error of 11% in the Bouguer anomaly profiles (Table 5). The
 350 absolute residuals were 631 nT and 0.8 mGal (Fig. 14). The more significant values are distributed
 351 along four regions in the centre and at the north of the magnetic and Bouguer anomaly fields (Figs. 14
 352 and 15). The lateral extension of the modelled body was 10700 m in north-south direction and 4000 m
 353 in the east-west, and it had maximum vertical extension of 2500 m (Fig. 14). The remanent
 354 magnetization obtained in this case was defined by inclination 27.7° , declination 207.7° and intensity
 4.7 A/m ($\alpha_{0.5\%} = 13.6^\circ$).

1
2
3
4
5
6
7
8
9
10
11
12
13
14
15
16
17
18
19
20
21
22
23
24
25
26
27
28
29
30
31
32
33
34
35
36
37
38
39
40
41
42
43
44
45
46
47
48
49
50
51
52
53
54
55
56
57
58
59
60

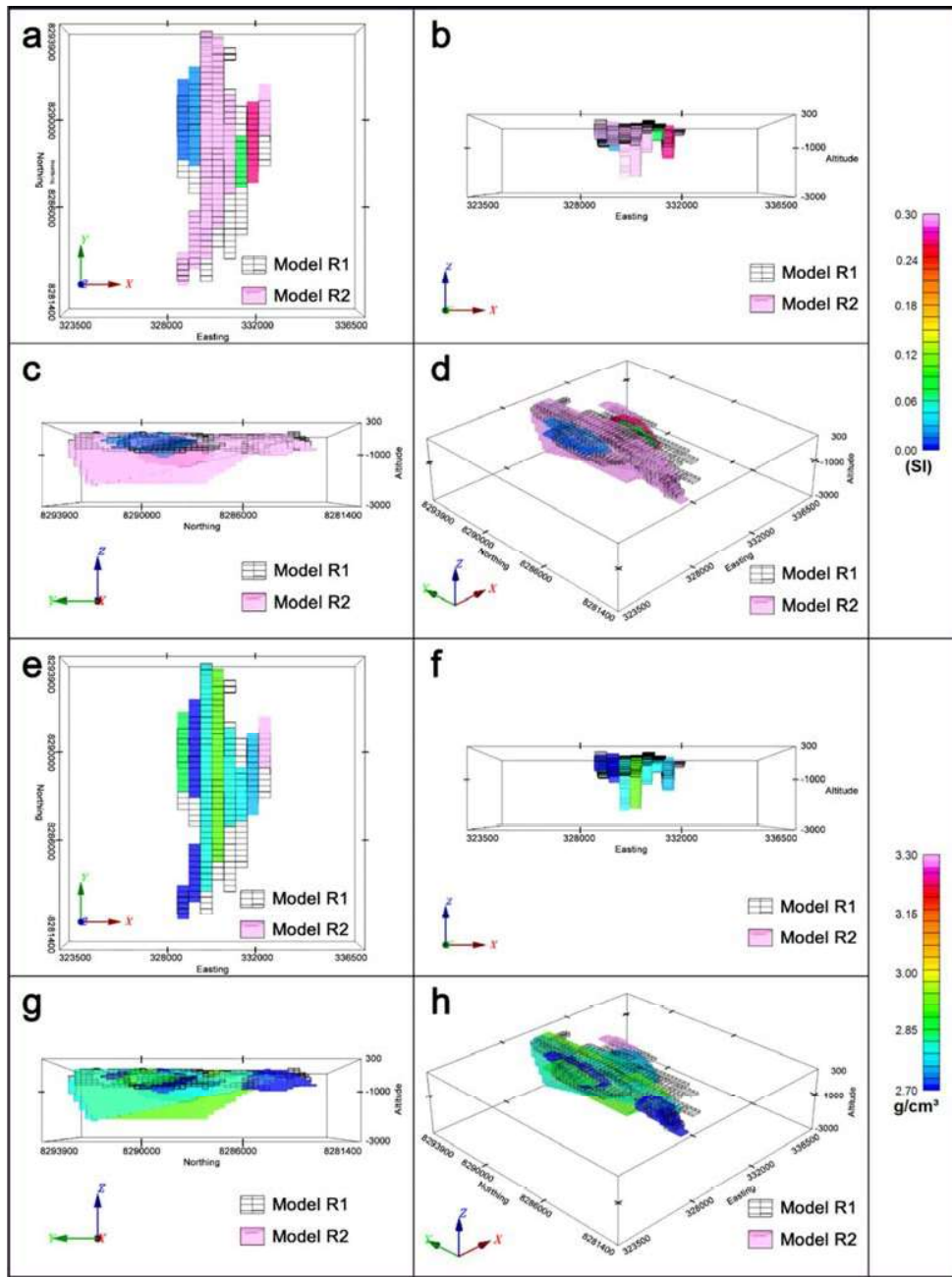


355

356 Fig. 14 – Bouguer anomaly profiles (blue) and modelled Bouguer anomaly (red) for models R1 and

357 R2. (a) and (d) shows the profile from IND-A to IND-B (Fig. 13), (b) and (e) the profile from IND-C

358 to IND-D, and (f) and (g) present the profile from IND-E to IND-F.



359

360 Fig. 15 – Magnetic susceptibility and density distribution for models R1 and R2 in the views: (a) and
 361 (e) top, (b) and (f) south, (c) and (g) west, and (d) and (h) perspective (inclination 30°, azimuth 45°).

362 Model R1 is represented by a black grid and represents the magnetic susceptibility 0.05 and density
 363 2.94 g/cm³.

364

365 **5. Discussion**

366

367 Modelling the magnetic and gravity field of the synthetic body using both the same parameters
368 as the original synthetic body and using inaccurate constraints, and keeping them fixed or allowing
369 them to vary in the staged inversion, indicated that the rms-error can be reduced to acceptable values
370 in all cases. However, the shape of the modelled body and the distribution of magnetic susceptibilities
371 and densities were severely affected. The modelled fields had rms-errors smaller than 4.0%, a good
372 value considering that it is a synthetic model without noise or interfering anomalies. The apparent
373 remanent magnetization in all cases differed from the original model by less than 10°, both in
374 inclination and declination, whereas the intensities have not exceeded more than 2 A/m of difference.

375 The lateral distribution of the modelled bodies kept the overall shape of the original model.
376 Model 1 (Fig. 5a and b) had the best distribution as would be expected for a model using all the
377 correct constraints. Models 2 to 4 (Fig. 5c to h) presented one to two sections more than the original
378 model, and their depths and depth extents were overestimated during the inversion. Model 2, which
379 kept fixed the magnetic susceptibility and density, extended to depths almost twice the size of the
380 original model. Models 3 and 4 (Fig. 5e to h) showed smaller variations in depth, except for the
381 sections that lay beyond the original model limits, which were displaced to considerably shallower or
382 deeper depths (Fig. 6).

383 Models 3 and 4 (Fig. 5e to h), in which magnetic susceptibilities and densities were allowed to
384 vary during the staged inversion, displayed variation in these features along the north-south oriented
385 sections. Both cases showed much higher properties in two or three sections, whereas the remaining
386 sections had values next to zero. This behavior was reflected in the residual fields, indicating exactly
387 the sections with higher properties, and what increased the rms-error.

388 The four synthetic cases showed that inaccurate constraints can interfere with the final result of
389 the modelling. Unsurprisingly, the best solution for the synthetic gravity and magnetic fields was
390 achieved by modelling with the right constraints fixed (Model 1, Fig. 5a and b), which resulted in a

1
2
3 391 low rms-error (Table 2) and a model with the closest shape, volume and physical properties to the
4
5 392 original body. In real cases, having all the correct constraints is not trivial or even possible in some
6
7 393 situations. The next best result was achieved by modelling with the correct initial constraints and then
8
9 394 allowing the magnetic susceptibility and density to change during the inversion (Model 3). Model 4,
10
11 395 which used inaccurate parameters that were allowed to change during the modelling, had the third
12
13 396 best result on the basis of the model and the rms-errors. The least reliable model used inaccurate
14
15 397 magnetic susceptibility and density values that were keep fixed during the inversion.

16
17 398 The magnetic and gravity anomalies associated with the Indiavaí body of the Figueira Branca
18
19 399 Suite were modelled using two of the cases shown with the synthetic models. One case (R1) used only
20
21 400 magnetic susceptibilities and densities from samples selected after mineralogical analyses, and kept
22
23 401 these features fixed during the staged inversion, similarly to Model 1. The second case, Model R2,
24
25 402 used all the measurements available and let magnetic susceptibility and density change during the
26
27 403 staged inversion, like Model 4. The two methodologies were chosen to apply the best case scenario
28
29 404 indicated by the synthetic model inversion, and the most common situation in geophysical
30
31 405 exploration, with limited data available.

32
33
34 406 The two inversions obtained low rms-errors for real data. Low rms-errors do not necessarily
35
36 407 reflect an adequate and geologically feasible result. Both models were elongated in north-south
37
38 408 direction and presented the same 4000 m extension in east-west direction. The major differences
39
40 409 between the two models were in the vertical extension, the volume, and the distribution of magnetic
41
42 410 susceptibility and density (Table 5 and Fig. 15). The maximum vertical extension of Model R2 was
43
44 411 2.5 times larger than in Model R1. This difference reflected directly in the volume, which showed
45
46 412 similar proportion (2.37 times).

47
48
49 413 Model R1 kept the magnetic susceptibility and density fixed, but varied the amplitude of total
50
51 414 magnetization, depth and the position of the vertices of the model. This staged-inversion proved to be
52
53 415 more time-consuming, especially on areas where the gravity profiles crossed the magnetic lines and
54
55 416 each other. The results showed a more compact body, and smaller errors than the inversions of Model
56
57 417 R2. The staged-inversion of Model R2 reduced the error considerably faster than in Model R1

1
2
3 418 process. Model 2, however, presented a large variation in the depth of the base of the model and in the
4
5 419 magnetic susceptibility and density. These last two features, similarly to the synthetic cases 3 and 4
6
7 420 (Fig. 5e to h), presented the concentration of higher values in some north-south sections, whereas the
8
9 421 remaining sections ended up with values near zero (Fig. 15).

10
11 422 The apparent remanent magnetization obtained in both real data cases were similar to the
12
13 423 paleomagnetic data obtained by D'Agrella-Filho *et al.* (2012). The natural remanence magnetization
14
15 424 (NRM) for the Indiavaí body has inclination 50.7° and declination 209.8° ($\alpha_{95\%} = 8.0^\circ$). The apparent
16
17 425 remanent magnetization for Model R1 had inclination 63.0° and declination 187.3° ($\alpha_{95\%}=8.9^\circ$), and
18
19 426 for Model R2, inclination 27.7° and declination 207.7° ($\alpha_{95\%}=13.6^\circ$). The proximity of the indirectly
20
21 427 estimated apparent magnetic remanence with the calculated NRM is remarkable, considering the
22
23 428 complexity and degree of interference of smaller anomalies over the main Indiavaí magnetic anomaly.

24
25
26
27 429

28
29 430

30 31 32 431 **6. Conclusions**

33
34 432

35
36
37 433 Measurements of densities and magnetic susceptibilities of samples from the Indiavaí body
38
39 434 from the Figueira Branca suite were abnormally low. Modelling potential fields with inaccurate
40
41 435 constraints can produce results significantly different than the actual source of the geophysical
42
43 436 signals.

44
45
46 437 A synthetic model was composed and used to test four different approaches for the staged-
47
48 438 inversion: two keeping the magnetic susceptibility and density fixed, and two setting them free during
49
50 439 the inversion. Correct and inaccurate properties were used in both cases. The model keeping the
51
52 440 correct properties fixed was the one that best reduced the residuals between observed and modelled
53
54 441 magnetic and gravity fields, and resulted in the shape and volume that best approached the original
55
56 442 model. The other models approximated to the original synthetic model, minimizing the rms-errors and

1
2
3 443 quantitatively followed the sequence, from best to worst: correct properties set free (Model 3),
4
5 444 inaccurate properties set free (Model 4), and inaccurate fixed properties (Model2).
6

7
8 445 Based on the results from the synthetic models, the magnetic and gravity field anomalies
9
10 446 associated with the Indiavaí body of the Figueira Branca Suite were modelled. Values of density and
11
12 447 magnetic susceptibilities were averaged from measurements obtained from hand-samples. Some of
13
14 448 the values obtained on these measurements were relatively low for the mafic-ultramafic rocks that
15
16 449 constitute the Figueira Branca Suite and corresponded with thin-section observations indicating
17
18 450 varying degrees of alteration and weathering.
19

20
21 451 Based on the variation in the condition of the samples, two approaches were used to evaluate
22
23 452 the effects of inaccurate constraints in the modelling of real potential fields. One model (R1) used
24
25 453 measurements made only on fresh samples, indicated by thin-sections, and kept these values fixed
26
27 454 during inversion. The second model (R2) used all the measurements, emulating a case where thin-
28
29 455 section analyses would not be available. Although both inversions presented rms-errors below 13%
30
31 456 for a considerably complex anomaly, Model R1 still had an rms-error of almost half of Model R2. The
32
33 457 shape of R1 was more regular and compact, with a single magnetic susceptibility and density for all
34
35 458 sections. Model R2 had 2.5 times the volume and vertical extension of Model R1. However, it took
36
37 459 much less time to achieve the rms-error than in Model R1. Distributions of magnetic susceptibility
38
39 460 and density as seen in Model R2 (north-south-oriented sections of fixed physical properties) are
40
41 461 geologically feasible, but less plausible for potential field modelling than assuming a homogeneous
42
43 462 distribution, as in Model R1.
44

45
46 463 Exploration projects frequently do not have the necessary time to spend on long and complex
47
48 464 modelling procedures, which makes the approach used in Model R2 appealing. Nevertheless, the
49
50 465 magnetic susceptibility and the density evidenced the importance of using correct constraints. The
51
52 466 results obtained in this paper showed that geological observation, thin-sections, and any other direct,
53
54 467 and/or indirect, constraints are valuable assets for a proper and reliable modelling.
55

56 468
57
58
59
60

469

470 **7. Acknowledgements**

471

472 The authors would like to thank Sebastian Fischer, Stuart Allison and Donald Herd for the help
473 with the thin sections, Vanessa B. Ribeiro for comments, and the Brazilian Geological Service for the
474 data. This work was done with the support of the CNPq, National Council for Technological and
475 Scientific Development – Brazil.

476

477

478 **8. References**

479

480 Bettencourt, J.S., Leite Jr, W.B., Ruiz, A.S., Matos, R., Payolla, B.L. & Tosdal, R.M., 2010.

481 The Rondonian-San Ignacio Province in the SW Amazonian Craton: An overview,
482 *Journal of South American Earth Sciences*, 29, 28-46.

483 Cordani, R. & Shukowsky, W., 2009. Virtual Pole from Magnetic Anomaly (VPMA): A
484 procedure to estimate the age of a rock from its magnetic anomaly only, *J Appl*
485 *Geophys*, 69, 96-102.

486 D'Agrella-Filho, M.S., Trindade, R.I.F., Elming, S.A., Teixeira, W., Yokoyama, E., Tohver,
487 E., Geraldés, M.C., Pacca, I.I.G., Barros, M.A.S. & Ruiz, A.S., 2012. The 1420 Ma
488 Indiavai Mafic Intrusion (SW Amazonian Craton): Paleomagnetic results and
489 implications for the Columbia supercontinent, *Gondwana Res*, 22, 956-973.

490 Fedi, M., Florio, G. & Rapolla, A., 1994. A Method to Estimate the Total Magnetization
491 Direction from a Distortion Analysis of Magnetic-Anomalies, *Geophys Prospect*, 42,
492 261-274.

- 1
2
3 493 Foss, C., 2006. Evaluation of strategies to manage remanent magnetization effects in
4
5 494 magnetic field inversion. *in 76th Annual SEG International Meeting*, pp. 4SEG, New
6
7 495 Orleans.
- 8
9
10 496 Matos, J.B.d., Silva, C.H.d., Costa, A.C.D.d., Ruiz, A.S., Souza, M.Z.A.d., Batata, M.E.F.,
11
12 497 Corrêa da Costa, P.C. & Paz, J.D.d.S., 2009. Geologia e Recursos Minerais da Folha
13
14 498 Jauru (SD.21-Y-C-III). *in Programa Geologia do Brasil*, pp. 134, Cuiabá.
- 15
16 499 Menezes, R.G., 1993. Pontes e Lacerda. Folha SD. 21-Y-c-n. *in Programa Levantamentos*
17
18 500 *Geológicos Básicos do Brasil - PLGBCPRM - Serviço Geológico do Brasil*.
- 19
20 501 Monteiro, H., Macedo, P.M.d., Silva, M.D.d., Moraes, A.A.d. & Marcheto, C.M.L., 1985. O
21
22 502 'Greenstone Belt' do Alto Jauru. *in XXXIV Congresso Brasileiro de*
23
24 503 *Geologia*Sociedade Brasileira de Geologia, Goiânia.
- 25
26
27 504 Nunes, N.S.d.V., 2000. Geologia e resultados prospectivos da área de Figueira
28
29 505 Branca/Indiavaí, Mato Grosso. *in Série Metais do Grupo da Platina e*
30
31 506 *Associados*CPRM - Serviço Geológico do Brasil.
- 32
33
34 507 Pratt, D.A.F., C. A.; Roberts, S., 2006. User Guided Inversion & Visualisation of
35
36 508 Interpretation Confidence. *in AESC Conference*, pp. 1-7AESC, Melbourne, Australia.
- 37
38
39 509 Reid, A.B., Allsop, J.M., Granser, H., Millett, A.J. & Somerton, I.W., 1990. Magnetic
40
41 510 interpretation in three dimensions using Euler deconvolution, *Geophysics*, 55, 80.
- 42
43 511 Saes, G.S., Leite, J.A.S. & Weska, R.K., 1984. Geologia da Folha Jauru (SD.21.Y.C.III): uma
44
45 512 síntese de conhecimentos. *in 33rd Congresso Brasileiro de Geologia*Sociedade
46
47 513 Brasileira de Geologia, Rio de Janeiro.
- 48
49
50 514 Souza, M.Z.A.d., Batata, M.E.F., Ruiz, A.S., Lima, G.A.d., Matos, J.B.d., Paz, J.D.d.S.,
51
52 515 Costa, A.C.D.d., Silva, C.H.d. & Corrêa da Costa, P.C., 2009. Geologia e Recursos
53
54 516 Minerais da Folha Rio Branco (SD-21-Y-D-1). *in Programa Geologia do Brasil*, pp.
55
56 517 178, Cuiabá.

1
2
3
4
5
6
7
8
9
10
11
12
13
14
15
16
17
18
19
20
21
22
23
24
25
26
27
28
29
30
31
32
33
34
35
36
37
38
39
40
41
42
43
44
45
46
47
48
49
50
51
52
53
54
55
56
57
58
59
60

518 Teixeira, W., Geraldes, M.C., D'Agrella, M.S., Santos, J.O.S., Barros, M.A.S., Ruiz, A.S. &
519 da Costa, P.C.C., 2011. Mesoproterozoic juvenile mafic-ultramafic magmatism in the
520 SW Amazonian Craton (Rio Negro-Juruena province): SHRIMP U-Pb geochronology
521 and Nd-Sr constraints of the Figueira Branca Suite, *Journal of South American Earth*
522 *Sciences*, 32, 309-323.
523

3. Manuscript 2: Tectonic insights of the Southwest Amazon Craton from geophysical, geochemical and mineralogical data of Figueira Branca Mafic-Ultramafic Suite, Brazil

Once defined the mineralogy and lithology of the samples, and ultimately, the proper constraints to be used in a potential field inversion, the following stage was to analyse the Figueira Branca Suite. This chapter develops geophysical models of the bodies that compose the suite, investigates the extent of the magmatism that generated it, the geochemical features of the parental magma and the local tectonic framework by the time of the intrusion.

Magnetic and gravity field data were modelled to evaluate the geometry and an approximation of the volume of the bodies from the Figueira Branca Suite. Gamma-ray spectrometry revealed areas where the intrusions outcropped or were very shallow. Major and trace elements geochemistry identified the samples as gabbros and peridotite-gabbros, whereas light-Rare-Earth element trends suggest a progressive fractionation of the magma. Trace element plots, allied with the observed and previously published geology of the region, indicated a back-arc extension framework in the later stages of the Santa Helena Orogen.

Manuscript Number: TECTO11736

Title: Tectonic insights of the Southwest Amazon Craton from geophysical, geochemical and mineralogical data of Figueira Branca Mafic-Ultramafic Suite, Brazil

Article Type: Research Paper

Keywords: Potential Fields; Geochemistry; Mineralogy; Radiometrics; Amazon Craton

Corresponding Author: Mr. Vinicius Hector Louro, MSc.

Corresponding Author's Institution: Instituto de Astronomia, Geofísica e Ciências Atmosféricas da Universidade de São Paulo

First Author: Vinicius Hector Louro, MSc.

Order of Authors: Vinicius Hector Louro, MSc.; Peter A Cawood, PhD; Marta S Mantovani, PhD

Abstract: The Figueira Branca Suite is a layered mafic-ultramafic complex in the Jauru Terrane, southwest Amazon Craton. New lithological, geochemical, gamma-ray and potential field data, integrated with geological, isotope and paleomagnetic data are used to characterize this pulse of Mesoproterozoic extension-related magmatism. The Figueira Branca Suite formed through juvenile magma emplacement into the crust at 1425 Ma, coeval with the later stages of the Santa Helena Orogen. Gabbros and peridotite-gabbros display increasing enrichment of LREE, interpreted as evidence of progressive fractionation of the magma. Magnetic and gamma-ray data delimit the extent of magmatism within the suite to four bodies to the north of Indiavaí city. Modelling gravity and magnetic field data indicate that the anomalous sources are close to the surface or outcropping. These intrusions trend northwest over 8 km, with significant remanent magnetization that is consistent with published direction obtained through paleomagnetic data. The emplacement, mineralogy and geochemical signature point towards a back-arc extension tectonic framework in the later stages of the Santa Helena Orogen.

Suggested Reviewers: Clive Foss
CSIRO

clive.foss@csiro.au

His research on potential field methods, developing modelling methodologies and applying in mining and tectonics.

Amarildo S Ruiz

Universidade Federal do Mato Grosso
asruiz@gmail.com

Researcher specialist in the Jauru Terrane, southwest Amazon Craton

Mauro C Geraldés

Universidade Estadual do Rio de Janeiro
geraldés@uerj.br

Researcher specialist in geochronology and geochemistry of the Amazon Craton

Fabio C Tontini

GNS Science

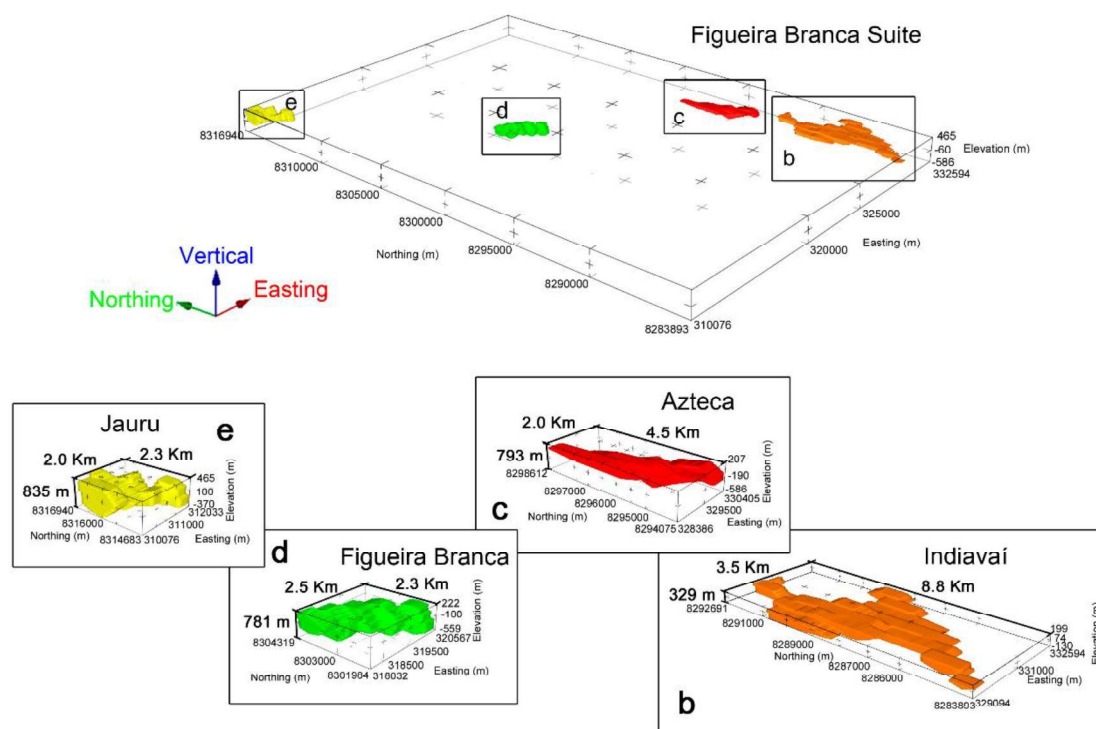
f.caratori.tontini@gns.cri.nz

Researcher specialist in potential fields modelling and tectonics

Tectonic insights of the Southwest Amazon Craton from geophysical, geochemical and mineralogical data of Figueira Branca Mafic-Ultramafic Suite, Brazil

Vinicius Hector Abud Louro, Peter Anthony Cawood, Marta Silvia Maria Mantovani

Graphical Abstract



Joint magnetic and gravity models of the Figueira Branca Suite constrained by petrophysical, geochemical and mineralogical analysis. In detail, (a) Indiavaí, (b) Azteca, (c) Figueira Branca and (d) Jauru models.

Tectonic insights of the Southwest Amazon Craton from geophysical, geochemical and mineralogical data of Figueira Branca Mafic-Ultramafic Suite, Brazil

Vinicius Hector Abud Louro, Peter Anthony Cawood, Marta Silvia Maria Mantovani

Highlights

- A model for the tectonic framework of the Jauru Terrane at 1.42 Ga is proposed.
- Gravity and magnetic field models constrained by geochemistry and mineralogy.
- The multi-method data showed indicated mafic intrusions in a back-arc setting.

1 **Tectonic insights of the Southwest Amazon Craton from geophysical,**
2 **geochemical and mineralogical data of Figueira Branca Mafic-Ultramafic Suite,**
3 **Brazil**

4

5 **Vinicius Hector Abud Louro^{1,2}, Peter Anthony Cawood², Marta Silvia Maria**
6 **Mantovani¹**

7

8 ¹ Instituto de Astronomia, Geofísica e Ciências Atmosféricas, Universidade de São Paulo,
9 São Paulo, Brazil.

10 ² Department of Earth and Environmental Sciences, University of St. Andrews, St. Andrews,
11 KY16 9AL, UK.

12

13 E-mails: vilouro@usp.br, pac20@st-andrews.ac.uk, msmmanto@usp.br

14

15 **Corresponding author:** Vinicius Hector Abud Louro.

16 **E-mail:** vilouro@usp.br

17

18 Phone: +55 (11) 99985 1501

19 Date of Submission: 28 January 2017

20

21

22

23

24

25

26

27

28 *Abstract*

29

30 The Figueira Branca Suite is a layered mafic-ultramafic complex in the Jauru Terrane,
31 southwest Amazon Craton. New lithological, geochemical, gamma-ray and potential field
32 data, integrated with geological, isotope and paleomagnetic data are used to characterize this
33 pulse of Mesoproterozoic extension-related magmatism. The Figueira Branca Suite formed
34 through juvenile magma emplacement into the crust at 1425 Ma, coeval with the later stages
35 of the Santa Helena Orogen. Gabbros and peridotite-gabbros display increasing enrichment of
36 LREE, interpreted as evidence of progressive fractionation of the magma. Magnetic and
37 gamma-ray data delimit the extent of magmatism within the suite to four bodies to the north
38 of Indiavaí city. Modelling gravity and magnetic field data indicate that the anomalous
39 sources are close to the surface or outcropping. These intrusions trend northwest over 8 km,
40 with significant remanent magnetization that is consistent with published direction obtained
41 through paleomagnetic data. The emplacement, mineralogy and geochemical signature point
42 towards a back-arc extension tectonic framework in the later stages of the Santa Helena
43 Orogen.

44

45 *Keywords*

46 Potential Fields; Geochemistry; Mineralogy; Radiometrics; Amazon Craton

47

48

49

50

51

52

53

54

55

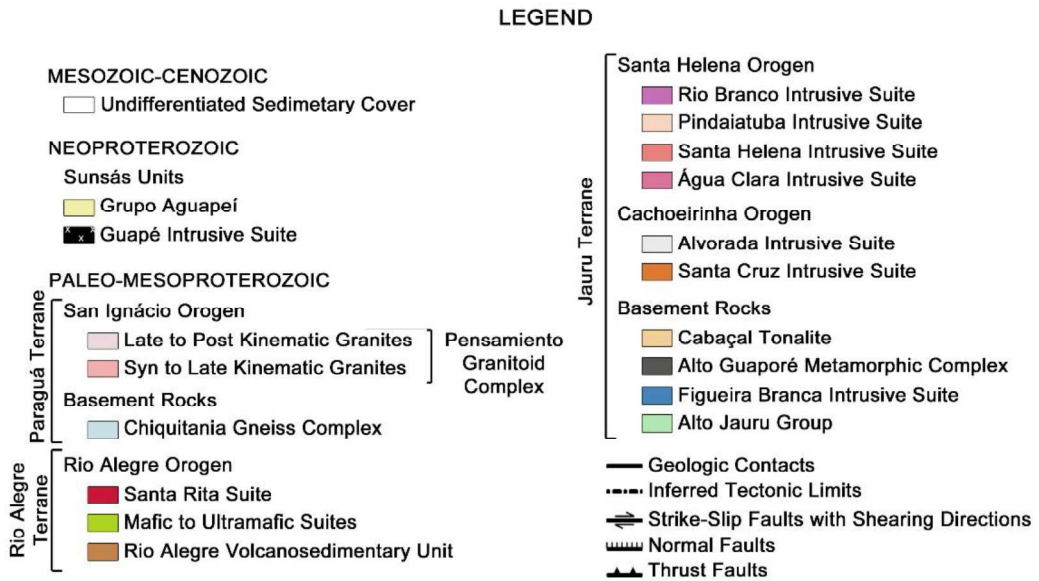
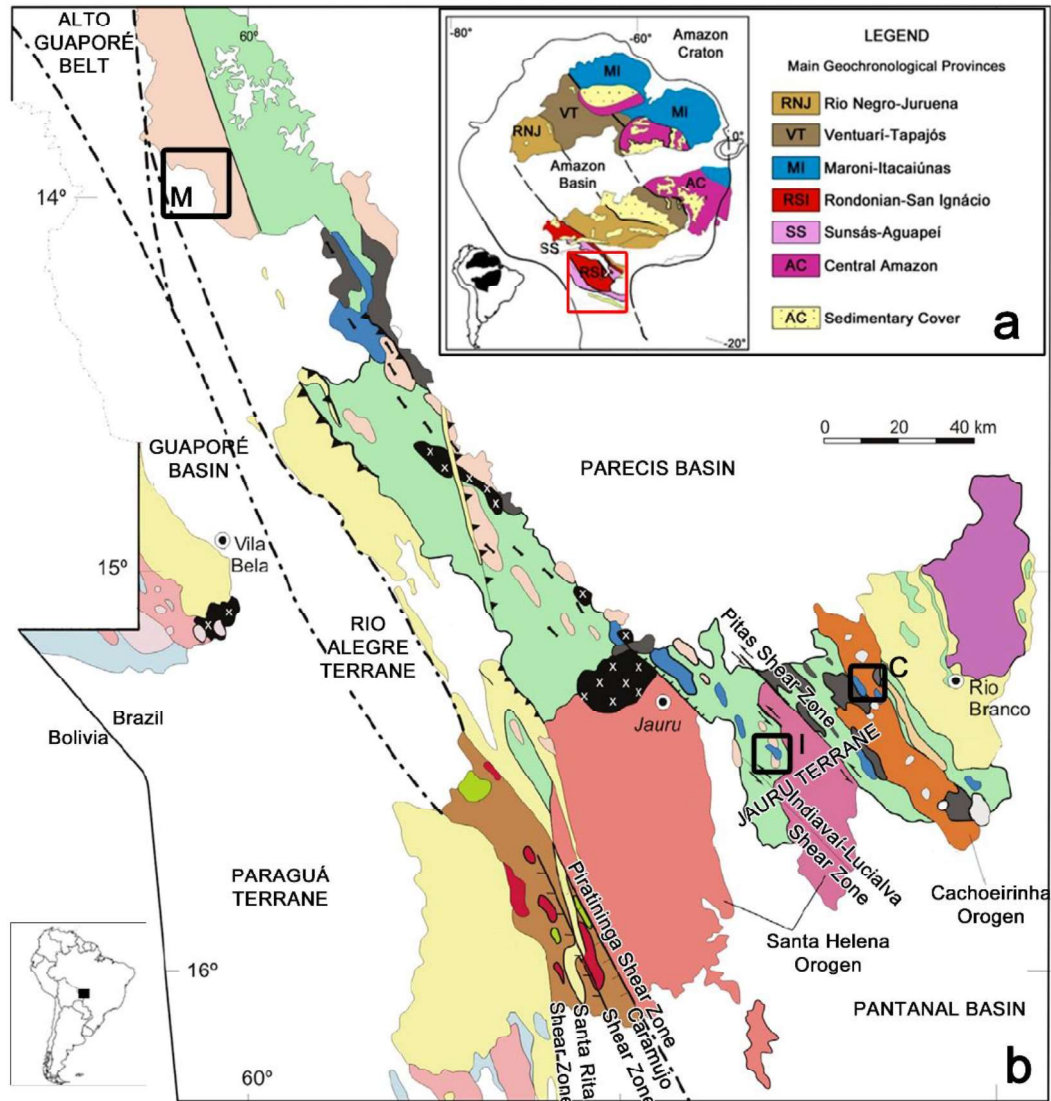
56

57 *1. Introduction*

58

59 The Amazon Craton is divisible into six geochronological provinces: Central Amazon,
60 including the stable Archean nuclei of the craton, and the Proterozoic provinces of Maroni-
61 Itacaiúnas, Ventuari-Tapajós, Rio Negro-Juruena, Rondonian-San Ignácio and Sunsás-
62 Aguapeí (Fig. 1a) (Tassinari and Macambira, 1999; Teixeira et al., 2010). The southern
63 portion of the Rio Negro-Juruena (1.78 – 1.55 Ga) province includes the Jauru Terrane (1.78
64 – 1.40 Ga), which contains Paleoproterozoic basement rocks and the Mesoproterozoic
65 Cachoeirinha and Santa Helena orogens (Fig. 1b) (Bettencourt et al., 2010). The Alto Jauru
66 Group, part of the Paleoproterozoic basement, hosts the Figueira Branca Mafic-Ultramafic
67 Suite, the focus of this paper.

68 The Figueira Branca Suite occurs in the southwest of the Mato Grosso State, Brazil, and to
69 the southwest of the Parecis Basin (Fig. 1b). Our aim is to integrate new lithological,
70 geochemical, gamma-ray and potential field data with available geological, isotope and
71 paleomagnetic data to characterize the Figueira Branca Suite and delimit the extent of this
72 Mesoproterozoic magmatic pulse.



73

74

75

Fig. 1 – (a) Main geochronological provinces of Amazon Craton (Bettencourt et al., 2010). The red polygon delimits the area of Fig. 1b. (b) Southwest of the Rio Negro-Juruena and Rondonian-San

76 Ignácio provinces of the Amazon Craton. The Figueira Branca Suite is represented in dark blue. The
77 black boxes indicate the bodies near the city of Indiavaí (I) and Cachoeirinha (C) (Bettencourt et al.,
78 2010), and the Morro do Leme and Morro do Sem-Boné mafic-ultramafic suites (M).
79

80 2. *Geologic and Tectonic Framework*

81

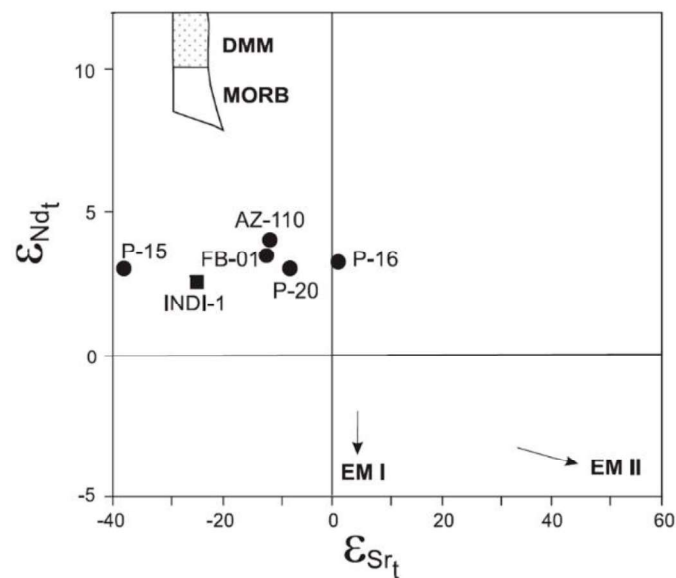
82 Cordani et al. (2010) use regional geochronological and tectonic patterns to propose that the
83 development of the southwest Amazon Craton occurred within a series of accretionary
84 orogens. This regime was responsible for the production of numerous magmatic arcs and
85 related magmatism until the late Mesoproterozoic (Teixeira et al., 2016). The Alto Jauru
86 Group and the Alto Guaporé Metamorphic Complex (Fig. 1b) compose the Jauru Terrane,
87 Rio Negro-Juruena Province (Matos et al., 2009; Souza et al., 2009). The Alto Jauru Group
88 (1760 to 1720 Ma) (Monteiro et al., 1986; (Bettencourt et al., 2010) comprises gneiss,
89 migmatites and three meta-volcanosedimentary sequences: Cabaçal, Araputanga and Jauru.
90 The Alto Guaporé Metamorphic Complex (1790 to 1740 Ma) (Menezes, 1993) is
91 characterized by granodioritic to tonalitic orthogneiss intruded into supracrustal
92 volcanosedimentary sequences, with all metamorphosed to greenschist or amphibolite facies
93 (Bettencourt et al., 2010).

94 During the evolution of the Rondonian-San Ignácio Province, the Jauru Terrane underwent
95 compressional deformation related to ocean closure, marked by the Guaporé suture and
96 collision of the Paraguá terrane (Rizzotto et al., 2013) (Fig. 01). Subduction associated with
97 ocean closure resulted in magmatic activity preserved in the Cachoeirinha (1587 to 1522 Ma)
98 and Santa Helena (1485 to 1425 Ma) orogens (Geraldes et al., 2001) and was intruded into
99 the Alto Jauru Group.

100 The Cachoeirinha orogen consists of the Alvorada (1.53 to 1.44 Ga) and Santa Cruz (1.56 to
101 1.52 Ga) intrusive suites. These suites are represented by granite, tonalite, granodiorite and
102 gneissic migmatite (Geraldes et al., 2001), and show an Andean-type arc signature with $\epsilon_{Nd(t)}$
103 values varying from -1.3 to +2.0 and T_{DM} ages of 1.9 to 1.7 Ga (Bettencourt et al., 2010;
104 Geraldes et al., 2001). The Santa Helena orogen comprises the Santa Helena (1.44 to 1.42
105 Ga), the Pindaituba (1.46 to 1.42 Ga) and the Água Clara (1.44 to 1.42 Ga) intrusive suites
106 (Ruiz, 2005). The intrusive suites of the Santa Helena Orogen consist of monzonites,

107 granodiorites and tonalites in an oceanic-continental arc setting evidenced by $\epsilon_{Nd(t)}$ values
 108 varying from +1.0 to +4.0 and T_{DM} ages of 1.8 to 1.5 Ga (Geraldes et al., 2001; Ruiz, 2005).

109 The Figueira Branca Suite is a layered mafic-ultramafic complex composed from bottom to
 110 top of dunite, pyroxenite, gabbro-norite, anorthosite, thin layers of troctolite, and olivine-
 111 gabbro (Teixeira et al., 2011). The Indiavaí gabbro from the suite yielded a U-Pb SHRIMP
 112 zircon age of 1425 ± 8 Ma (Fig. 1b, box I), and a second intrusion near Cachoeirinha city
 113 (Fig. 1b, box C) was dated at 1541 ± 23 Ma (Teixeira et al., 2011). Ar-Ar dating of biotites
 114 yielded plateau ages of 1275 ± 4 Ma and 1268 ± 4 Ma for the Indiavaí gabbro, which were
 115 evaluated as minimum ages for regional cooling. $\epsilon_{Nd(1.42 \text{ Ga})}$ values vary from +3.0 to +4.7, and
 116 $\epsilon_{Sr(1.42 \text{ Ga})}$ values from -39.1 to -8.1 indicating a predominantly juvenile source (Fig. 2). The
 117 crystallization age of the Indiavaí gabbro is coeval with the later stages of evolution of the
 118 Santa Helena Orogen (Fig. 1b) (Tassinari et al., 2000).



119
 120 Fig. 2 - $\epsilon_{Nd}(1.42 \text{ Ma})$ vs. $\epsilon_{Sr}(1.42 \text{ Ga})$ diagram of the Figueira Branca Suite (Teixeira et al., 2011).
 121

122 Our study is focused on the geological, geophysical, isotope and geochemical character of
 123 four northwest aligned intrusions of the Figueira Branca Suite between the towns of Indiavaí
 124 and Lucialva (Fig. 3). This data set provided a basis for evaluating other bodies with similar
 125 features usually associated with this suite (Fig. 1). By associating different bodies of similar
 126 geophysical signature with the Figueira Branca Suite, we were able to estimate the extent of
 127 the magmatism that generated the suite during the Mesoproterozoic and its role for the
 128 tectonic framework of the area.

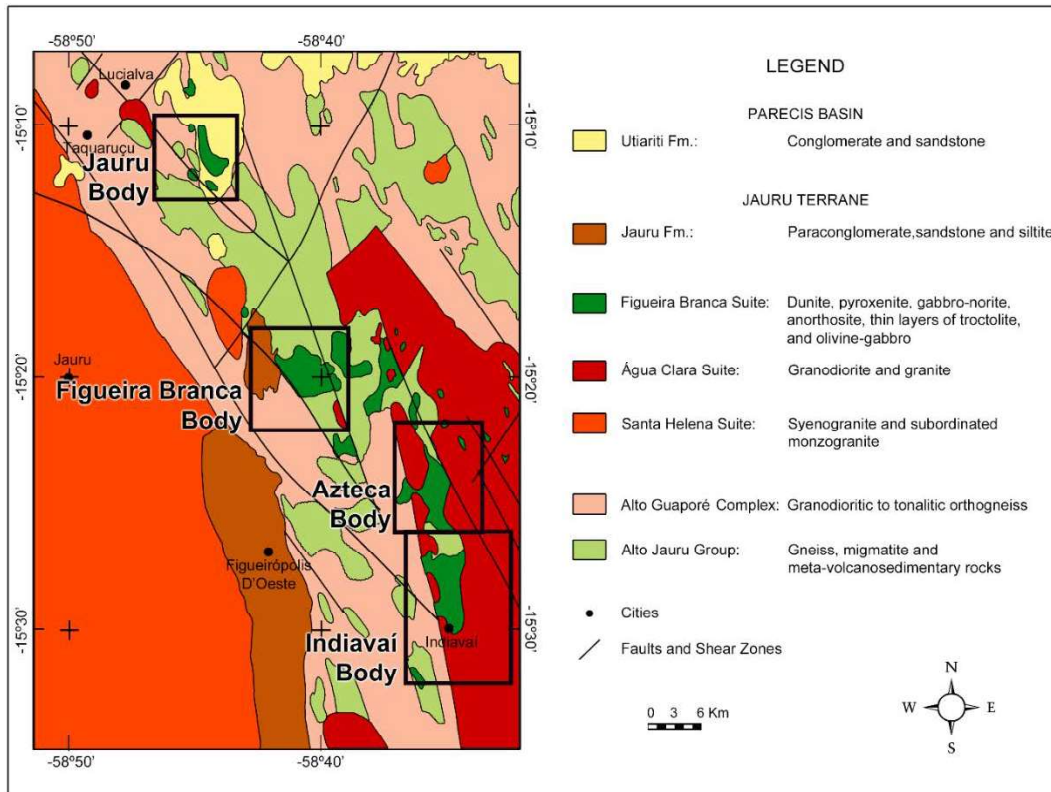


Fig. 3 – Local geological map (Nunes, 2000a; Saes et al., 1984; Teixeira et al., 2011).

130

131

132

133 Bettencourt et al. (2010) suggested rocks of the Figueira Branca Suite mafic-ultramafic suite
 134 extend north of the Santa Helena batholith. In more detailed studies, Ruiz (2005), Corrêa da
 135 Costa et al. (2009) and Girardi et al. (2012) associate the mafic-ultramafic plutons to the
 136 north of the Santa Helena batholith to the Córrego Dourado Suite (Fig. 1). This suite is made
 137 of foliated metagabbro, metatroctolite, tremolite, pyroxenite and serpentinite (Corrêa da
 138 Costa et al., 2009; Ruiz, 2005). Although there is no direct dating of the Córrego Dourado
 139 Suite, Ruiz (2005) associate the rock type and deformation of this suite to the 1439 ± 4 Ma
 140 Salto do Céu gabbroic sill (Teixeira et al., 2016).

141 Northwest of the Jauru Terrane, a set of mafic-ultramafic intrusions crops out in the Alto
 142 Guaporé Metamorphic Complex. (Nunes, 2000b) associated these bodies, the Morro do Leme
 143 and the Morro do Sem-Boné suites, to the Cacoal Suite (not mapped in Fig. 01, more
 144 outcrops are found to the north of Fig. 1). These suites are basic-ultrabasic intrusions, made
 145 up of dunites and peridotites of 1349 ± 14 Ma (Rb-Sr, whole rock) (Quadros and Rizzotto,
 146 2007).

147

148 3. *Data*

149

150 In 2006, the Brazilian Geological Service undertook a gamma-ray and magnetic field
151 airborne survey named “Projeto 1080 – Área 2 Mato Grosso” that covers the region occupied
152 by the Figueira Branca Suite. The nominal terrain clearance was 100 m at an airspeed of
153 approximately 280 Km/h. The north-south line spacing was 500 m, whereas the east-west tie
154 lines were spaced at 10000 m. The airborne survey was processed by LASA Prospecções S/A
155 and Prospectors Aerolevantamentos e Sistemas LTDA.

156 The gamma-ray data were measured with an Exploranium GR-820 Spectrometer of 256
157 channels. This spectrometer uses 5 sets of NaI (Tl) crystals, three of them downward-
158 oriented, and two upward. The downward-oriented sets are composed by two sets crystal of
159 16.8 L and one set of 8.4 L. The two upward-oriented sets contain 4.2 L crystals. The
160 sampling interval was 1 s, resulting in an observation spacing of approximately 78 m.

161 The acquisition of the magnetic field data used Geometrics G-822A Cesium magnetometers
162 of resolution of 0.001 nT. The sampling interval of 0.1 s resulted in an approximate sample
163 spacing of 7.8 m. The magnetic noise level is 0.5 nT after the industry standard corrections
164 were applied. The average International Geomagnetic Reference Field (IGRF) ambient field
165 for this period, which had an inclination -11.6° , declination 234.9° , and intensity 23749 nT.

166 195 ground gravity stations were installed in the region where the suite is emplaced. 50
167 samples of different rock types were collected for petrophysical and geochemical
168 measurements. Density data were collected by the “Archimedes method” with distilled water
169 and a high-precision analytic balance, whereas magnetic susceptibility measures were taken
170 using a Kappameter KT-9 magnetic susceptibility meter. Thin sections were prepared and
171 analysed to select samples for geochemical measurements and for constraining the
172 geophysical models. 30 samples were selected for whole-rock major elements analyses
173 through XRF, from which 20 were designed for trace and rare-earth elements analyses by
174 ICP-MS, containing specimens of the Figueira Branca Suite, Alto Jauru Group and adjacent
175 granitic suites.

176 The selected samples were powdered and homogenized as bulk material. The XRF analyses
177 were made in a Philips PW2400 XRF instrument at the Geoanalítica laboratory of the
178 Instituto de Geociências of the Universidade de São Paulo, Brazil. The trace and REE
179 analyses were made at the Laboratório de Geoquímica Analítica of the Universidade Estadual

180 de Campinas, Brazil. The samples were digested in Parr-type bombs with HF and HNO₃ mix.
 181 All solutions were prepared with ultra-pure water through the Milli-Q system. The HNO₃ was
 182 purified by sub-ebullition. The containers used on the dilutions were previously cleaned with
 183 HNO₃ (5%) and washed with ultra-pure water. The trace elements measurements used an
 184 ICP-MS XseriesII (Thermo) equipped with CCT (Collision Cell Technology). The calibration
 185 of the equipment was made using multielementary solutions gravity-prepared by
 186 monoelementary standard solutions of 100 mg/L (AccuStandards). The detection limit (DL =
 187 $\bar{x} + 3\sigma$) was determined as the average (\bar{x}) plus three standard deviations (σ) of ten
 188 measurements of the laboratory blanks and the instrument background. The quality control
 189 used the reference materials BRP-1 (basalt) and GS-N (granite) from the Laboratório de
 190 Geoquímica Analítica. The results and their respective uncertainties for the eleven samples
 191 from the Figueira Branca Suite rocks are available in Table 1.

192 Table 1 – XRF and ICP-MS results for the Figueira Branca Suite.

XRF Results (%)													
Sample	IND03	IND06	IND09	IND10	AZT05	AZT10	FIG01	FIG02	FIG03	JAU01	JAU02	DL	Error (±)
SiO ₂	47.09	46.96	47.79	47.04	50.97	48.39	48.89	39.64	40.74	49.48	50.18	0.03	0.48
TiO ₂	0.41	0.35	0.26	0.28	0.57	0.42	0.22	0.06	0.08	0.28	0.55	0.003	0.009
Al ₂ O ₃	20.48	23.95	21.72	20.7	18.37	18.1	6.15	9.39	18.13	21.18	17.62	0.02	0.09
Fe ₂ O ₃	9.89	6.52	8.04	9.08	8.25	8.45	9.31	11.3	6.64	7.7	9.36	0.01	0.09
MnO	0.14	0.09	0.11	0.12	0.14	0.13	0.17	0.15	0.09	0.1	0.14	0.002	0.003
MgO	9.01	7.09	8.79	9.83	7.27	5.67	22.96	26.97	16.26	7.66	10.56	0.01	0.06
CaO	10.27	12.35	11.02	10.3	9.43	10.5	7.89	4.92	9.4	10.02	8.73	0.01	0.02
Na ₂ O	2.38	2.13	2.46	2.36	2.75	2.22	0.32	0.33	1.13	2.76	2.37	0.02	0.12
K ₂ O	0.12	0.11	0.11	0.12	0.38	0.81	0.21	0.03	0.03	0.19	0.24	0.01	0.01
P ₂ O ₅	0.03	0.03	0.01	0.02	0.04	0.02	0.12	0.01	0.01	0.01	0.11	0.003	0.003
LOI	<0.01	0.86	0.1	0.16	1.48	5.72	5.28	7.98	6.98	0.16	0.2	0.01	---
Total	99.81	100.44	100.41	100.02	99.65	100.43	101.52	100.78	99.49	99.54	100.06	---	---
ICP-MS Results (mg.g ⁻¹)													
Sample	IND03	IND06	IND09	IND10	AZT05	AZT10	FIG01	FIG02	FIG03	JAU01	JAU02	DL	Error (±)
Cu	89.1	---	32.5	---	74.3	35.3	4.89	32.0	12.9	46.6	42.6	3	0.2
Nb	0.52	---	0.37	---	1.53	0.75	0.61	0.32	1.33	0.20	1.38	0.9	0.05
Rb	4.31	---	3.58	---	11.4	13.8	0.93	0.94	0.81	3.55	3.41	1	0.2
Sr	238	---	236	---	218	218	178	137	225	522	458	6	0.07
Zn	55.9	---	46.1	---	59.2	45.9	58.7	63.1	41.4	52.3	71.5	2	3.4
Zr	17.4	---	13.4	---	42.8	22.6	13.0	3.30	5.13	4.74	32.9	5	0.04
Cr	17.2	---	32.5	---	390	103	1703	136	1184	137	609	1	0.4
Ba	41.7	---	39.0	---	85.5	71.6	8.47	24.9	28.0	112	154	7	0.08
Ni	202	---	160	---	40.7	49.6	1054	1112	720	168	175	0.9	0.2
Be	0.15	---	0.09	---	0.35	0.23	0.39	0.06	0.04	0.16	0.32	0.1	0.04

V	100	---	65.6	---	139	134	110	19.8	26.9	69.7	112	7	0.1
Co	56.8	---	52.9	---	40.3	39.3	82.9	125	70.7	50.7	54.1	1.4	0.02
Ga	16.3	---	15.9	---	19.0	17.1	5.65	5.99	10.6	16.3	15.3	0.6	0.009
Y	8.87	---	6.19	---	14.7	10.6	5.43	1.56	1.77	3.12	8.85	1	0.02
Mo	0.10	---	0.08	---	0.28	0.14	0.13	0.08	0.08	0.06	0.15	0.1	0.02
Sn	0.14	---	0.06	---	0.32	0.19	0.06	<DL	<DL	<DL	0.14	0.4	0.08
Sb	0.03	---	0.02	---	0.14	0.10	0.39	0.01	0.01	0.01	0.01	0.01	0.01
Cs	0.06	---	0.05	---	0.83	0.40	0.02	0.14	0.15	0.11	0.19	0.02	0.004
Hf	0.53	---	0.42	---	1.20	0.69	0.35	0.09	0.13	0.16	0.81	0.2	0.005
Ta	0.05	---	0.09	---	0.12	0.05	0.05	0.09	0.40	0.03	0.08	0.08	0.003
Pb	0.57	---	0.51	---	1.78	1.47	1.09	0.28	0.25	0.67	1.04	0.3	0.05
Bi	0.03	---	0.03	---	0.04	0.08	0.06	0.02	0.02	0.02	0.02		0.006
Th	0.28	---	0.22	---	0.85	0.33	0.46	0.14	0.05	0.05	0.14	0.1	0.003
U	0.08	---	0.05	---	0.39	0.12	0.33	0.19	0.06	0.01	0.08	0.03	0.03
La	1.82	---	1.47	---	5.31	2.70	4.02	0.96	0.90	1.57	5.08	1	0.01
Ce	4.13	---	3.28	---	11.5	6.16	8.37	1.75	1.99	3.02	11.7	1.2	0.02
Pr	0.60	---	0.46	---	1.51	0.87	1.15	0.24	0.27	0.37	1.60	0.2	0.006
Nd	2.95	---	2.20	---	6.77	3.97	4.85	0.93	1.10	1.66	6.98	0.9	0.009
Sm	0.98	---	0.69	---	1.78	1.17	1.08	0.21	0.27	0.45	1.61	0.2	0.007
Eu	0.49	---	0.46	---	0.63	0.60	0.28	0.14	0.19	0.47	0.71	0.08	0.003
Gd	1.13	---	0.80	---	1.96	1.36	1.03	0.21	0.27	0.44	1.57	0.3	0.006
Tb	0.22	---	0.16	---	0.36	0.26	0.16	0.03	0.05	0.07	0.26	0.05	0.003
Dy	1.57	---	1.10	---	2.56	1.88	0.98	0.26	0.31	0.53	1.61	0.3	0.003
Ho	0.36	---	0.24	---	0.54	0.40	0.20	0.05	0.07	0.11	0.34	0.06	0.003
Er	0.96	---	0.67	---	1.56	1.17	0.53	0.14	0.18	0.31	0.94	0.1	0.004
Tm	0.14	---	0.10	---	0.22	0.17	0.08	0.02	0.03	0.05	0.13	0.02	0.02
Yb	0.91	---	0.60	---	1.44	1.05	0.51	0.17	0.18	0.34	0.86	0.09	0.005
Lu	0.14	---	0.10	---	0.22	0.17	0.08	0.03	0.03	0.05	0.14	0.02	0.002
Sc	14.7	---	13.5	---	27.2	29.2	21.3	5.95	4.74	12.2	20.3	0.8	1.4
Li	4.20	---	7.44	---	8.97	5.31	1.39	3.72	2.68	5.68	5.76	0.3	0.03
Cd	0.07	---	0.05	---	0.09	0.07	0.05	0.01	0.01	0.07	0.07	0.1	0.02

193

194 *4. Results & Discussion*

195

196 *4.1. Typical Magnetic Field Signature and Bodies Associated with the Suite*

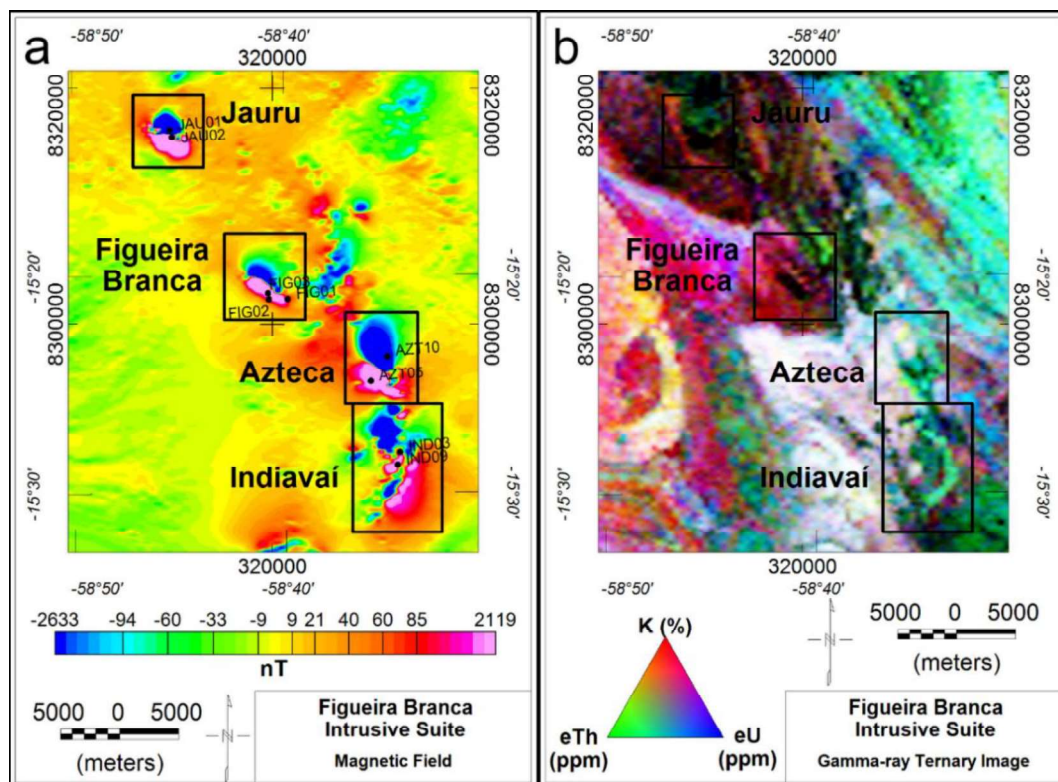
197

198 Initial data analysis used magnetic field method and the gamma-ray spectrometry to establish
199 the geophysical signature of the Figueira Branca Suite and delineate analogue anomalies
200 within the Jauru Terrane. The “Projeto 1080 – Área 2 Mato Grosso” provided a regional data
201 set of magnetization contrasts and gamma-ray emissions (Fig. 4). The four recognized bodies

202 of the Figueira Branca Suite display significant contrasts of magnetization with their
 203 respective host-rocks, generating magnetic anomalies in the total magnetic field map (Fig.
 204 4a). The intrusions were named, from the south to north, Indiavaí, Azteca, Figueira Branca
 205 and Jauru. These anomalies show a specific pattern with negative values to the north and
 206 positive to the south, indicating the presence of a significant remanent magnetization in their
 207 sources. The gamma-ray emission for the areas of the four bodies indicated discrete low
 208 counts (dark to black areas in Fig. 4b), typically associated with mafic rocks (Dickson and
 209 Scott, 1997). The Indiavaí and Azteca bodies show the general low counts pattern, but have
 210 higher concentrations of eTh and eU than their northern counterparts. The higher
 211 concentration of both elements produces a cyan coloration in the area of the bodies.

212 A group of small occurrences associated to the Figueira Branca Suite is found to the east of
 213 the Figueira Branca anomaly and to the north of Azteca (Fig. 4a). This anomaly shows a low
 214 trend of gamma-ray counts (Fig. 4b) as expected for mafic rocks, however the magnetic
 215 signature differs grandly from the other anomalies linked with the suite.

216



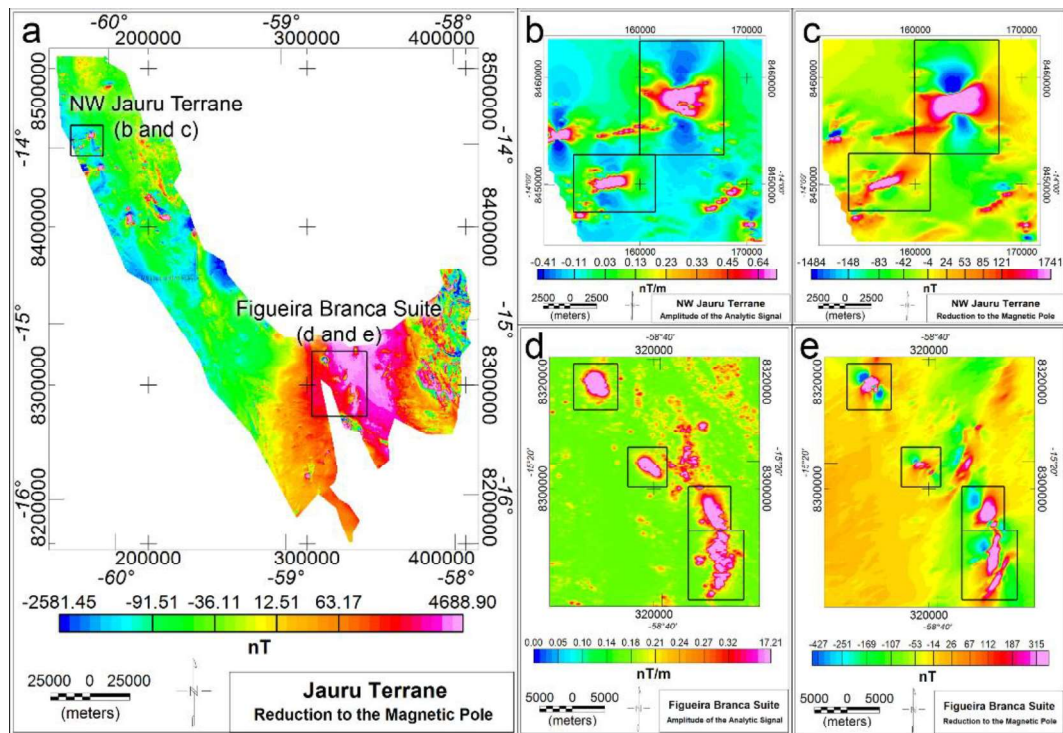
217

218 Fig. 4 - (a) Total magnetic field of the area of the Figueira Branca Suite, including the location of the
 219 samples associated to the intrusive suite. (b) Gamma-ray emission of the area.

220

221 The magnetic field and gamma-ray emissions were used as proxies to investigate for
222 additional mapped and unmapped intrusions related with the Figueira Branca Suite. To use
223 the magnetic field as a proxy, we applied the Reduction to the Magnetic Pole (RTP) operator
224 to estimate the direction of total magnetization of the anomalies. A successful RTP filtering
225 results in a magnetic field where the anomalies present positive contrasts centred over the
226 limits of the bodies, as the negative values on the map are close to zero. The RTP filtering
227 requires knowledge of the direction of total magnetization of the field. Hence, it is
228 recommended to use of this filtering in areas with magnetic anomalies predominantly
229 generated by the induced magnetization, where its direction is known by the geomagnetic
230 field in the area during the survey. Fedi et al. (1994) and Cordani and Shukowsky (2009)
231 proposed and implemented, respectively, a technique called MaxiMin, which does an
232 inversion of the inclination and declination to estimate the values that better minimize the
233 negative values of the field and maximize the positive values. The MaxiMin optimal results
234 were inclination of 56° and declination of 213° , with an α_{95° of 5° after 386 iterations. Figure
235 5a shows the RTP field of the Jauru Terrane with the targets found with the analogue
236 characteristics of gamma-ray emission and/or magnetization. In order to define the lateral
237 limits of the bodies and evaluate qualitatively the MaxiMin results, we used the 3-D
238 Amplitude of the Analytic Signal (Fig. 5b and d) (Roest et al., 1992).

239



240
241
242
243
244
245

Fig. 5 – (a) RTP of the Jauru Terrane identifying bodies with similar features as those already recognized as part of the Figueira Branca Suite. (b) and (c) are the Amplitude of the Analytic Signal and the RTP, respectively, of the anomalies in the northwest of the Jauru Terrane, while (d) and (e) are the same maps, respectively, for the Figueira Branca Suite.

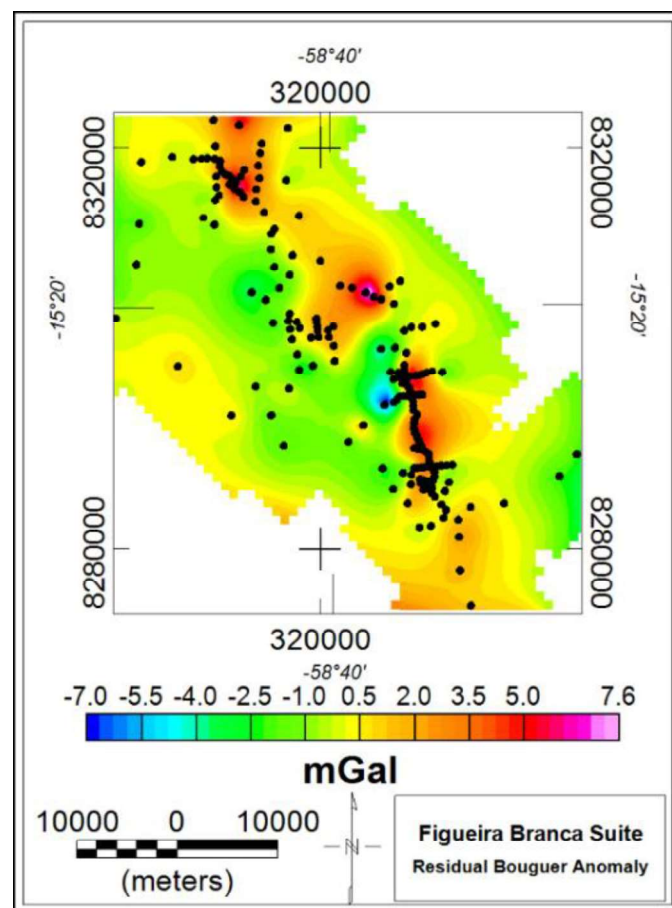
246
247
248
249
250
251
252
253
254
255
256
257
258
259

In the northwest of the Jauru Terrane, a set of other gamma-ray and/or magnetic anomalies presented similar geophysical signature inside the Jauru Terrane. The only two anomalies in the northwest that were properly reduced to the pole were spatially associated with the Morro do Leme and the Morro do Sem-Boné complexes (Fig. 1, 5b and c). These intrusive complexes are associated to Cacoal basic-ultrabasic intrusive suite and hosted by the Alto Guaporé Belt (Nunes, 2000b). The RTP of both complexes present similar shapes, indicating analogue direction of total magnetization. Louro et al. (2014) suggest a remanent magnetization with inclination of 41.8° and declination of 193° for the Morro do Leme. Therefore, in the absence of analogue geophysical signatures unrelated with known suites in the Jauru Terrane, we focused on characterizing the Figueira Branca Suite using the only the four recognized bodies that maintained the same signature on different and independent geological and geophysical data.

260 4.2. Gravity Field

261

262 The gravity field of the region showed three of the four gravity anomalies (Fig. 6). The
263 Figueira Branca anomaly could not be properly surveyed due to flooding over the northern
264 part of the body due to construction of a dam. The irregular distribution of gravity stations
265 allied with a regional trend of the gravity field requiring regional-residual separation. We
266 isolated the gravity anomaly signatures using a high-pass filter to remove wavelengths larger
267 than 24400 Km. The cut-off wavelength was defined based on the first inclination change of
268 the energy spectrum. The anomalies showed good spatial correlation with the magnetic field
269 data and their maximum amplitudes varied from 1.6 (in the Figueira Branca magnetic
270 anomaly area) to 7.6 mGal.



271

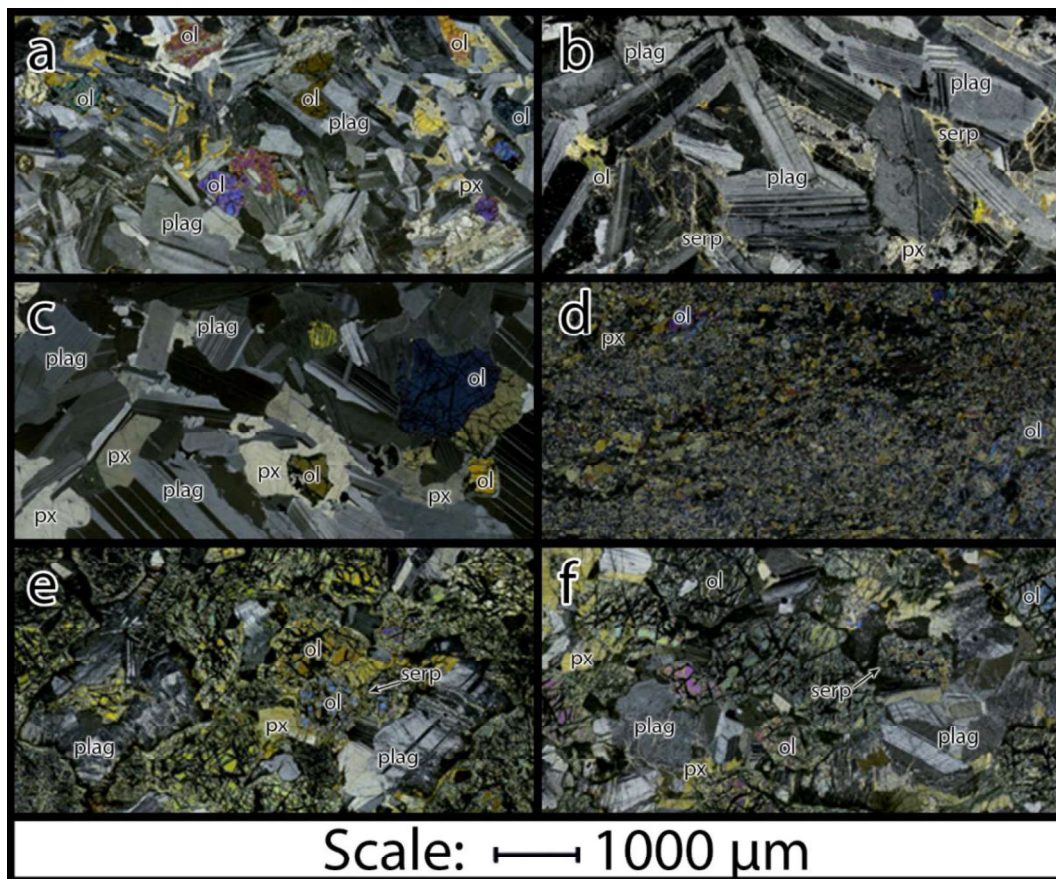
272 Fig. 6 – Residual Bouguer anomaly map of the Figueira Branca Suite. The black circles represent the
273 location of the gravity stations.

274

275

277

278 Mineralogy of the Indiavaí, Azteca and Jauru bodies is dominated by plagioclase (ca. 60% to
 279 70%) with fractured and serpentinized olivine (ca. 20% to 25%) and intergrown pyroxene
 280 (ca. 10% to 15%) (Fig. 7a, 7b and 7c). The Figueira Branca intrusion shows variable grain
 281 size with parts relatively fine grained and displaying significant serpentinization and
 282 weathering (Fig. 7d), whereas other sections are coarse grained and contain a higher
 283 proportion of olivine (ca. 60% olivine and ca. 40% plagioclase; Fig 7e and 7f). Opaque oxide
 284 minerals are present in all thin sections. D'Agrella-Filho et al. (2012) determined the opaque
 285 oxide phase as magnetite in the Indiavaí gabbro.



286

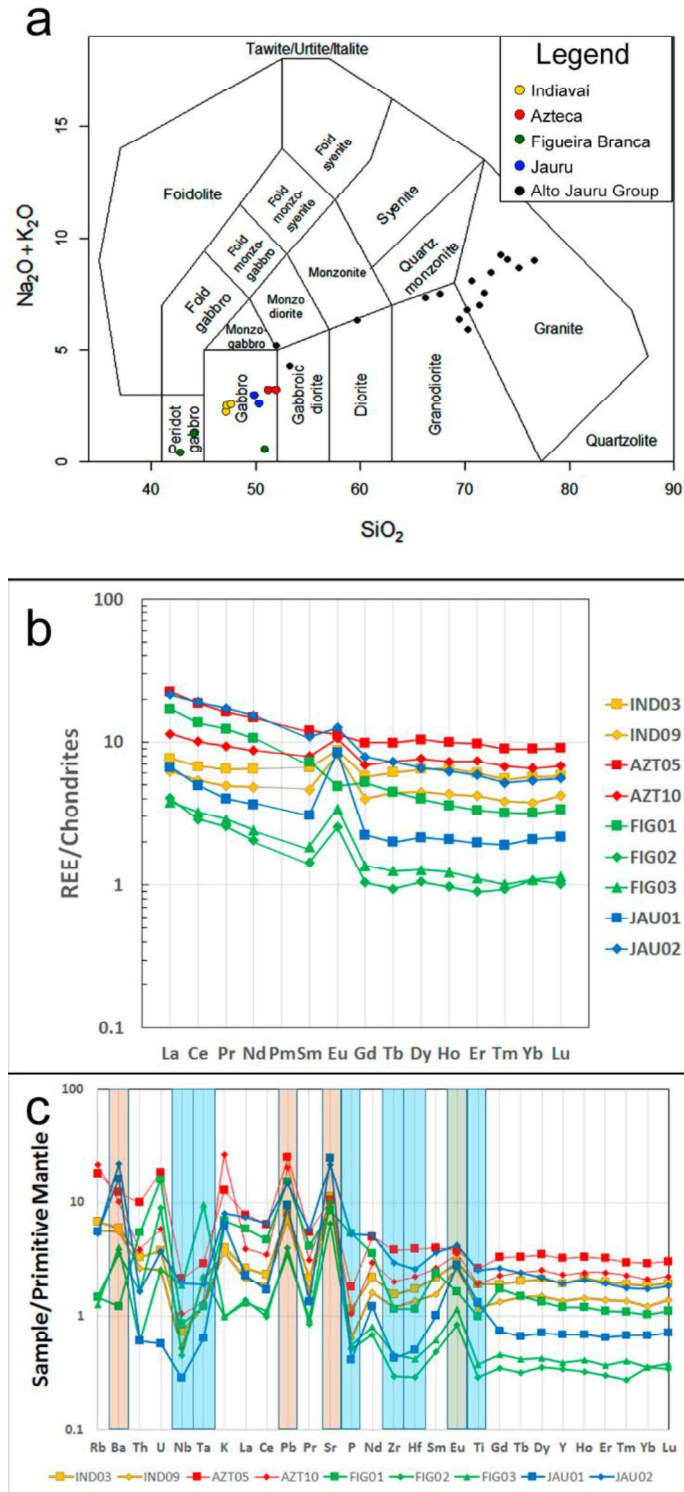
287 Fig. 7 – Thin sections of the samples (a) IND09, (b) AZT05, (c) JAU01, (d) FIG01, (e) FIG02 and (f)
 288 FIG03. The crystals are indicated by their abbreviations: ol – olivine, plag – plagioclase, px –
 289 pyroxene, and serp – serpentine. All photos were taken with cross-polarized light.

290

291 Geochemical data were collected on 11 samples (Table 1). On a TAS (SiO₂ vs. NaO₂ + K₂O)
 292 plot (Fig. 8a) (Middlemost, 1994), these samples were located inside the gabbro field, with

293 the exception of two out of three olivine-rich samples from the Figueira Branca intrusion
294 (FIG01 and FIG02) that showed significantly lower values of SiO₂ and Na₂O+K₂O and were
295 located in the peridotite-gabbro field (Fig. 8a).

296 The REE normalized to chondrites (McDonough and Sun, 1995) shows the increase in the
297 slopes among the intrusions, from lower to higher: Indiavaí, Figueira Branca, Azteca and
298 Jauru (Fig. 8b). The increase in the slopes indicate the evolution of the magma of the Figueira
299 Branca Suite, with the Jauru body representing the most, and the Indiavaí intrusion the least,
300 evolved. The majority of the samples display Eu anomalies consistent with the presence of
301 plagioclase (Fig. 7).



302

303

304

305

306

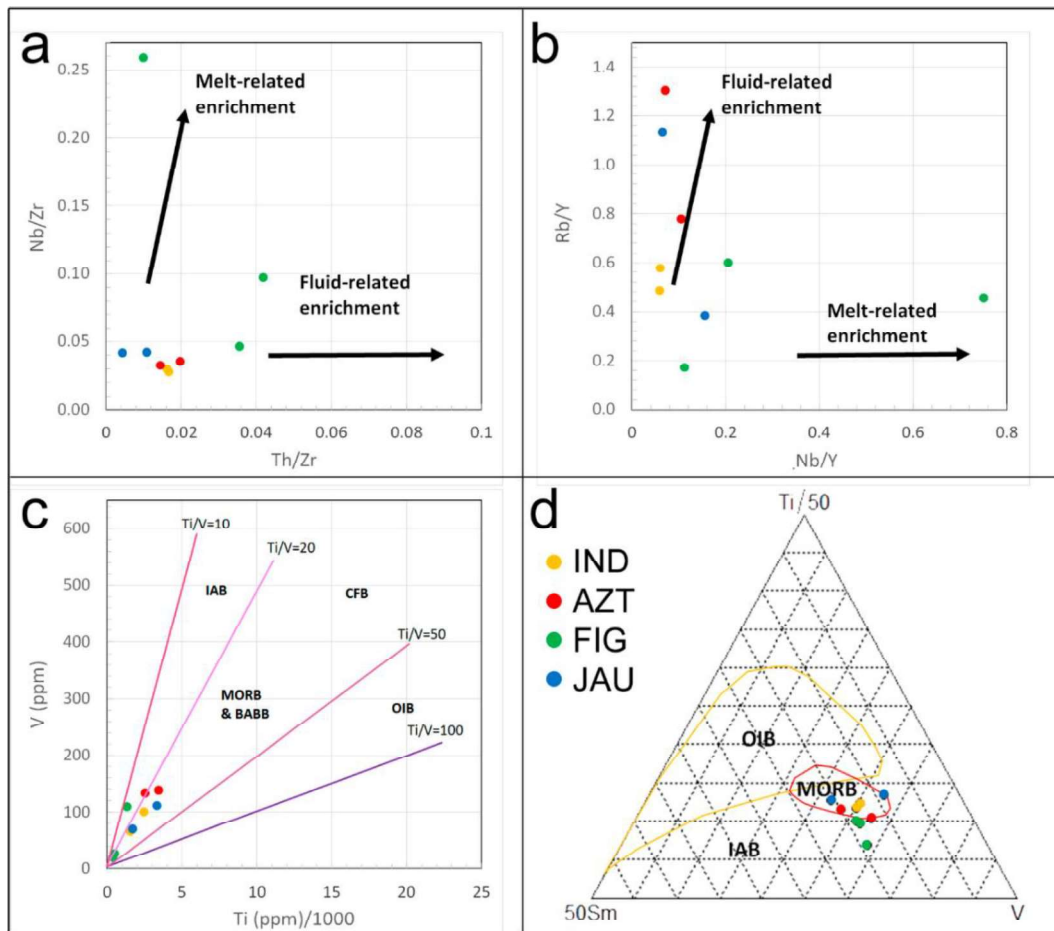
Fig. 8 – (a) TAS (SiO₂ vs. Na₂O + K₂O) plot (Middlemost, 1994), (b) REE normalized to the chondrite values (McDonough and Sun, 1995) and trace elements normalized to Primitive Mantle (Sun and McDonough, 1989) of the Figueira Branca Suite.

307 According with Zheng (2012), Pb and Sr positive anomalies on a Primitive Mantle
308 normalized spidergram (Sun and McDonough, 1989) are associated to metasomatism in
309 subduction zones before the melting of the parental magma (Fig 8c). Two types of
310 metasomatized media are possible in these zones: a media characterized by slab-derived
311 fluids and one by hydrous melt. The first has high capacity to transport water-soluble
312 elements, but not water-insoluble. Hydrous melts, however, can transport both water-soluble
313 and insoluble elements. Rb/Y, Nb/Y, Nb/Zr and Th/Zr ratios can be used as proxies to
314 suggest the type of metasomatized media (Kepezhinskias et al., 1997). The mafic samples of
315 the Figueira Branca Suite indicated high values of Rb/Y and Th/Zr, and lower values of Nb/Y
316 and Nb/Zr (Fig. 9a and 9b), indicating a hydrous melt predominance in the parental magma.
317 The samples of the Figueira Branca intrusion showed significantly different Th/Zr and Nb/Zr
318 ratios than the remaining samples from the suite. This behaviour follows the contrast
319 observed on the mineralogy (Fig. 7c) and REE slopes (Fig. 8b) of these samples.

320

321

322



323

324 Fig. 9 – Petrogenetic diagrams (a) Nb/Zr vs. Th/Zr, and (b) Rb/Y vs. Nb/Y (Kepezhinskas et al.,
 325 1997), and tectonic discriminant (c) V vs. Ti/1000 (Shervais, 1982), and (d) ternary Ti/50 vs. Sm*50
 326 vs. V (Vermeesch, 2006) of the Figueira Branca Suite.

327

328 Pronounced Zr and Hf negative anomalies for the Figueira Branca Suite samples (Fig.
 329 8c) is indicative of a supra-subduction setting (Wang et al., 2013) and consistent with the
 330 Rb/Y, Nb/Y, Nb/Zr and Th/Zr ratios (Fig. 9a and b). The samples show Ti/V ratios
 331 ($10 > \text{Ti}/\text{V} > 30$) (Fig. 9c) related with MORB and Back-Arc Basin Basalts (BABBB) (Shervais,
 332 1982), whereas in the ternary Ti-Sm-V diagram (Vermeesch, 2006) (Fig. 9d), they fall in the
 333 transitional field between MORB and IAB. Vermeesch (2006) explains that the multiplying
 334 factors in the Ti-V and Ti-Sm-V diagrams are used because geochemical data is expressed as
 335 parts of a whole, so the concentration of some elements are not entirely independent to vary
 336 without interfering in the concentration of others in the same system.

337 The Figueira Branca Suite lies to the east of the Santa Helena orogen and to the west of
 338 the Água Clara orogen (Fig. 1), two structures originated by the subduction of oceanic crust

339 to the west of the Santa Helena orogen. These features, along with the $\epsilon_{Nd}(1.42 \text{ Ma})$ vs.
 340 $\epsilon_{Sr}(1.42 \text{ Ga})$ signature (Fig. 3), suggest that the Figueira Branca parental magma, originally
 341 depleted, metasomatized during and/or after the subduction of the same ocean crust that
 342 resulted in the Santa Helena and Água Clara orogens. Furthermore, the location of the suite
 343 between orogens and the parallel alignment of the geophysical anomalies with the extinct
 344 subduction zone, in an extensive environment (Teixeira et al., 2011), suggests a tectonic
 345 framework of back-arc magmatism.

346

347 4.4. Magnetic and Gravity Modelling

348

349 Density and magnetic susceptibility were measured on samples of the Figueira Branca Suite
 350 and adjacent rocks (Table 2). These values, along with the total field direction estimated by
 351 the MaxiMin technique (inclination 56° and declination of 213°), were used as constraints to
 352 develop magnetic and gravity models for the four anomalies of the Figueira Branca Suite. We
 353 adapted the methodology of staged inversion of Foss (2006) for the available dataset. First,
 354 we created outcropping block models with lateral limits based on the amplitude of the
 355 analytic signal over the magnetic field data. To each of these models were attributed the total
 356 magnetization direction, the average magnetic susceptibility and density (Table 2). The
 357 ambient magnetic field was defined by the IGRF by the time of the survey (inclination -11.6° ,
 358 declination 234.9° , and intensity 23749 nT). The significantly smaller number and mostly
 359 irregularly distributed gravity data, was modelled as a secondary parameter which we
 360 allowed larger root mean square (RMS) errors (less than 20%) than to the magnetic field (less
 361 than 10%).

362 Table 2 - Measured average density and magnetic susceptibility of the four bodies of the Figueira
 363 Branca Suite.

Body	Average Density (g/cm³)	Average Magnetic Susceptibility (SI)
Indiavaí	2.93888 ± 0.0001	0.043 ± 0.003
Azteca	2.91945 ± 0.0001	0.065 ± 0.004
Figueira Branca	2.84133 ± 0.0001	0.054 ± 0.004
Jauru	3.02962 ± 0.0001	0.066 ± 0.005

364

365

366 The staged inversion varied the following parameters at each stage: (1) the amplitude of the
367 total magnetization, and depth extent of the block model; (2) the amplitude of the total
368 magnetization, depth extent and horizontal position; (3) the amplitude of the total
369 magnetization, depth extent, horizontal position and vertices movements in north-south
370 direction; (4) the parameters of the previous stage plus the vertices movements in east-west
371 direction; and (5) all the previous parameters plus the magnetic susceptibility. By the end of
372 the first staged inversion, the body was subdivided in 500 m north-south oriented polygonal
373 prisms centred over the surveyed flight lines and the process was reinitiated to optimize the
374 results, with two differences: instead varying the depth extent in all stages, the vertices were
375 allowed to vary their positions on vertical direction, and the stage (4) was skipped. The third
376 and last pass of inversion permitted the variation of the density of the models, with the
377 modelling based on profiles of the Bouguer anomalies of the Figueira Branca Suite bodies
378 (Figs. 10 and 11).

379 The models achieved low RMS errors both for the magnetic and gravity data (Table 2). The
380 maps comparing the observed, modelled and residual fields are shown in Figure 10. The
381 modelled Azteca magnetic anomaly (Fig. 10b) showed higher amplitudes in the south of the
382 map unrelated to any model. We attributed the higher amplitude to border effects due to
383 interpolation of the modelled data. The observed Bouguer anomaly profiles are compared
384 with the modelled profiles in figure 11. The residual fields presented low amplitudes when
385 compared with the amplitude of the anomalies in the observed fields (see the RMS in Table
386 3). Although the average magnetic susceptibility and average density were used as constraints
387 for the modelling, we allowed their variation during the last stages of the inversion due the
388 small number of fresh samples available. The measured and the modelled values remained
389 the same after the inversion (Tables 2 and 3). The modelled amplitude of the total
390 magnetization varied from 2.8 to 8.6 A/m². These amplitudes, attributed to their respective
391 directions obtained through the MaxiMin RTP, enabled the determination of the total
392 magnetization vectors for the sources of the anomalies. The measured and modelled magnetic
393 susceptibilities, with the characteristics of the ambient field given by the IGRF, permitted the
394 estimation of the induced magnetization vectors on the Figueira Branca Suite modelled
395 bodies. Subtracting the total by the induced magnetization vector of each model, we
396 estimated their remanent magnetization vectors. The calculated remanent magnetization for
397 the four anomalies were quite similar as seen in Table 2. Their directions approximate the

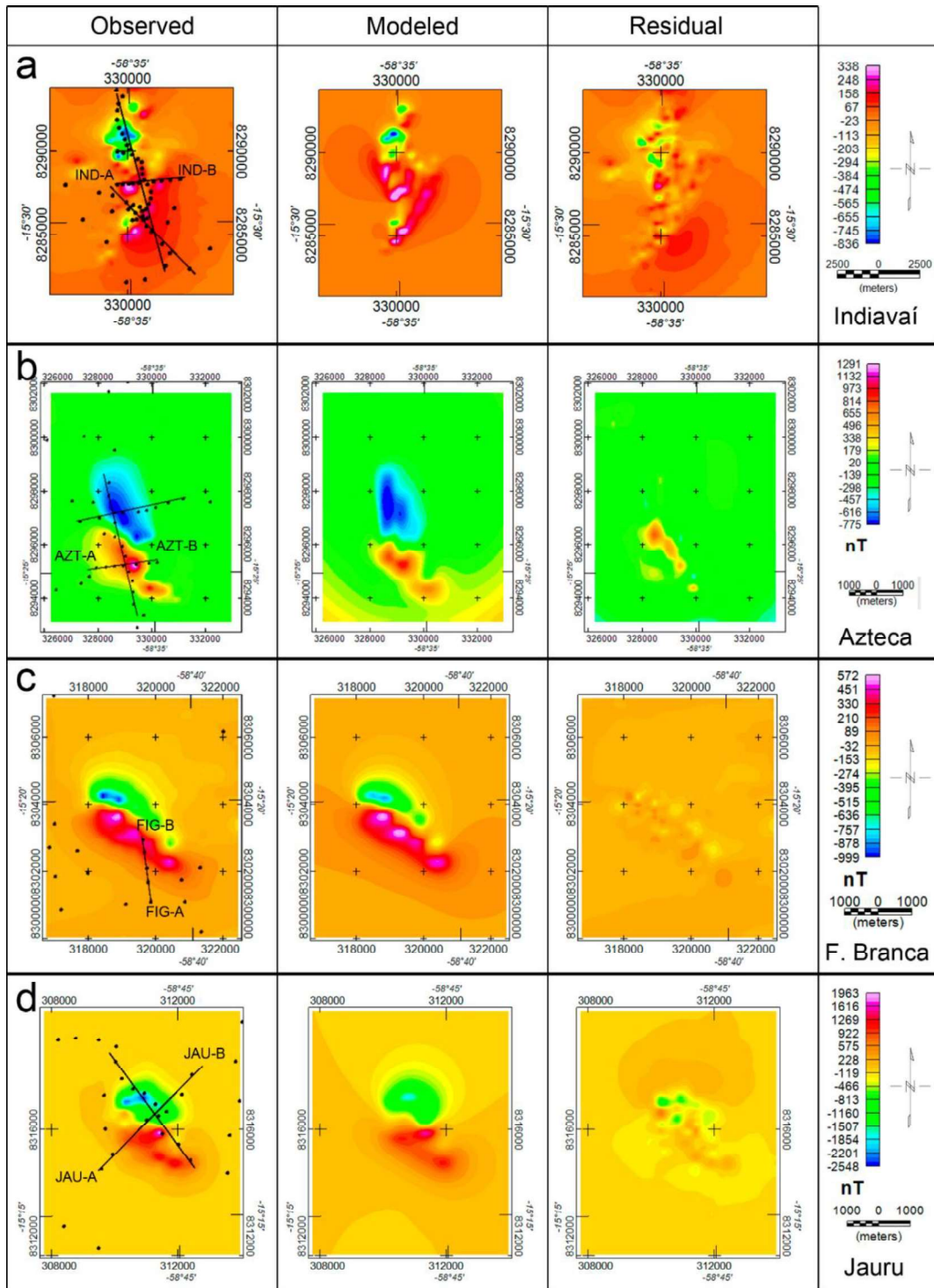
398 average remanent magnetization direction of the Indivaí gabbro reported by D'Agrella-Filho
 399 et al. (2012) with inclination 50.7°, declination 209.8°, and α_{95}^0 8.0.

400

401

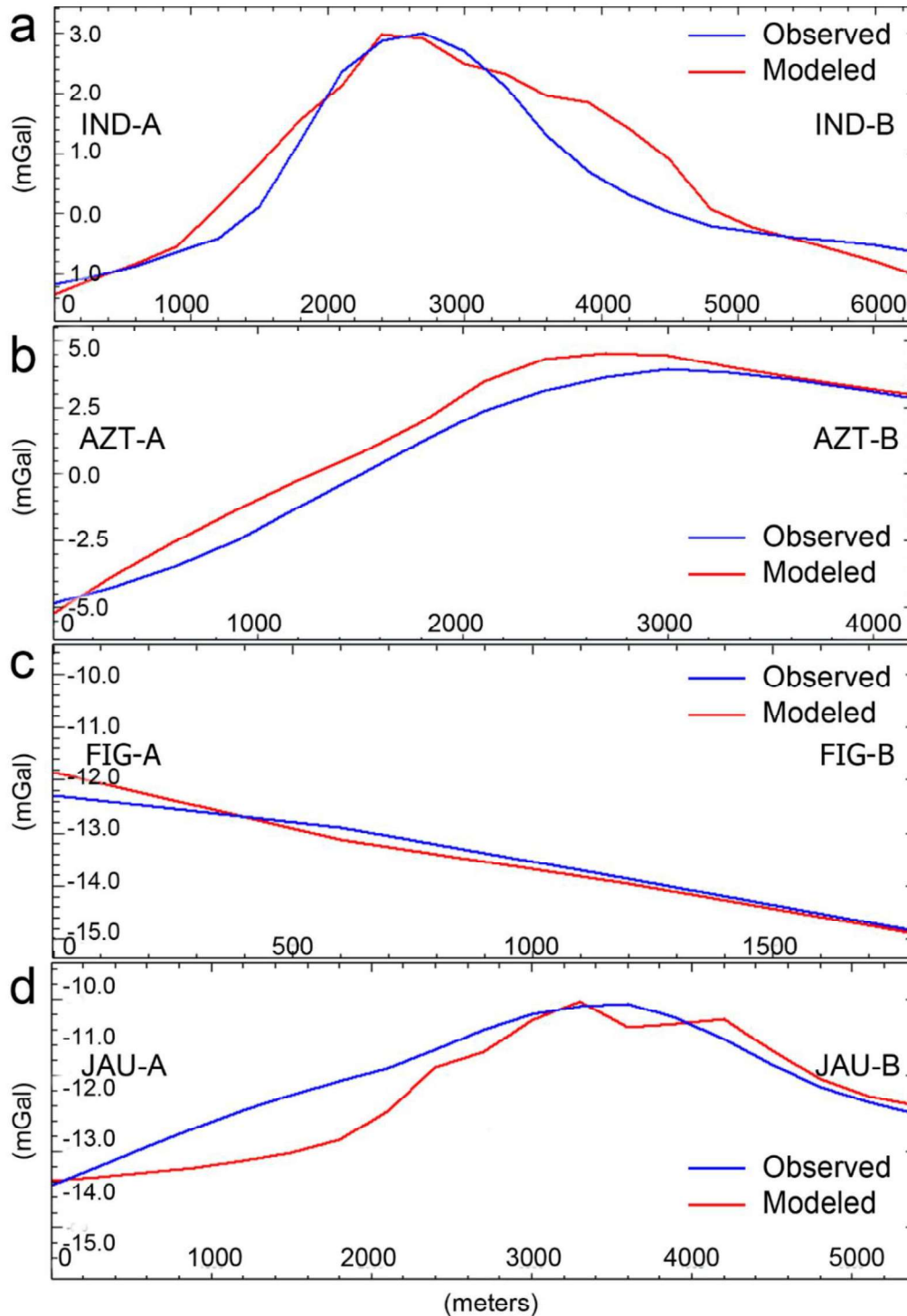
Table 3 - Features and RMS values of the models of the Figueira Branca Suite.

Geophysical Models			
Alto Jauru Group (Host-rock)			
Samples			
Avg. Mag. Suscep.	0.007 (SI)	# of Samples	36
Avg. Density	2.70 g/cm ³		
Indivaí			
Samples			
Avg. Mag. Suscep.	0.05 (SI)	# of Samples	6
Avg. Density	2.94 g/cm ³		
Magnetic and Gravity Fields Inversions			
Magnetization	Induced	Total	Remanent
Inclination (°)	-11.6	56	49.6
Declination (°)	346.9	213	199.5
Intensity (A/m)	0.9	3.8	4.4
RMS-Mag (%)	5.8	# of Points	29003
RMS-Grav (%)	18.9	# of Points	89
Azteca			
Samples			
Avg. Mag. Suscep.	0.07 (SI)	# of Samples:	2
Avg. Density	2.91 g/cm ³		
Magnetic and Gravity Fields Inversions			
Magnetization	Induced	Total	Remanent
Inclination (°)	-11.6	56	51.2
Declination (°)	346.9	213	191.8
Intensity (A/m)	1.3	8.6	9.5
RMS-Mag (%)	6.4	# of Points	9251
RMS-Grav (%)	12.1	# of Points	37
Figueira Branca			
Samples			
Avg. Mag. Suscep.	0.06 (SI)	# of Samples:	3
Avg. Density	2.84 g/cm ³		
Magnetic and Gravity Fields Inversions			
Magnetization	Induced	Total	Remanent
Inclination (°)	-11.6	56	45.9
Declination (°)	346.9	213	194
Intensity (A/m)	1.1	2.8	3.6
RMS-Mag (%)	3.7	# of Points	19206
RMS-Grav (%)	10.8	# of Points	17
Jauru			
Samples			
Avg. Mag. Suscep.	0.07 (SI)	# of Samples:	3
Avg. Density	3.02 g/cm ³		
Magnetic and Gravity Fields Inversions			
Magnetization	Induced	Total	Remanent
Inclination (°)	-11.6	56	51.6
Declination (°)	346.9	213	202.9
Intensity (A/m)	1.3	7.8	8.6
RMS-Mag (%)	3.3	# of Points	9893
RMS-Grav (%)	13.8	# of Points	28



402
 403
 404
 405
 406

Fig. 10 – Original, modelled and residual magnetic fields of the bodies of Figueira Branca Suite: (a) Indiavaí, (b) Azteca, (c) Figueira Branca, and (d) Jauru. The black circles refer to the gravity measurements. The lines indicate the profiles used in the gravity inversion.



407

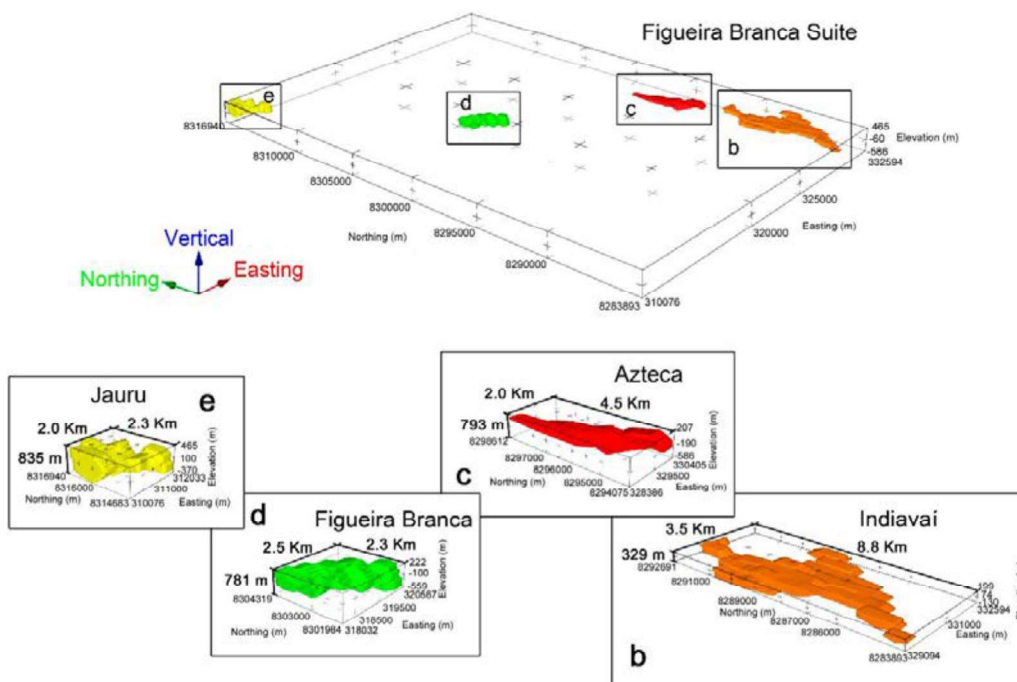
408 Fig. 11 – Original (blue lines) and modelled (red lines) of the Bouguer anomaly profiles: (a) IND-A to
 409 IND-B of the Indiavaí body, (b) AZT-A to AZT-B of the Azteca body, (c) FIG-A to FIG-B of the
 410 Figueira Branca body, and (d) JAU-A to JAU-B of the Jauru body.

411

412 The modelled bodies display an overall northwest-southeast trend, varying from 6 to 10 km
 413 in this direction, whereas their sizes in the northeast-southwest direction varied from 3 to 5

414 km (Fig. 12). The shallower horizons of the bodies were kept in the surface, constrained by
 415 the location the outcrops found in the field, and the vertical extensions ranged from
 416 approximately 330 to 835 m. The vertical extension and, by consequence, the depth of the
 417 bottom of the bodies are mostly speculative, as the ambiguity inherent to potential field
 418 methods does not allow a precise estimation of these features, even considering the
 419 knowledge about the magnetic susceptibility, remanent magnetization, and the location of
 420 outcrops.

421



422

423 Fig. 12 – Joint magnetic and gravity models of the Figueira Branca Suite. In detail, (a) Indiavaí, (b)
 424 Azteca, (c) Figueira Branca and (d) Jauru models.

425

426 The magnetization, magnetic susceptibility and density obtained in each model of the
 427 Figueira Branca Suite (Fig. 10) agree with the context of gabbroic rocks intruded in a meta-
 428 volcanosedimentary environment described by geochemical (this work) and geological
 429 observations (D'Agrella-Filho et al., 2012; Teixeira et al., 2011). All cases presented similar
 430 values for magnetic susceptibility (Table 3), leaving the cause of the difference in the
 431 amplitude of the anomalies to the remanent magnetization. The shapes and depth extents can
 432 be associated with sills, as suggested by Teixeira et al. (2011). The layers of different
 433 lithologies could not be discriminated through the geophysical methods.

434

435 5. *Conclusions*

436

437 The Figueira Branca Suite is a layered mafic-ultramafic complex, dated at 1425 Ma, intruded
438 into the Alto Jauru meta-volcanosedimentary group and adjacent to granites from the Santa
439 Helena Orogen. Using magnetic field and gamma-ray geophysical data, we delineated the
440 extent of the suite. Apart from the Indiavaí, Azteca, Figueira Branca and Jauru bodies, only
441 two mafic intrusions in the northwest of the Jauru Terrane showed magnetic and gamma-ray
442 signatures that could be related with the suite, however these two intrusions were recognized
443 as the Morro do Leme and Morro do Sem-Boné complexes, part of the 1349 Ma Cacoal
444 Suite. No other geophysical signatures similar to the four intrusions of the Figueira Branca
445 Suite were found in the Jauru Terrane.

446 Thin sections of the Figueira Branca Suite indicated a mineralogy dominated by plagioclase,
447 olivine and variable amounts of intergrown pyroxene (0 to 30%). This mineralogy indicates
448 gabbroic rocks, as it was shown in the TAS. Magnetite is likely opaque minerals phase and is
449 present in all samples. The increase in the amount of pyroxene among the samples from one
450 intrusion to another in the Figueira Branca Suite suggests a fractionation in the parental
451 magma. REE analyses normalized to chondrites showed a trend of major enrichment of
452 LREE over HREE elements. The change in the slope of the REE normalized to chondrites
453 indicates an increase in the amount of melt in the parental magma. These two changes
454 suggest that the extraction of magma generated the bodies of the Figueira Branca Suite in the
455 sequence: Indiavaí, Figueira Branca, Azteca and Jauru.

456 Magnetic and gravity fields were used to compose 3D models constrained by magnetic
457 susceptibility (average of 0.06) and density (average of 2.93 g/cm³) measurements. This data
458 combined with new field investigation and geochemical data indicate sill-like shapes
459 extending 8 km on average in the northwest direction. The calculated remanent
460 magnetizations are similar to the direction suggested by previously published paleomagnetic
461 data of the Indiavaí gabbro.

462 Trace element concentrations suggested that the parental magma of the Figueira Branca Suite
463 is associated with metasomatic processes of subduction zones. The magma was characterized
464 by hydrous melts, typical from supra-subduction environments. The northwest alignment of
465 the bodies, indicated by geological observation and geophysical modelling, is perpendicular

466 to the direction of accretion of the terranes in southwest Amazon Craton and parallel to
467 regional shear zones. The suite is located to east-northeast of the orogen and paleo-
468 subduction zone that generated the Santa Helena orogen, marked by the Piratininga and
469 Caramujo shear zones (Fig. 1).

470 Previously published isotope data show a juvenile mantle source for the Figueira Branca
471 Suite. The integration of these data with those presented in this paper indicate that the
472 magmatism that generated the Figueira Branca Suite during a phase of extension of the Jauru
473 Terrane. This event occurred during the late stages of emplacement of the Santa Helena
474 orogeny (1425 Ma) and was interpreted as a magmatism in a back-arc setting.

475

476 *6. Acknowledgements*

477

478 We would like to thank Vanessa B. Ribeiro for the comments, and the Brazilian Geological
479 Service for the data. This work was done with the support of the CNPq, National Council for
480 Technological and Scientific Development – Brazil.

481

482 *7. References*

483

484 Bettencourt, J.S., Leite Jr, W.B., Ruiz, A.S., Matos, R., Payolla, B.L., Tosdal, R.M., 2010.
485 The Rondonian-San Ignacio Province in the SW Amazonian Craton: An overview. *Journal of*
486 *South American Earth Sciences* 29, 28-46.

487 Cordani, R., Shukowsky, W., 2009. Virtual Pole from Magnetic Anomaly (VPMA): A
488 procedure to estimate the age of a rock from its magnetic anomaly only. *J Appl Geophys* 69,
489 96-102.

490 Cordani, U.G., Fraga, L.M., Reis, N., Tassinari, C.C.G., Brito-Neves, B.B., 2010. On the
491 origin and tectonic significance of the intra-plate events of Grenvillian-type age in South
492 America: A discussion. *Journal of South American Earth Sciences* 29, 143-159.

493 Corrêa da Costa, P.C., Girardi, V.A.V., Matos, J.B.d., Ruiz, A.S., 2009. Geocronologia Rb-Sr
494 e características geoquímicas dos diques máficos da região de Nova Lacerda e Conquista
495 D'Oeste (MT), porção sudoeste do Craton Amazônico [Rb-Sr geochronology and

496 geochemical characteristics of mafic Dykes in the Nova Lacerda and Conquista D'Oeste
497 region, Mato Grosso, SW Amazonian Craton]. *Geologia USP: Série Científica* 9, 17.

498 D'Agrella-Filho, M.S., Trindade, R.I.F., Elming, S.A., Teixeira, W., Yokoyama, E., Tohver,
499 E., Geraldés, M.C., Pacca, I.I.G., Barros, M.A.S., Ruiz, A.S., 2012. The 1420 Ma Indiavai
500 Mafic Intrusion (SW Amazonian Craton): Paleomagnetic results and implications for the
501 Columbia supercontinent. *Gondwana Res* 22, 956-973.

502 Dickson, B.L., Scott, K.M., 1997. Interpretation of aerial gamma-ray surveys – adding the
503 geochemical factors. *AGSO Journal of Australia Geology and Geophysics* 17, 13.

504 Fedi, M., Florio, G., Rapolla, A., 1994. A Method to Estimate the Total Magnetization
505 Direction from a Distortion Analysis of Magnetic-Anomalies. *Geophys Prospect* 42, 261-274.

506 Foss, C., 2006. Evaluation of strategies to manage remanent magnetization effects in
507 magnetic field inversion, 76th Annual SEG International Meeting. SEG, New Orleans, p. 4.

508 Geraldés, M.C., Van Schmus, W.R., Condie, K.C., Bell, S., Teixeira, W., Babinski, M., 2001.
509 Proterozoic geologic evolution of the SW part of the Amazonian Craton in Mato Grosso
510 state, Brazil. *Precambrian Res* 111, 91-128.

511 Girardi, V.A.V., da Costa, P.C.C., Teixeira, W., 2012. Petrology and Sr-Nd characteristics of
512 the Nova Lacerda dike swarm, SW Amazonian Craton: new insights regarding its
513 subcontinental mantle source and Mesoproterozoic geodynamics. *Int Geol Rev* 54, 165-182.

514 Kepezhinskas, P., McDermott, F., Defant, M.J., Hochstaedter, A., Drummond, M.S.,
515 Hawkesworth, C.J., Koloskov, A., Maury, R.C., Bellon, H., 1997. Trace element and Sr-Nd-
516 Pb isotopic constraints on a three-component model of Kamchatka arc petrogenesis. *Geochim*
517 *Cosmochim Acta* 61, 577-600.

518 Louro, V.H.A., Mantovani, M.S.M., Ribeiro, V.B., 2014. Magnetic field analysis of Morro
519 do Leme nickel deposit. *Geophysics* 79, K1-K9.

520 Matos, J.B.d., Silva, C.H.d., Costa, A.C.D.d., Ruiz, A.S., Souza, M.Z.A.d., Batata, M.E.F.,
521 Corrêa da Costa, P.C., Paz, J.D.d.S., 2009. *Geologia e Recursos Minerais da Folha Jauru*
522 (SD.21-Y-C-III), Programa Geologia do Brasil, Cuiabá, p. 134.

523 McDonough, W.F., Sun, S.S., 1995. The Composition of the Earth. *Chem Geol* 120, 223-253.

524 Menezes, R.G., 1993. Pontes e Lacerda. Folha SD. 21-Y-c-n, Programa Levantamentos
525 Geológicos Básicos do Brasil - PLGB. CPRM - Serviço Geológico do Brasil.

526 Middlemost, E.A.K., 1994. Naming Materials in the Magma Igneous Rock System. *Earth-Sci*
527 *Rev* 37, 215-224.

528 Nunes, N.S.d.V., 2000a. Geologia e resultados prospectivos da área de Figueira
529 Branca/Indiavaí, Mato Grosso, Série Metais do Grupo da Platina e Associados, 24 ed. CPRM
530 - Serviço Geológico do Brasil.

531 Nunes, N.S.d.V., 2000b. Geologia e resultados prospectivos das áreas Morro do Leme e
532 Morro Sem Boné/Mato Grosso, Série Metais do Grupo da Platina e Associados, CPRM -
533 Serviço Geológico do Brasil ed. CPRM - Serviço Geológico do Brasil, Goiânia, p. 61.

534 Quadros, N.L.E.S., Rizzotto, G.J., 2007. Geologia e recursos minerais do Estado de
535 Rondônia: Sistema de Informações Geográficas – SIG: Texto Explicativo do Mapa
536 Geológico e de Recursos Minerais do Estado de Rondônia., Programa Geologia do Brasil.
537 CPRM, Porto Velho, p. 153 p.

538 Rizzotto, G.J., Santos, J.O.S., Hartmann, L.A., Tohver, E., Pimentel, M.M., McNaughton,
539 N.J., 2013. The Mesoproterozoic Guapore suture in the SW Amazonian Craton: Geotectonic
540 implications based on field geology, zircon geochronology and Nd-Sr isotope geochemistry.
541 *Journal of South American Earth Sciences* 48, 271-295.

542 Roest, W.R., Verhoef, J., Pilkington, M., 1992. Magnetic Interpretation Using the 3-D
543 Analytic Signal. *Geophysics* 57, 116-125.

544 Ruiz, A.S., 2005. Evolução Geológica do Sudoeste do Cráton Amazônico Região Limítrofe
545 Brasil-Bolívia-Mato Grosso, Departamento de Geociências. UNESP - Rio Claro, Rio Claro,
546 p. 299.

547 Saes, G.S., Leite, J.A.S., Weska, R.K., 1984. Geologia da Folha Jauru (SD.21.Y.C.III): uma
548 síntese de conhecimentos, 33rd Congresso Brasileiro de Geologia. Sociedade Brasileira de
549 Geologia, Rio de Janeiro.

550 Shervais, J.W., 1982. Ti-V Plots and the Petrogenesis of Modern and Ophiolitic Lavas. *Earth*
551 *Planet Sc Lett* 59, 101-118.

552 Souza, M.Z.A.d., Batata, M.E.F., Ruiz, A.S., Lima, G.A.d., Matos, J.B.d., Paz, J.D.d.S.,
553 Costa, A.C.D.d., Silva, C.H.d., Corrêa da Costa, P.C., 2009. Geologia e Recursos Minerais da
554 Folha Rio Branco (SD-21-Y-D-1), Programa Geologia do Brasil, Cuiabá, p. 178.

555 Sun, S.-s., McDonough, W.F., 1989. Chemical and isotopic systematics of oceanic basalts:
556 implications for mantle composition and processes. Geological Society, London, Special
557 Publications 42, 313-345.

558 Tassinari, C.C.G., Bettencourt, J.S., Geraldés, M.C., Macambira, M.J.B., Lafon, J.M., 2000.
559 The Amazonian Craton, in: Cordani, U.G., Milani, E.J., Thomaz Filho, A., Campos, D.A.
560 (Eds.), 31st International Geological Congress. Sociedade Brasileira de Geologia, Rio de
561 Janeiro, pp. 41-95.

562 Tassinari, C.C.G., Macambira, M.J.B., 1999. Geochronological provinces of the Amazonian
563 Craton. Episodes 22, 174-182.

564 Teixeira, W., Ernst, R.E., Hamilton, M.A., Lima, G., Ruiz, A.S., Geraldés, M.C., 2016.
565 Widespread ca. 1.4 Ga intraplate magmatism and tectonics in a growing Amazonia. Gff 138,
566 241-254.

567 Teixeira, W., Geraldés, M.C., D'Agrella, M.S., Santos, J.O.S., Barros, M.A.S., Ruiz, A.S., da
568 Costa, P.C.C., 2011. Mesoproterozoic juvenile mafic-ultramafic magmatism in the SW
569 Amazonian Craton (Rio Negro-Juruena province): SHRIMP U-Pb geochronology and Nd-Sr
570 constraints of the Figueira Branca Suite. Journal of South American Earth Sciences 32, 309-
571 323.

572 Teixeira, W., Geraldés, M.C., Matos, R., Ruiz, A.S., Saes, G., Vargas-Mattos, G., 2010. A
573 review of the tectonic evolution of the Sunsas belt, SW Amazonian Craton. Journal of South
574 American Earth Sciences 29, 47-60.

575 Vermeesch, P., 2006. Tectonic discrimination diagrams revisited. Geochemistry, Geophysics,
576 Geosystems 7, n/a-n/a.

577 Wang, H., Wu, Y.B., Qin, Z.W., Zhu, L.Q., Liu, Q., Liu, X.C., Gao, S., Wijbrans, J.R., Zhou,
578 L., Gong, H.J., Yuan, H.L., 2013. Age and geochemistry of Silurian gabbroic rocks in the
579 Tongbai orogen, central China: Implications for the geodynamic evolution of the North
580 Qinling arc-back-arc system. Lithos 179, 1-15.

- 581 Zheng, Y.F., 2012. Metamorphic chemical geodynamics in continental subduction zones.
582 Chem Geol 328, 5-48.

4. Manuscript 3: Magnetic Amazon: where was the Amazon Craton in Nuna?

So far, the Figueira Branca suite was evaluated in scales from microscopic to hundreds of kilometres. In chapter 3, the Figueira Branca suite and the Jauru Terrane in the southwest of the Amazon Craton were assessed with geophysical and geochemical methodologies. This manuscript will increase the area of study once more to continental scales.

A back-arc extension in the later stages of the Santa Helena Orogen was responsible for the intrusion of the Figueira Branca Suite. From a broader perspective, during the 1.6 to 1.4 Ga period, the Amazon Craton had passed for most of its accretionary history, and would still face the accretion of its youngest provinces, the Rondonian-San Ignácio and Sunsás.

The Paleo- to Mesoproterozoic period was marked by the supercontinent Nuna. A variety of models proposed reconstructions for the supercontinent, with different constituent fragments and geometries. The Amazon Craton has been shown attached and separated from the Nuna's major landmass, and the central objective of this chapter is to investigate position of the craton from 1.6 to 1.4 Ga. To achieve it, magnetic field data was used to analyse three reconstructions of Nuna: (1) Mertanen and Pesonen (2012), which is based on paleomagnetic data; (2) Pisarevsky et al. (2014), based on paleomagnetic and geological constraints; and (3) Pehrsson et al. (2015) who integrated paleomagnetic and geological data with patterns and features of ore deposit distribution.

The dataset used to evaluate the reconstructions was the global magnetic anomaly map, EMAG2 (Maus et al., 2009). It was used to map the Amazon and other cratons suggested to be connected from 1.6 to 1.4 Ga: West African, Baltic and the North China cratons. Magnetic field regimes and lineaments were used to evaluate coeval blocks of different cratons. By recognizing the supercontinent reconstruction model that the magnetic field best supported, it

was possible to suggest the condition and location of the Amazon Craton during the intrusion of the Figueira Branca Suite.

Manuscript Details

Manuscript number	PRECAM_2017_82
Title	Magnetic Amazon: where was the Amazon Craton in Nuna?
Article type	Research Paper

Abstract

A variety of reconstructions have been proposed for the Paleo- to Mesoproterozoic supercontinent Nuna. Most involve the juxtaposition of Laurentia and Baltica with Siberia occupying an adjacent or nearby position. But the disposition of other cratonic blocks around these core elements, or whether they were even part of Nuna, is unresolved. We use magnetic field data from the global magnetic anomaly map, EMAG2, from the Amazon, Baltic, West African and North China cratons to observe potential continuity of magnetic lineaments and regimes in domains of similar ages within these cratons. On this basis, a permissible early Mesoproterozoic configuration of these cratonic fragments involves southwest Baltica (Sarmatia) abutting the northern portion of the Amazon Craton (Maroni-Itacaiúnas), whereas the western or the southern border of West Africa would be close to, or connected with, the northeast side of the Amazon Craton. This data is consistent with those models that locate the Amazon Craton at the southern end of the main Nuna landmass.

Keywords Amazon Craton; Nuna; Mesoproterozoic; Magnetic Field; EMAG2.

Corresponding Author Vinicius Louro

Order of Authors Vinicius Louro, Marta Mantovani, Peter A. Cawood, VANESSA RIBEIRO

Suggested reviewers Johanna Salminen, Sally Pehrsson, Joseph Meert, David Evans, M. Santosh

Submission Files Included in this PDF

File Name [File Type]

Louro et al - 2017 - Magnetic Amazon - Cover Letter.docx [Cover Letter]

Louro et al - 2017 - Magnetic Amazon.docx [Manuscript File]

Fig 1 - Nuna Theories.tif [Figure]

Fig 2 - Magnetic regimes.tif [Figure]

Fig 3 - Amazon Craton - Balburgh et al - 2009.tif [Figure]

Fig 4 - West Africa Craton - Youbi et al - 2013.tif [Figure]

Fig 5 - Baltica Craton - Bogdanova et al - 2007.tif [Figure]

Fig 6 - North China Craton - Wu et al - 2013.tif [Figure]

Fig 7 - Amazon Craton - Mag.tif [Figure]

Fig 8 - West African Craton - Mag.tif [Figure]

Fig 9 - Baltica Craton - Mag.tif [Figure]

Fig 10 - North China Craton - Mag.tif [Figure]

Fig 11 - Nuna - Mertanen and Pesonen - 2012.tif [Figure]

Fig 12 - Mertanen and Pesonen - Terranes.tif [Figure]

Fig 13 - Columbia - Pisarevsky - 2014.tif [Figure]

Fig 14 - Pisarevsky - Terranes.tif [Figure]

Fig 15 - Columbia - Pehrsson - 2014.tif [Figure]

Fig 16 - Pehrsson - Terranes.tif [Figure]

Louro et al - 2017 - Magnetic Amazon - Table 1.docx [Table]

Highlights.docx [Highlights]

To view all the submission files, including those not included in the PDF, click on the manuscript title on your EVISE Homepage, then click 'Download zip file'.

1 **Magnetic Amazon: where was the Amazon Craton in Nuna?**

2

3 **Vinicius H. A. Louro^{1,2}, Peter A. Cawood^{2,3}, Marta S. M. Mantovani¹, Vanessa B.**
4 **Ribeiro^{1,4}**

5

6 ¹ Instituto de Astronomia, Geofísica e Ciências Atmosféricas, Universidade de São Paulo, São
7 Paulo, Brazil.

8 ² Department of Earth and Environmental Sciences, University of St. Andrews, St. Andrews,
9 UK.

10 ³ School of Earth, Atmosphere & Environment, Monash University, Melbourne, VIC 3800,
11 Australia

12 ⁴ Universidade Federal de Pernambuco – UFPE, Recife, Pernambuco, Brazil.

13

14 E-mails: vilouro@usp.br, peter.cawood@monash.edu, msmmanto@usp.br,
15 van.biondo@gmail.com

16

17 **Corresponding author:** Vinicius H. A. Louro.

18 **E-mail:** vilouro@usp.br

19 **Present Address:** Rua do Matão, 1226, Sala A-204, Laboratório de Geofísica da Litosfera –
20 GEOLIT, Instituto de Astronomia, Geofísica e Ciências Atmosféricas, Universidade de São
21 Paulo, Cidade Universitária, São Paulo, Brazil. CEP: 05508-090

22

23 Phone: +55 (11) 99985 1501

24 Date of Submission: 05 February 2017

25

26

27 **Abstract**

28

29 A variety of reconstructions have been proposed for the Paleo- to Mesoproterozoic
30 supercontinent Nuna. Most involve the juxtaposition of Laurentia and Baltica with Siberia
31 occupying an adjacent or nearby position. But the disposition of other cratonic blocks around
32 these core elements, or whether they were even part of Nuna, is unresolved. We use magnetic
33 field data from the global magnetic anomaly map, EMAG2, from the Amazon, Baltic, West
34 African and North China cratons to observe potential continuity of magnetic lineaments and
35 regimes in domains of similar ages within these cratons. On this basis, a permissible early
36 Mesoproterozoic configuration of these cratonic fragments involves southwest Baltica
37 (Sarmatia) abutting the northern portion of the Amazon Craton (Maroni-Itacaiúnas), whereas
38 the western or the southern border of West Africa would be close to, or connected with, the
39 northeast side of the Amazon Craton. This data is consistent with those models that locate the
40 Amazon Craton at the southern end of the main Nuna landmass.

41

42 **Keywords**

43 Amazon Craton, Nuna, Mesoproterozoic, Magnetic Field, EMAG2.

44

45

46

47

48

49

50

51

52

53

54

55 **1. Introduction**

56

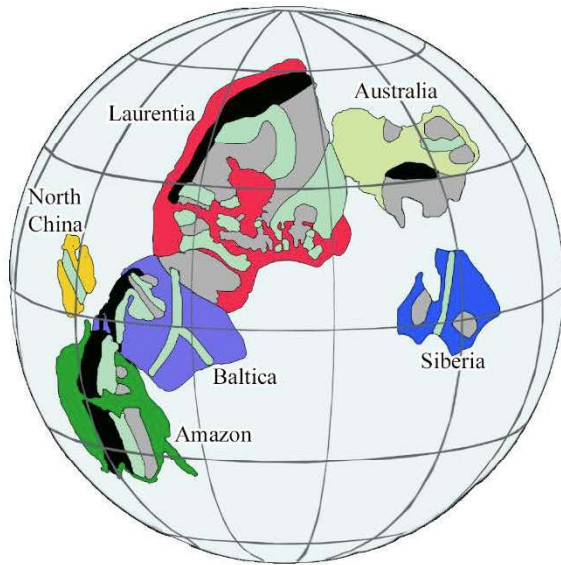
57 The location and composition of the Paleo- to Mesoproterozoic supercontinent Nuna, also
58 known as Columbia and Hudsonland, and its constituent fragments is much debated and a
59 variety of models, some of which entail mutually exclusive configurations, have been proposed
60 (Evans and Mitchell, 2011; Johansson, 2009; Pisarevsky et al., 2014; Rogers and Santosh,
61 2002; Williams et al., 1991; Zhao et al., 2002; Zhao et al., 2004; Zhao et al., 2001).
62 Understanding the processes of supercontinent amalgamation and breakup, as well as their
63 paleogeographic configuration, provides valuable insights into the evolution of the Earth,
64 including the role of Large Igneous Provinces (LIP) (Youbi et al., 2013), their relationship to
65 patterns of ore deposits (Cawood and Hawkesworth, 2015; Pehrsson et al., 2015), and their
66 potential impact on the Earth's surficial environments, including atmosphere and ocean
67 composition and the biosphere (e.g., Cawood and Hawkesworth, 2015, and references therein).

68 Historically, supercontinent reconstructions are based on the integration of one or more datasets
69 involving stratigraphic and tectonic correlations, geochemical and isotopic compositions, and
70 paleomagnetic data. In this paper, we evaluate the position of the Amazon Craton in the Nuna
71 supercontinent using magnetic field data and, in particular, we assess a number of recent
72 reconstructions that highlight the range of Nuna configurations and the datasets used to justify
73 those configurations, including: (1) Mertanen and Pesonen (2012), which is based on
74 paleomagnetic data; (2) Pisarevsky et al. (2014), based on paleomagnetic and geological
75 constraints; and (3) Pehrsson et al. (2015) who integrated paleomagnetic and geological data
76 with patterns and features of ore deposit distribution (Fig. 1).

77

Nuna Reconstructions

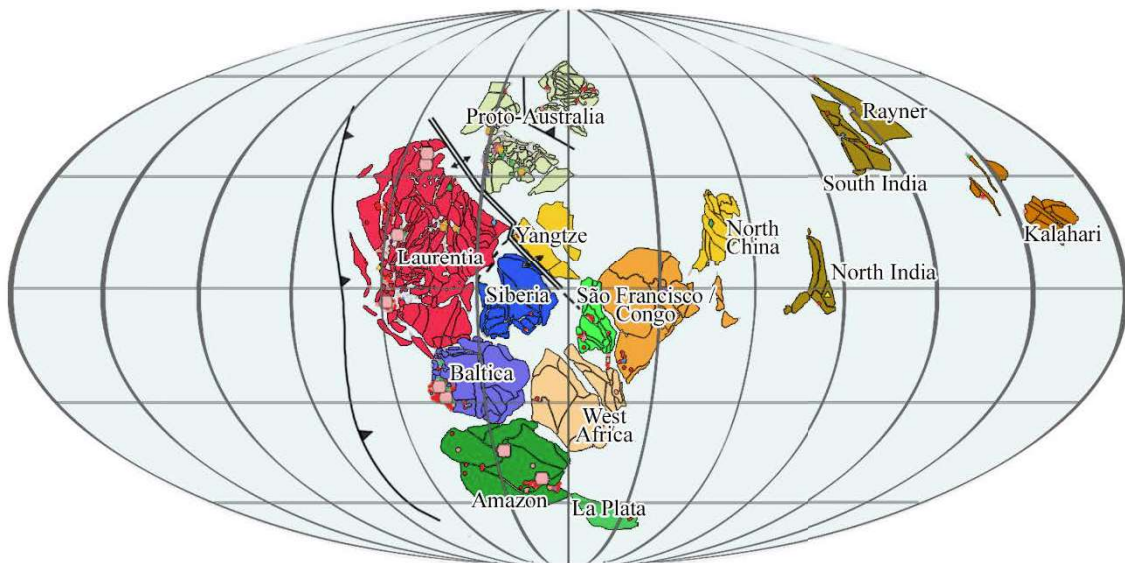
(a) Mertanen and Pesonen (2012)



(b) Pisarevsky et al. (2014)



(c) Pehrsson et al. (2015)



78

79 Fig. 1 – Reconstructions of Nuna proposed by (a) Mertanen and Pesonen (2012), (b)

80

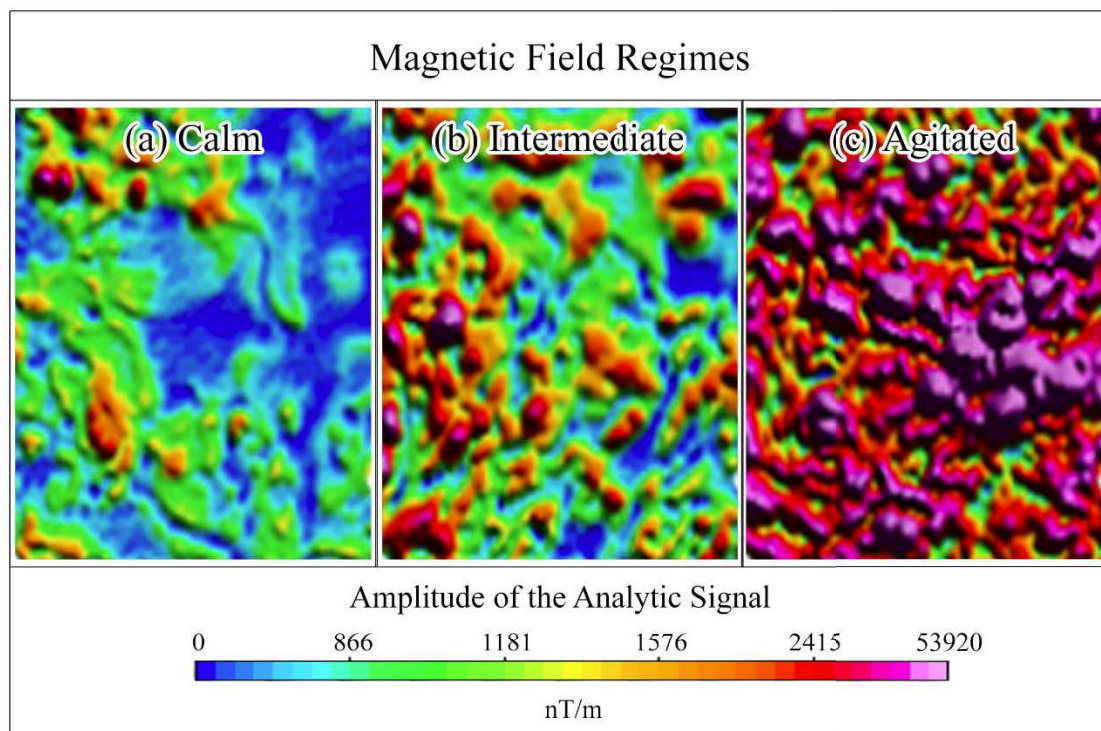
Pisarevsky et al. (2014), and (c) Pehrsson et al. (2015).

81

82 Our assessment is based on a combination of Total Magnetic Field, the Amplitude of the
83 Analytic Signal 3D (Roest et al., 1992), and Tilt data (Verduzco et al., 2004) of the Amazon
84 and potential adjacent cratons, to compare magnetic signature, which along with geologic and
85 age data of these cratons enables us to reevaluate proposed Nuna reconstructions. Unfortunately,

86 paleopole data for the Amazon Craton for the relevant period of Nuna assembly is limited: the
87 1420 Ma Indiavaí (D'Agrella-Filho et al., 2012) and Nova Guarita intrusives (Bispo-Santos et
88 al., 2012), and the 1790 Ma Colider (Bispo-Santos et al., 2008) and Avanavero intrusives (Reis
89 et al., 2013). The small number of Proterozoic reference poles in the Amazon Craton, as well
90 as West Africa (Pisarevsky et al., 2014), in part reflects the vast area of the Amazon forest
91 with limited access and poor exposure, as well as areas of civilian unrest, or of military and
92 strategic value, and thus complicates the reconstruction of the Amazon Craton in Nuna. In this
93 paper, we demonstrate that remotely accessed data, such as magnetic field data, can provide
94 additional information to constrain the relationship between blocks in Nuna. In particular, we
95 use magnetic field data and its products to evaluate field regimes and magnetic lineaments
96 within and between cratons. Magnetic field regimes are defined by the concentration of
97 magnetic anomalies within a designated region. The regimes can be interpreted as calm,
98 intermediate or agitated depending on the frequency pattern of the magnetic anomalies (Fig.
99 2). Magnetic lineaments are normally expressions of contacts, faults, boundaries between
100 terranes, and folds, where secondary magnetite is created through the insertion of oxygen in a
101 Fe-bearing environment (Grant, 1985b; Rotherham, 1997).

102



103

104 Fig. 2 – Magnetic field regimes using the Amplitude of the Analytic Signal: (a) calm, (b)
105 intermediate, and (c) agitated.

106 **2. Geology of the Cratons**

107

108 The evaluation of the role of Amazonia in Nuna, or indeed whether it was even part of Nuna,
109 requires an outline of available geological constrains. Our focus is the Amazon Craton and
110 most published models suggest that it is linked with one or more of West African, Baltic and/or
111 the North China cratons. Outlined below are the key geological features of these blocks.

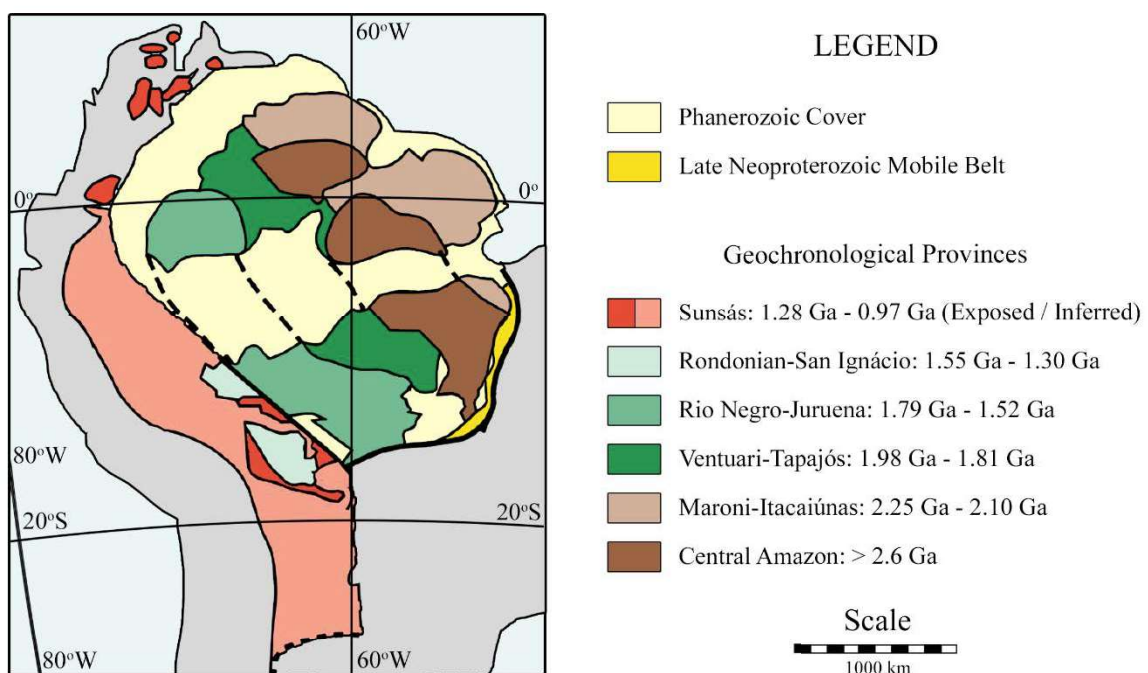
112

113 **2.1. Amazon Craton**

114

115 Tassinari and Macambira (1999) and Teixeira et al. (2010) divide the Amazon craton into six
116 structural and geochronological provinces: Central Amazon (> 2.6 Ga), Maroni-Itacaiúnas
117 (2.25 to 2.10 Ga), Ventuari-Tapajós (1.98 to 1.81 Ga), Rio Negro-Juruena (1.79 to 1.52 Ga),
118 Rondonian-San Ignácio (1.55 to 1.30 Ga) and Sunsás (1.28 to 0.97 Ga) (Fig. 3). The stable
119 Archean nuclei of the Central Amazon is a granite-greenstone terrain. It was not affected by
120 the 2.2 Ga to 1.9 Ga Trans-Amazonian Orogeny (Hurley et al., 1967), however
121 Paleoproterozoic magmatic and sedimentary events are recorded across this cratonic core.

122



123

124 Fig. 3 – Geochronological provinces of the Amazon Craton (Bahlburg et al., 2009).

125 The Paleoproterozoic Maroni-Itacaiúnas Province is located to the northeast of the Central
126 Amazon and can be traced for 1500 km (Fig. 3). It is characterized by greenstone belts and
127 associated calc-alkaline granitoids, with large metavolcanic-sedimentary sequences
128 metamorphosed from greenschist to amphibolite facies (Tassinari and Macambira, 1999). To
129 the southwest of the Central Amazon, lies the northwest-southeast elongated Ventuari-Tapajós
130 province, composed of calc-alkaline granitoids with juvenile isotopic signatures (Cordani et
131 al., 2010). Further to the southwest, the Rio Negro-Juruena province of granite gneisses and
132 granitoids of granodioritic and tonalitic compositions forms a 2000 km long and 600 km wide
133 belt aligned northwest-southeast (Fig. 3).

134 The Rondonian-San Ignácio and Sunsás are the largest provinces of the Amazon Craton (Fig.
135 3). The 1.55 to 1.30 Ga Rondonian-San Ignácio has granite-gneiss-migmatitic terranes
136 metamorphosed to amphibolite or granulite facies composing its basement (Tassinari and
137 Macambira, 1999). Cordani and Teixeira (2007) associate the formation of the Rondonian-San
138 Ignácio province to the amalgamation of intra-oceanic magmatic arcs and accretionary prisms
139 and ultimately their collision to the southwest with the Rio Negro-Juruena province. The
140 Sunsás orogenic belt is the youngest province of the Amazon Craton. It is the expression of the
141 collision between Amazonia and Laurentia, during the assembly of the Rodinia (Cawood and
142 Pisarevsky, 2017; Sadowski and Bettencourt, 1996; Tohver et al., 2006). The Sunsás province
143 is characterized by metamorphosed volcano-plutonic-sedimentary sequences intruded by
144 Neoproterozoic granitic suites (Boger et al., 2005).

145

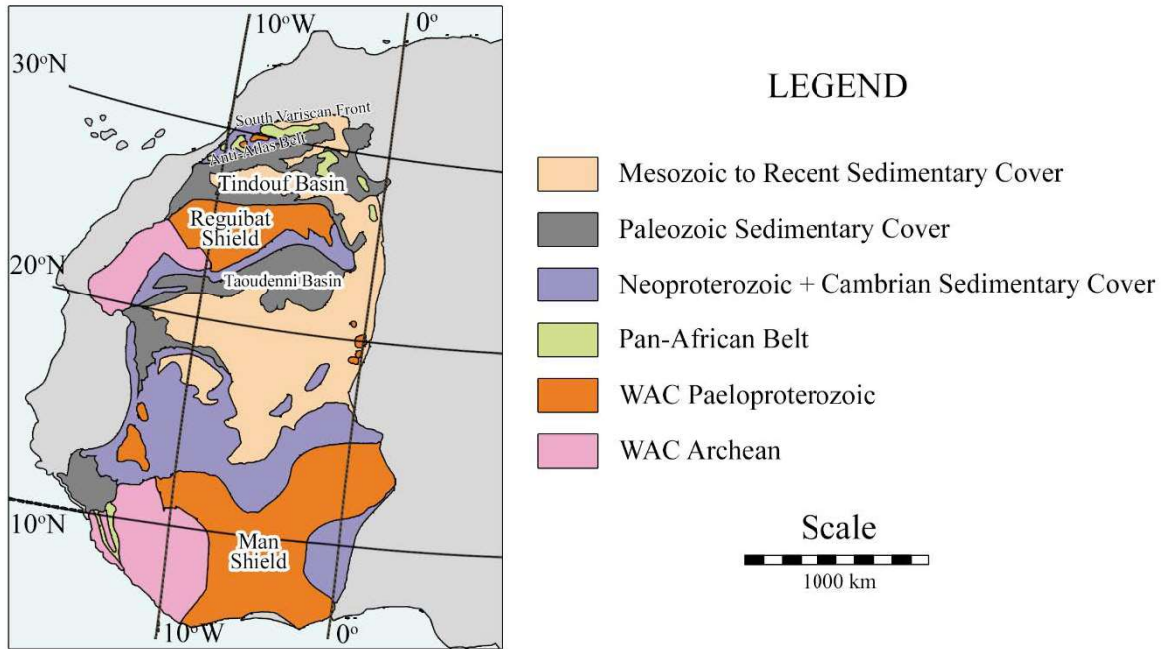
146 **2.2. West African Craton**

147

148 The West African Craton, northwest Africa (Fig. 4), has been stable since 2 Ga (Youbi et al.,
149 2013). It consists of the Archean Reguibat and Man shields to the north and south, respectively,
150 large Paleoproterozoic domains separated by cratonic sedimentary basins, and at the northern
151 end, the Anti Atlas belt. The Man shield is composed by TTG-type banded gneiss, older than
152 3.0 Ga (Beckinsale et al., 1980), overlain by greenstone belt lithologies intruded by granites.
153 The Reguibat Shield contain Archean and Paleoproterozoic migmatites interlayered with mafic
154 gneisses, greenstone belts, and voluminous tonalitic or granodioritic plutons (Key et al., 2008).
155 Between the shields, in the central portion of the West African Craton, the late Proterozoic to

156 Paleozoic Taoudeni basin, and to the north of the Reguibat Shield, the Paleozoic Tindouf basin,
157 overlie basement (Guerrak, 1989; Windley, 1987).

158



159

160 Fig. 4 – West African Craton (WAC) (Ennih and Liégeois, 2008).

161

162 The Anti-Atlas belt is located between the Alpine Atlas chain and the Tindouf basin. It is
163 composed of Proterozoic low- to medium-grade schists and intrusive granitoids, and a thick
164 (ca. 10 km) late Neoproterozoic to Paleozoic sedimentary cover (Soulimani and Burkhard,
165 2008). Many orogenic cycles are recognized in the West African Craton, spanning from 3.5 to
166 1.75 Ga, along with the 750 to 550 Ma Pan African orogenic event (Ennih and Liégeois, 2008).
167 Söderlund et al. (2013), El Bahat et al. (2013), Kouyaté et al. (2013) and Youbi et al. (2013)
168 indicate that the interval from 1.7 to 1.0 Ga was marked by intraplate magmatic events.

169

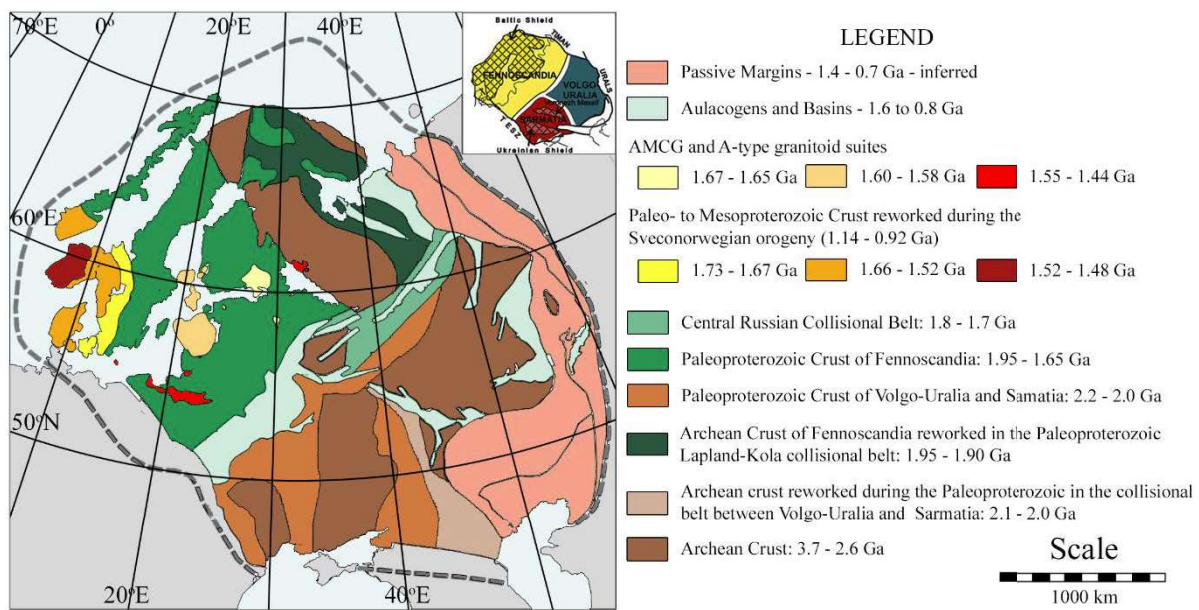
170 2.3. Baltic Craton

171

172 Baltica is divisible into the Archean proto-continents of Sarmatia, Volgo-Uralia and
173 Fennoscandia (Fig. 5) that were assembled into Baltica along Paleoproterozoic to
174 Mesoproterozoic orogenic belts (Bogdanova et al., 2008).

175 The Fennoscandian Shield, northwest Baltica, is surrounded by Paleoproterozoic crust formed
 176 between 1.95 and 1.90 Ga, and intruded by the 1850-1650 Ma Transcandinavian Igneous Belt
 177 (Bingen et al., 2008). Basement within the shield is cut by Anorthosite-Mangerite-Charnockite-
 178 Granite (AMCG) (Emslie et al., 1994) and A-type granitoid suites, dolerite dykes and sills,
 179 tholeiitic basalt, mafic metavolcanic rocks, and gabbro-tonalite complexes were emplaced
 180 between 1.73 to 1.44 Ga (Bogdanova et al., 2006; Bogdanova et al., 2008). The Central Russian
 181 collisional belt connects Fennoscandia and Sarmatia (Fig. 5). It contains blocks of Archean
 182 rocks reworked during the Paleoproterozoic.

183



184

185 Fig. 5 – Baltic Craton (Bogdanova et al., 2008).

186

187 The Volgo-Uralia Shield in eastern Baltica, contains granitic gneiss as old as 3.3 Ga
 188 (Bogdanova et al., 2005) and is characterized by 3.0 to 2.7 Ga belts of metasedimentary and
 189 metaigneous granulites, and subordinate komatiite-bearing greenstone sequences (Bogdanova
 190 et al., 2008). The collisional belt between the Volgo-Uralia and Sarmatia contains turbiditic
 191 pelites and greywackes with carbonaceous rocks (Shchipansky et al., 2007). To the north and
 192 east of the Volgo-Uralia, lies an inferred 1.4 to 0.7 Ga passive margin succession (Bogdanova
 193 et al., 2008).

194 Sarmatia is the result of the amalgamation of 3.7 to 2.6 Ga blocks intercalated by 2.2 to 2.1 Ga
 195 Paleoproterozoic belts (Bogdanova et al., 2008). Bogdanova et al. (2006) report north-south

196 trends, both in the Paleoproterozoic belts and reworked Archean crust, but with an abrupt
197 change to a northeast-southwest orientation at the northeastern limit of the block. This change
198 marks the continental-margin igneous belt formed at 2.0 to 1.95 Ga with the collision of
199 Sarmatia with the Volgo-Uralia.

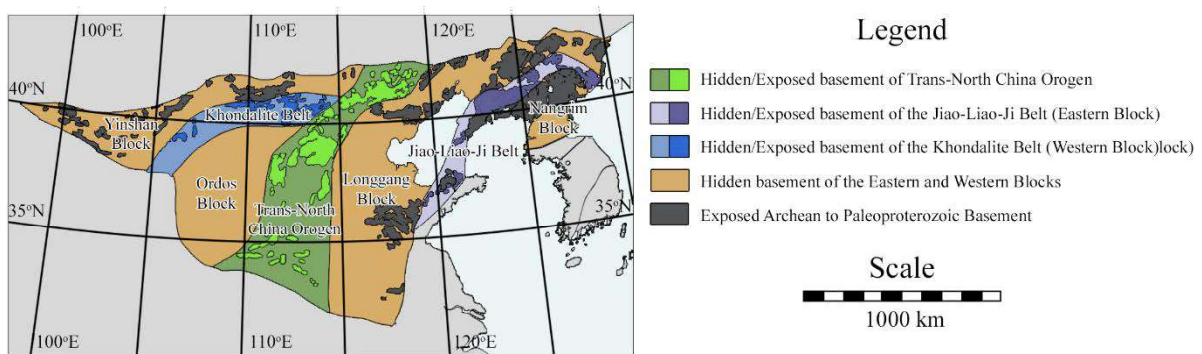
200

201 2.4. North China Craton

202

203 The North China Craton consists of four Archean blocks (Yinshan, Ordos, Longgang and
204 Nangrim), amalgamated by younger orogenic belts (Fig. 6) (Zhao and Cawood, 2012). The
205 Yinshan and the Ordos blocks are separated by the 1.95 to 1.92 Ga Khondalite Belt, which
206 together form the Western Block of the North China Craton (Dong et al., 2007; Wu et al., 2013;
207 Zhao and Cawood, 2012). The Longgang and the Nangrim blocks, united by the Jiao-Liao-Ji
208 belt at 1.90 Ga, constitute the Eastern Block of the North China Craton (Wu et al., 2013; Zhao
209 and Cawood, 2012). The Western and Eastern blocks collided at ca. 1.85 Ga, forming the
210 Paleoproterozoic Trans-North China Orogen (Zhao et al., 2012).

211



212

213 Fig. 6 – North China Craton (Zhao et al., 2004).

214

215 The Yinshan Block is composed of Neoproterozoic tonalite-trondhjemite-granodiorite (TTG)
216 gneisses and minor supracrustal rocks metamorphosed at ca. 2.5 Ga (Wu et al., 2013). The 1.95
217 to 1.92 Ga Khondalite Belt, separating the Yinshan and the Ordos blocks is dominated by
218 gneisses, paragneisses, calc-silicate rocks and marbles (Zhao and Zhai, 2013). The Ordos
219 Block, to the south of the Khondalite Belt, is largely covered by the Mesozoic to Cenozoic
220 Ordos basin.

221 In the Eastern Block, the Longgang and the Nangrim blocks consist of 3.8 to 3.0 Ga TTG
222 gneisses, 2.7-2.5 Ga syntectonic granitoids, supracrustal ultramafic (komatiitic) to felsic
223 volcanic rocks and metasedimentary rocks (Zhao et al., 2001). The Jiao-Liao-Ji Belt, separating
224 the Longgang and Nangrim blocks, is characterized by metamorphosed sedimentary-volcanic
225 successions and associated granitic and mafic intrusions (Zhao and Zhai, 2013).

226 The Trans-North China Orogen extends north-south for approximately 1200 km and is up to
227 300 km wide (Zhao et al., 2012). It contains late Neoproterozoic to early Paleoproterozoic (2560
228 to 2475 Ma) TTG gneisses, granitoids and greenstone belts developed under continental
229 magmatic arc, island arc- or back-arc basin environments (Wilde et al., 2005; Zhao et al., 2012;
230 Zhao and Zhai, 2013).

231

232 **3. Methodology**

233

234 *3.1. Data*

235

236 The magnetic field data used here was obtained through the Earth Magnetic Anomaly Grid
237 (EMAG2) (Maus et al., 2009). This compiled and corrected data set incorporates satellite, ship
238 and airborne surveys, of which the last two had been given preference where available. The
239 resolution of the grid is 2 arc min (ca. 3.7 km in the equator), and the altitude normalized to 4
240 km above the geoid. Wavelengths longer than 330 km were obtained with the latest CHAMP
241 satellite magnetic field model MF6 (<http://geomag.org/models/MF6.html>, accessed
242 28/02/2017).

243

244 *3.2. Magnetic Field Techniques*

245

246 We analysed the crustal magnetic field data obtained by EMAG2 to evaluate Nuna
247 reconstructions. Three features of the magnetic field were considered to facilitate comparison
248 of continental-scale structures: the magnetic regime (agitated, intermediate, or calm, e.g. Fig.
249 2), the size of the anomalies, and the orientation of the magnetic lineaments. The resolution

250 and normalized altitude obtained from the EMAG2 are compatible with the scale of the
251 investigated tectonic features (> 3.7 km).

252 Geological and tectonic features usually present different amounts of magnetic minerals,
253 resulting in the generation of a magnetic signal, whether inserted in an external (geomagnetic)
254 field or not. Magnetite is a minor accessory mineral present in most rocks, rarely constituting
255 more than 1 % by volume of a rock (Grant, 1985a). The formation of magnetite, primary or
256 secondary, is mainly associated with the supply of oxygen in the system. The most important
257 factors that determine the bulk magnetic properties of a rock are the total iron content, the
258 oxidation state, the initial crystallization environment, the degree of metamorphism, the degree
259 of silica saturation, the grain size of original sediment (in metasedimentary rocks), and the
260 major element chemistry (Grant, 1985a).

261 The magnetic regimes were evaluated based on the frequency that magnetic anomalies appear
262 in each domain of the cratons. An agitated regime (Fig. 2) is interpreted to represent greater
263 tectonic activity through the entire history of the block, but not necessarily in a single period,
264 while intermediate and calm regimes indicate less active settings, e.g., passive margins
265 undergoing thermally driven subsidence (Olesen et al., 2007). To observe the magnetic
266 regimes, the Total Magnetic Field (TMI) and the Amplitude of the Analytic Signal 3D (AAS)
267 (Roest et al., 1992) were analysed. The TMI shows overall patterns of anomalies, but depends
268 on the geomagnetic (inducing) field at the time of the survey. This dependence is relevant in
269 studies of large areas, in which the magnetic field changes in orientation and intensity, i.e. the
270 present magnetic field in the Amazon Craton varies in inclination from -30° to +30°,
271 declination from -20° to -10°, and intensity from 33012 to 22890 nT, depending on the location,
272 whereas in Baltica, it changes from +68° to +78° in inclination, from -2° to +10° in declination,
273 and from 52952 to 54635 nT in intensity (<https://www.ngdc.noaa.gov/geomag-web/#igrfwmm>,
274 accessed in 28/02/2017, the magnetic field refers to the International Geomagnetic Reference
275 Field model for same date the data was accessed in the website).

276 The AAS is given by the expression (Roest et al., 1992):

$$277 \quad \text{AAS} = \sqrt{[(\partial T/\partial x)^2 + (\partial T/\partial y)^2 + (\partial T/\partial z)^2]} \quad (1)$$

278 where T refers to the TMI, and x, y, and z directions in Cartesian space. The AAS is one of the
279 most commonly used techniques to evaluate the lateral limits of sources of potential field
280 anomalies.

281 Linked to the magnetic regime, the size of the anomalies was explored with the AAS (Figs. 7b,
282 8b, 9b and 10b). This technique, based on directional derivatives of the field, reveals the lateral
283 limits of discrete bodies and geological features. It displays little dependence on the direction
284 of the magnetic field, so the location of the anomaly or the presence of remanent magnetization
285 does not interfere with the results. Coeval domains connected at some point in Earth evolution
286 tend to present structures of similar sizes (Olesen et al., 2007) if no posterior event altered
287 significantly its composition and size. Regional tectonothermal events involving magmatism,
288 deformation and metamorphism can generate strain and thermal energy sufficient to alter the
289 size of the anomalies, whether by distorting the body, by changing and or extinguishing the
290 remanent magnetization, or by opening the system to oxygenated fluids and formation of
291 secondary magnetite. These changes can be observed in large areas that not necessarily are
292 limited to one specific domain.

293 The assembly of terranes and regional movements inside the cratons are considered by
294 evaluating the size of the anomalies. These events can alter the direction of magnetic
295 lineaments, especially close to the boundary zone, and less significantly in distal regions from
296 the event. The magnetic lineaments were assessed primarily with the Tilt technique (Verduzco
297 et al., 2004), and complemented by AAS. The Tilt technique is given by the relation:

$$298 \quad \text{TILT} = \tan^{-1} \left\{ \frac{\sqrt{(\partial T / \partial z)^2}}{\sqrt{[(\partial T / \partial x)^2 + (\partial T / \partial y)^2]}} \right\} \quad (2)$$

299 where T refers to the TMI, and x, y, and z directions in Cartesian space.

300 In successful supercontinent reconstructions, coeval stable domains in adjacent cratons, created
301 under similar circumstances, should display parallel to subparallel lineaments, and continuity
302 from one craton to another. Magnetic overprinting can occur after the stabilization of the
303 domain, commonly in cratonization events; for example, a regional thermal overprint occurred
304 in the southwest Amazon Craton at ca. 1.3 Ga (Bettencourt et al., 2010). This kind of event is
305 accompanied by tectonic reactivation, deformation, and magmatism, which are manifested by
306 extensive shear zones, mylonitic belts, rifts and sedimentary basins, and post-tectonic and
307 anorogenic intrusions (Cordani and Teixeira, 2007). The magnetic overprint can change the
308 orientation of the magnetic lineaments to directions that differ from those obtained during the
309 formation of the domain. Such later tectonic events are generally associated with a regional
310 thermal anomaly of sufficient magnitude to unblock the magnetic moments, which vary
311 depending on the mineral and size of the grains. These are large-scale events and were mostly
312 recognized in the cratons used in this work, and are incorporated into our interpretation.

313

314 **4. Magnetic Signatures**

315

316 To aid the visualization and interpretation of tectonic provinces and lineaments, the colours of
 317 the provinces were normalized to the colours used in the Amazon Craton map according with
 318 their respective ages (Fig. 3). The age relations and magnetic regimes are summarized in Table
 319 1.

320

321 Table 1 - The age relations and magnetic regimes of the Amazon, Baltic, West African and
 322 North China Cratons.

Craton	Terrane	Normalization (AC)	Magnetic Regime
Amazon	Central Amazon	n/a	Agitated, decreasing to the south
Amazon	Maroni-Itacaiúnas	n/a	Agitated
Amazon	Ventuari-Tapajós	n/a	Intermediate
Amazon	Rio Negro-Juruena	n/a	Intermediate, increasing to the south
Amazon	Rondonian-San Ignácio	n/a	Calm to Intermediate
Amazon	Sunsás	n/a	Calm, agitation in the central area
Amazon	Phanerozoic Cover	n/a	Calm to Intermediate
Baltica	Archean Crust	Central Amazon	Intermediate to agitated
Baltica	Archean Crust reworked - Volgo-Uralia/Sarmatia Collision	Maroni-Itacaiúnas	Calm to agitated
Baltica	Paleoproterozoic Crust of Volgo-Sarmatia	Maroni-Itacaiúnas	Intermediate to agitated
Baltica	Archean Crust reworked of Fennoscandia	Ventuari-Tapajós	Calm
Baltica	Paleoproterozoic Crust of Fennoscandia	Rio Negro-Juruena	Intermediate to agitated
Baltica	Central Russian collisional belt	Rio Negro-Juruena	Calm to intermediate
Baltica	1.73 - 1.67 Ga crust reworked during the Sveconorwegian orogeny (1.14 - 0.92 Ga)	Rio Negro-Juruena	Calm
Baltica	1.66 - 1.52 Ga crust reworked during the Sveconorwegian orogeny (1.14 - 0.92 Ga)	Rio Negro-Juruena	Calm to intermediate
Baltica	1.67 - 1.65 Ga AMCG and A-type granitoid suites	Rio Negro-Juruena	Intermediate
Baltica	1.60 - 1.58 Ga AMCG and A-type granitoid suites	Rio Negro-Juruena	Agitated
Baltica	1.52 - 1.48 Ga crust reworked during the Sveconorwegian orogeny (1.14 - 0.92 Ga)	Rondonian-San Ignácio	Calm to intermediate
Baltica	1.55 - 1.44 Ga AMCG and A-type granitoid suites	Rondonian-San Ignácio	Agitated
Baltica	Aulacogens and basins, internal parts of passive margins	Rondonian-San Ignácio	Intermediate to agitated

Baltica	Passive Margins (inferred)	Sunsás	Calm and agitated
West Africa	Archean	Central Amazon	Agitated
West Africa	Paleoproterozoic	Maroni-Itacaiúnas	Calm to agitated
West Africa	Neoproterozoic + Cambrian Sedimentary Cover	Sunsás	Intermediate to agitated
West Africa	Pan-African Belts	Phanerozoic Cover	Intermediate
West Africa	Paleozoic Sedimentary Cover	Phanerozoic Cover	Intermediate
West Africa	Mesozoic to Recent Sedimentary Cover	Phanerozoic Cover	Intermediate to agitated
North China	Archean to Paleoproterozoic basement	Central Amazon	Intermediate
North China	Trans-North China Orogen	Ventuari-Tapajós	Intermediate
North China	Khondalite Belt	Maroni-Itacaiúnas	Calm and agitated
North China	Jiao-Liao Ji Belt	Maroni-Itacaiúnas	Calm to intermediate

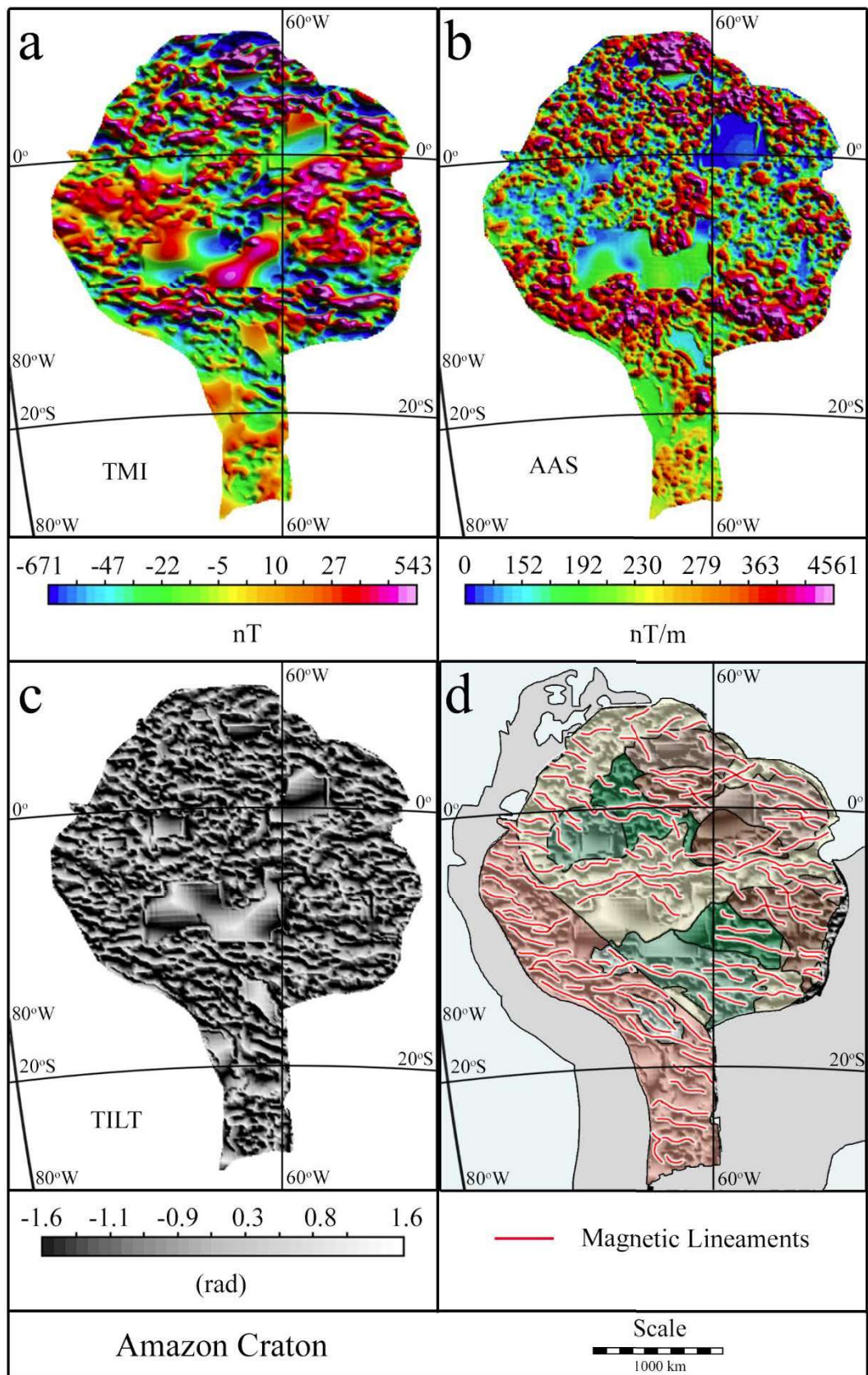
323

324 *4.1. Amazon Craton*

325

326 The Amazon Craton has a northwest-southeast trend of lithotectonic assemblages (e.g. Fig. 3)
327 that is mimicked by the magnetic field (Fig. 7). The limits of the various provinces recognized
328 within the craton are not clear from the magnetic data set alone, but with the support of
329 geological data, it was possible to associate specific magnetic signatures for each province. The
330 Central Amazon province shows an agitated magnetic domain in the north, with large
331 anomalies up to 100 km wide, and decreasing agitation and anomaly size to the south. The
332 Maroni-Itacaiúnas province has an agitated magnetic domain, with anomalies up to 130 km
333 wide. The Ventuari-Tapajós, Rio Negro-Juruena, Rondonian-San Ignácio, and Sunsás
334 provinces show a progressive decrease in agitation and anomaly size. Further to the southwest,
335 in the Amazon basin, the magnetic signature shows a significant decrease of agitation in all
336 provinces. The areas proximal to the borders of the Amazon basin show a new increase of
337 agitation, but still maintaining the overall trend of a reduction in the size of the anomaly.

338



339

340 Fig. 7 – Amazon Craton: (a) TMI, (b) AAS, (c) Tilt, and (d) Tilt map overlain by the
 341 geological provinces and magnetic lineaments. The colours of the provinces were normalized
 342 to the colours used in the Amazon Craton map (Fig. 4) according with their respective ages.

343 The magnetic lineaments from the Amazon Craton show the overall northwest-southeast trend
344 displayed by the lithotectonic provinces (Fig. 7d). This trend is orthogonal to the northeast-
345 southwest-oriented accretion that occurred around the Central Amazon province since the
346 Paleoproterozoic. The area occupied by the Amazon Basin, central in the map and covered by
347 Phanerozoic cover, shows a significant decrease in the magnetic regime and in the volume of
348 lineaments. A major lineament crosscuts the craton from east to west, starting in the eastern
349 end of the Amazon basin and continuing through the Sunsás Belt to the western border.

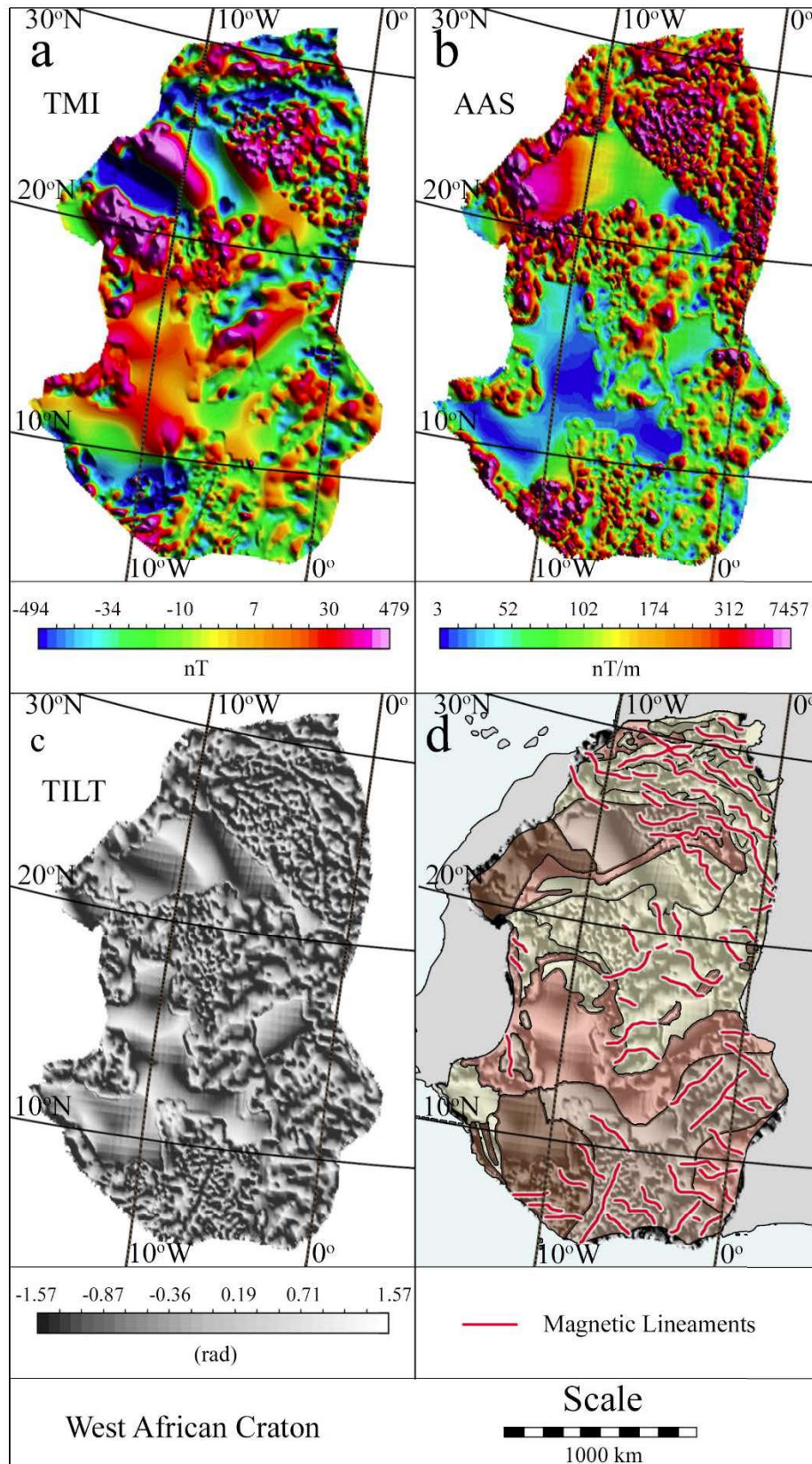
350

351 *4.2. West African Craton*

352

353 The Archean shield regions of the West African Craton, are equivalent in age to the Central
354 Amazon province, and display an overall agitated regime (Fig. 8). The shields, however,
355 display large areas that lack data. The Paleoproterozoic domains display a calm regime in the
356 south, but agitated in the northern region proximal to the Anti-Atlas belt. In the areas dominated
357 by Neoproterozoic and Cambrian sedimentary cover, the magnetic field has intermediate
358 agitation in the southeast of the West African Craton, but an agitated character in the northeast,
359 proximal to the southern front of Variscan deformation. Like the Archean shields, the
360 Neoproterozoic and Cambrian cover incorporate large areas that lack data.

361



362

363 Fig. 8 – West African Craton: (a) TMI, (b) AAS, (c) Tilt, and (d) Tilt map overlain by the
 364 geological provinces and magnetic lineaments. The colours of the provinces were normalized
 365 to the colours used in the Amazon Craton map (Fig. 4) according with their respective ages.

366 The relatively small area representing the Pan-African belts within the West African Craton is
367 dominated by a small number of large anomalies up to 100 km wide. The Paleozoic to Recent
368 sedimentary cover, extending over most of the craton, shows intermediate agitation in the
369 magnetic regime. This cover displays a local increase in agitation when proximal to the
370 Southern Front of the Variscan deformation, in the northeast of the craton. Large areas without
371 data compose the sedimentary cover.

372 The north portion of West African Craton has a northwest-southeast trend, parallel to the Anti-
373 Atlas belt and the south Variscan front (Fig. 8d). Orthogonal, northeast-southwest-oriented,
374 lineaments can be seen in the Man Shield in the south of the craton and in the area covered by
375 Mesozoic to recent sediments in the centre of the craton. Significantly large areas in the
376 southwest and northwest West African Craton do not have available magnetic field data,
377 impeding further analysis.

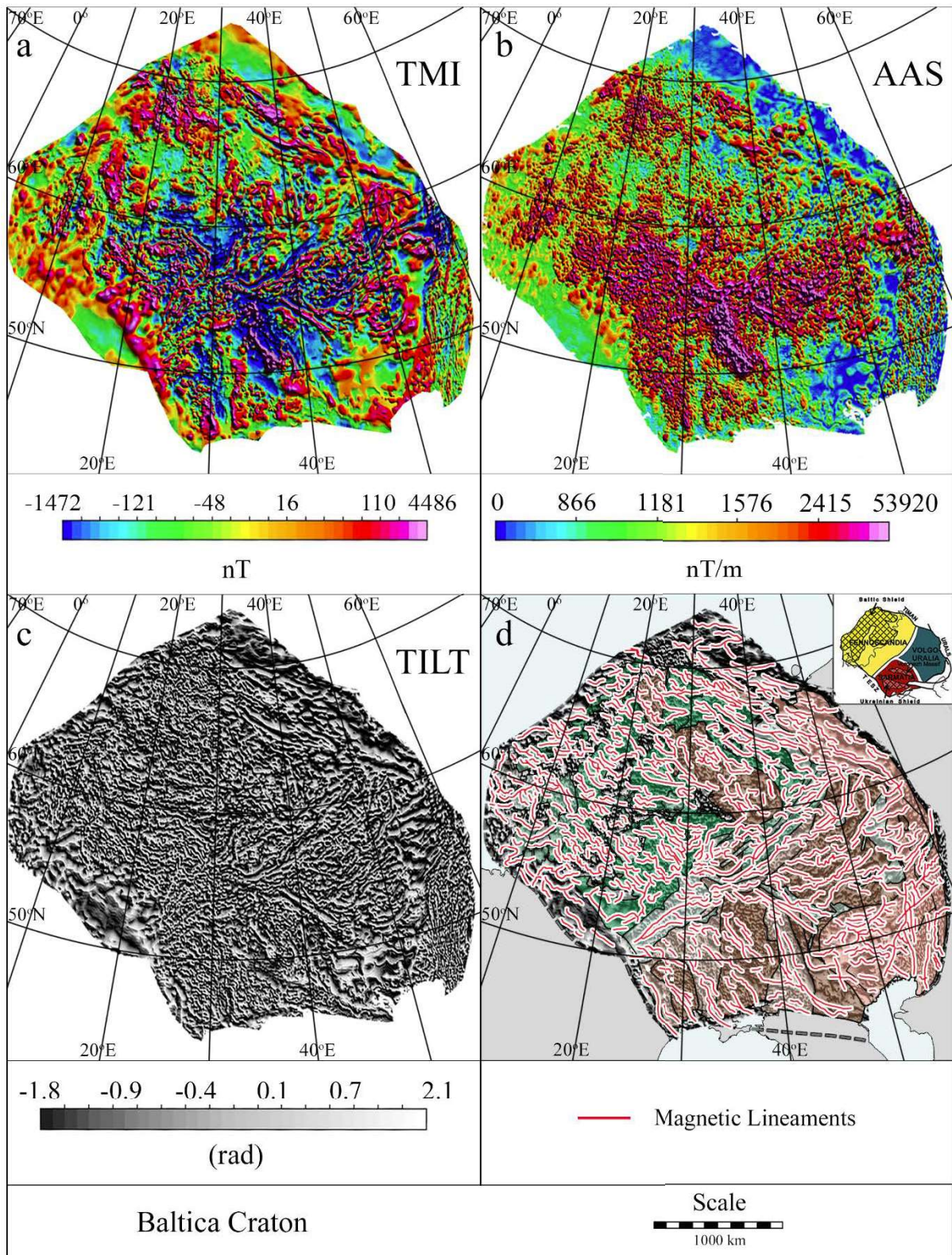
378

379 *4.3. Baltic Craton*

380

381 The Baltic Craton shows an overall calm to intermediate magnetic field in its northern and
382 southern portions. A highly agitated east-west trend crosscuts the craton, occupying the region
383 south of Fennoscandia, the collisional orogens between Fennoscandia and Sarmatia, and
384 between Sarmatia and Volgo-Uralia (Fig. 9). We will refer to this trend as the Central Baltica
385 Magnetic regime. The Archean crust in Baltica shows an intermediate magnetic regime in the
386 central Archean terrane of Fennoscandia and in the Archean domain in southern Sarmatia. In
387 northern Fennoscandia and southwestern Sarmatia, the magnetic regime is agitated. In Volgo-
388 Uralia, the Archean crust presents an agitated regime, especially in its southern area (Central
389 Baltica Magnetic regime). In regions composed of reworked Archean crust, a calm regime
390 dominates the magnetic field, except in areas proximal to the Central Baltica Magnetic regime.

391



392

393 Fig. 9 – Baltica Craton: (a) TMI, (b) AAS, (c) Tilt, and (d) Tilt map overlain by the geological
 394 provinces and magnetic lineaments. The colours of the provinces were normalized to the
 395 colours used in the Amazon Craton map (Fig. 4) according with their respective ages.

396 The magnetic field of the Paleoproterozoic crust of Fennoscandia and Volgo-Uralia, shows
397 higher agitation than Archean crust reworked during the same period (Figs. 5 and 9). The late
398 Paleoproterozoic to Mesoproterozoic structures and suites indicate an increasing magnetic
399 setting from calm in the east to agitated in the west, which experienced the late
400 Mesoproterozoic to early Neoproterozoic Sveconorwegian orogeny. In the Central Russian
401 collisional belt, the field remains calm. The mostly inferred passive margins along the northern
402 and eastern borders of the Baltic Craton (Fig. 5) show a predominantly calm regime, with very
403 long wavelength anomalies, typical of this type of tectonic setting (Nemčok, 2016; Parker Jr,
404 2014). The central area of Baltica, corresponding with the eastern limit of the Central Baltica
405 Magnetic regime, is characterized by a sudden increase in the magnetic regime to agitated.

406 The Fennoscandia, Sarmatia and Volgo-Uralia domains, and the intervening collisional
407 orogenic belts, are reflected in the distribution and orientation of the magnetic lineaments from
408 the Baltic craton (Fig. 9d). Fennoscandia shows a WNW-ESE trend in lineaments, except near
409 the western limit of the craton with the Sveconorwegian orogen, where the trend varies from
410 east-west to northeast-southwest. An almost orthogonal trend to the Fennoscandian shield
411 occurs in the collisional zone of Fennoscandia and Sarmatia and continues in the northeast-
412 southwest direction through the Central Russia Collisional Belt. The Volgo-Uralia shield
413 displays a similar ENE-WSW orientation. Sarmatia shows an overall northwest-southeast
414 orientation, slightly oblique to that in Fennoscandia. The inferred 1.4 to 0.7 Ga passive margins
415 of Baltic craton do not show a predominant trend of magnetic lineaments.

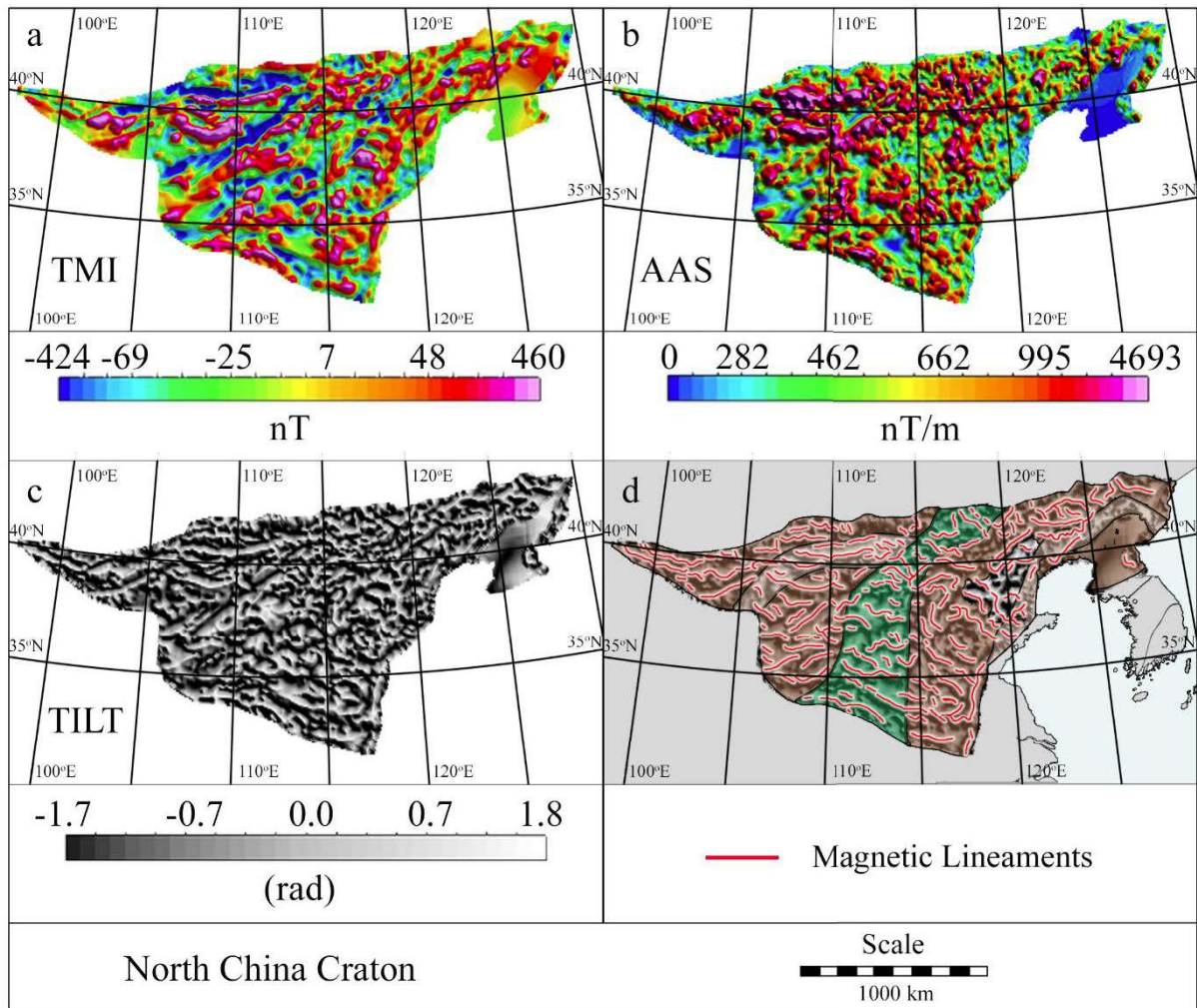
416

417 *4.4. North China Craton*

418

419 The North China Craton is characterized by long wavelength anomalies, and increasing
420 agitation near the limits between the Archean to Paleoproterozoic basement and the orogens
421 and belts (Fig. 10). A northeast-southwest trend is visible in all magnetic fields and derived
422 maps. The Archean to Paleoproterozoic basement presents intermediate to agitated regimes
423 with large magnetic anomalies. The magnetic regimes in the Ordos and Longgang blocks have
424 intermediate frequency, whereas the Yinshan block shows an increased concentration of
425 anomalies. The Nangrim Block, in the Eastern Block, does not have sufficient data to be
426 evaluated.

427



428

429 Fig. 10 – North China Craton: (a) TMI, (b) AAS, (c) Tilt, and (d) Tilt map overlain by the
 430 geological provinces and magnetic lineaments. The colours of the provinces were normalized
 431 to the colours used in the Amazon Craton map (Fig. 4) according with their respective ages.

432

433 The Trans-North China Orogen displays a similar magnetic regime to that of the Ordos and
 434 Longgang blocks, including long wavelengths and intermediate concentration of anomalies.
 435 The Khondalite Belt varies from a calm regime in the west, near the border of the craton, to the
 436 increasing agglomeration of large anomalies from the centre to the eastern end proximal to the
 437 Trans-North China Orogen. The Jiao-Liao-Ji Belt has a calm regime in the south with sparse
 438 anomalies from the centre to the northeast area.

439 In the Archean to Paleoproterozoic basement of the North China Craton, the magnetic
 440 lineament trends show a northeast-southwest pattern in the Ordos Block (Western Block) and
 441 northwest in the Longgang Block (Eastern Block) (Fig. 10d). The northwest portion of the

442 craton, marked by the Yinshan Block and the Khondalite Belt shows a predominant east-west
443 trend. The northwest area, containing the Nangrim Block and the Jiao-Liao-Ji Belt, does not
444 have sufficient data to reveal a major trend.

445

446 **5. Results**

447

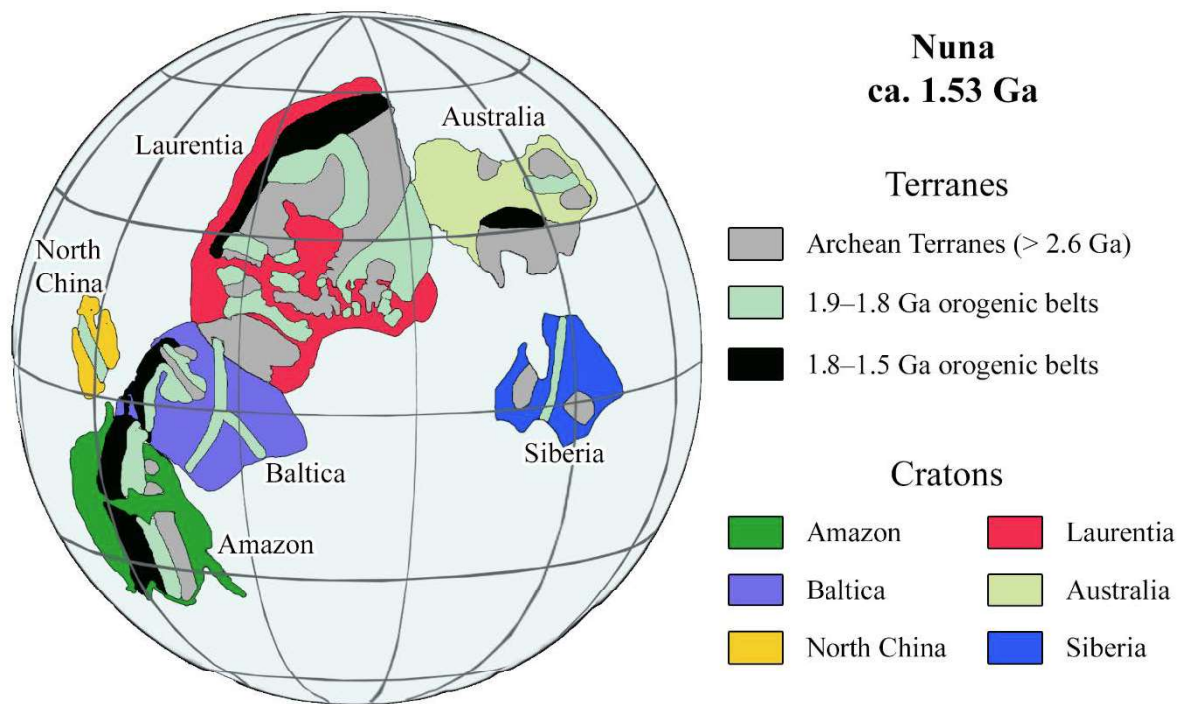
448 Based on mapping the magnetic regimes and lineaments for Amazonia, West Africa, Baltica,
449 and North China, Tilt maps were overlain by geological provinces and magnetic lineaments to
450 compare a variety of proposed Nuna reconstructions (Figs. 12, 14 and 16). This enables a visual
451 comparison of the alignment and possible continuity of magnetic lineaments within and
452 between the cratons. The continuity of provinces based on the magnetic field data was
453 compared with respect to available geological and paleomagnetic data to evaluate the Nuna
454 reconstructions of Mertanen and Pesonen (2012), Pisarevsky et al. (2014) and Pehrsson et al.
455 (2015).

456

457 *5.1. Mertanen and Pesonen (2012)*

458

459 Mertanen and Pesonen (2012) used a compilation of Precambrian paleopoles with minimum
460 Q-values of four (Van der Voo, 1990) to propose Nuna reconstructions for 2.45, 1.88, 1.78,
461 1.63, 1.53, 1.26 and 1.04 Ga. The Q-value is a 7-point measure that determines the quality of
462 a paleopole measurement. Their reconstructions show that by 1.53 Ga an assembled Nuna
463 included a continuous landmass formed by Amazonia, Baltica, Laurentia and Australia (Fig.
464 11). Siberia and North China cratons are disconnected from this main landmass reflecting a
465 lack of continuity between their Paleoproterozoic and older orogenic belts with coeval units in
466 their proposed reconstruction. The position of Amazonia with respect to Baltica is based on the
467 inferred continuity of the 1.9 Ga to 1.8 Ga Ventuari-Tapajós Province with the Svecofennian,
468 and the 1.8 Ga to 1.5 Ga Rio Negro-Juruena provinces with the Trans-Scandinavian Igneous
469 Belt. Laurentia is orientated so the 1.8 Ga to 1.5 Ga orogenic belts along its eastern and
470 southwestern margins face an open ocean, thus forming a long lasting accretionary orogen that
471 was only terminated with the Mesoproterozoic Grenville collisional event (Cawood and
472 Pisarevsky, 2017; Hynes and Rivers, 2010; Karlstrom et al., 2000; Zhao et al., 2002).



473

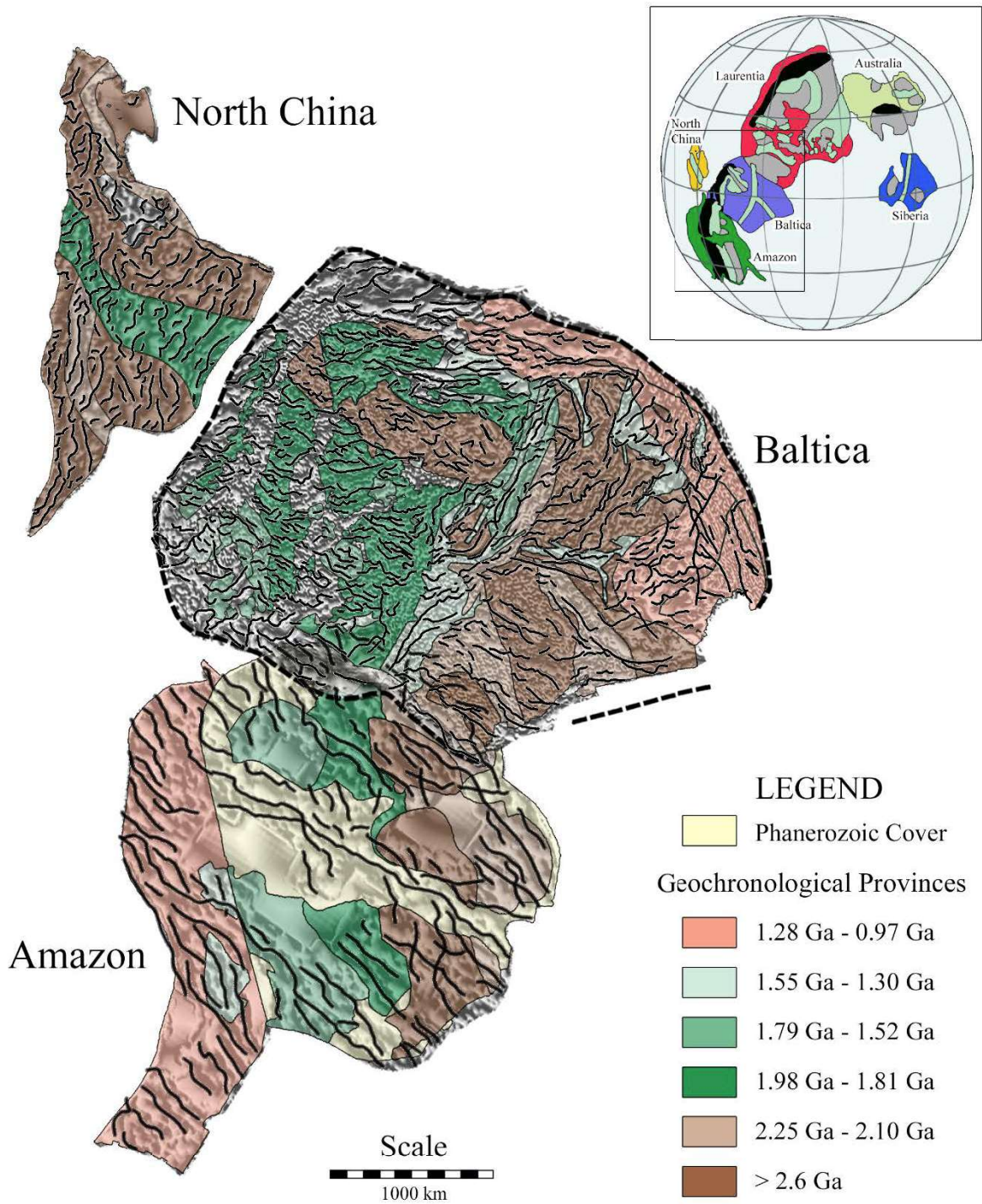
474

Fig. 11 – Nuna reconstruction at 1.53 Ga.

475

476 The Nuna reconstruction proposed by Mertanen and Pesonen (2012) shows Baltica and the
 477 North China cratons adjacent to the Amazon Craton (Figs. 11 and 12). The Amazon Craton is
 478 rotated approximately 35° clockwise, whereas Baltica is rotated 20° and North China 78° anti-
 479 clockwise relative to their present orientation. The magnetic lineaments of the Paleo- to
 480 Mesoproterozoic domains from Amazon and Baltica are sub-parallel, displaying a northwest-
 481 southeast trend. The Archean Central Amazon and the Archean crust of Sarmatia maintain this
 482 alignment and suggest a connection of both cratons. Although the apparent geological and
 483 geochronological continuity of the Longgang Block and the Trans-North China Orogen with
 484 the Archean and Paleo- to Mesoproterozoic crust of Fennoscandia support their reconstruction,
 485 the magnetic lineaments of North China Craton are near orthogonal to those of Fennoscandia
 486 (Fig. 12).

487



488

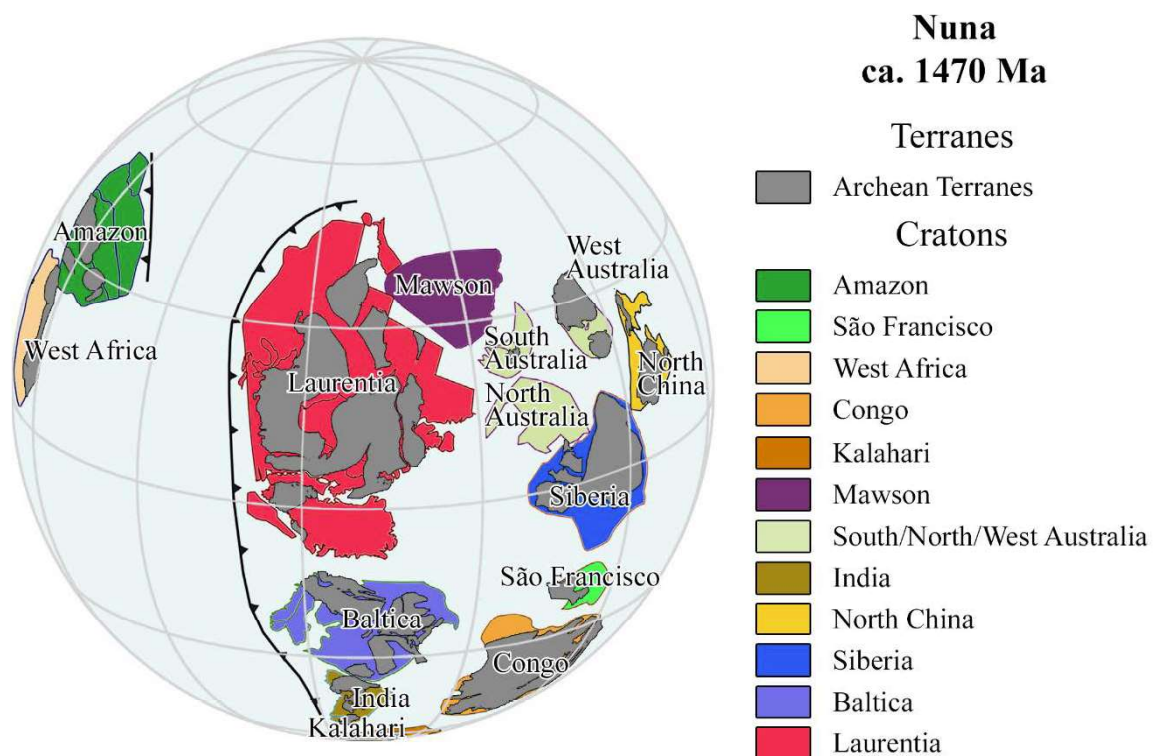
489 Fig. 12 – Nuna reconstruction at 1.53 Ga of the Amazon and adjacent cratons, Baltica and
 490 North China, according to Mertanen and Pesonen (2012), added by the magnetic lineaments.
 491 The colours of the geological units in Baltic and North China cratons were normalized to the
 492 colours of provinces of similar age in the Amazon Craton.

493

495

496 Pisarevsky et al. (2014) used apparent polar wander paths (APWPs) and coeval paired
 497 paleopoles between continents to evaluate possible cratonic connections during the
 498 Proterozoic. They propose a model in which two separated landmasses, East and West Nuna,
 499 formed a single supercontinent between 1650 and 1580 Ma. Pisarevsky et al. (2014) present
 500 the evolution of the Nuna through a series of global paleogeographic reconstructions for 1770,
 501 1720, 1650, 1580, 1500, 1470, 1450, 1380 and 1270 Ma. West Nuna was composed by
 502 Laurentia, Baltica and possibly India, whereas the East Nuna contained Australia, Mawson
 503 (Antarctica), and North China. After ca. 1500 Ma, Siberia and Congo/São Francisco joined
 504 Nuna, whereas West African and the Amazon cratons formed a separate continent from Nuna
 505 (Fig. 13).

506



507

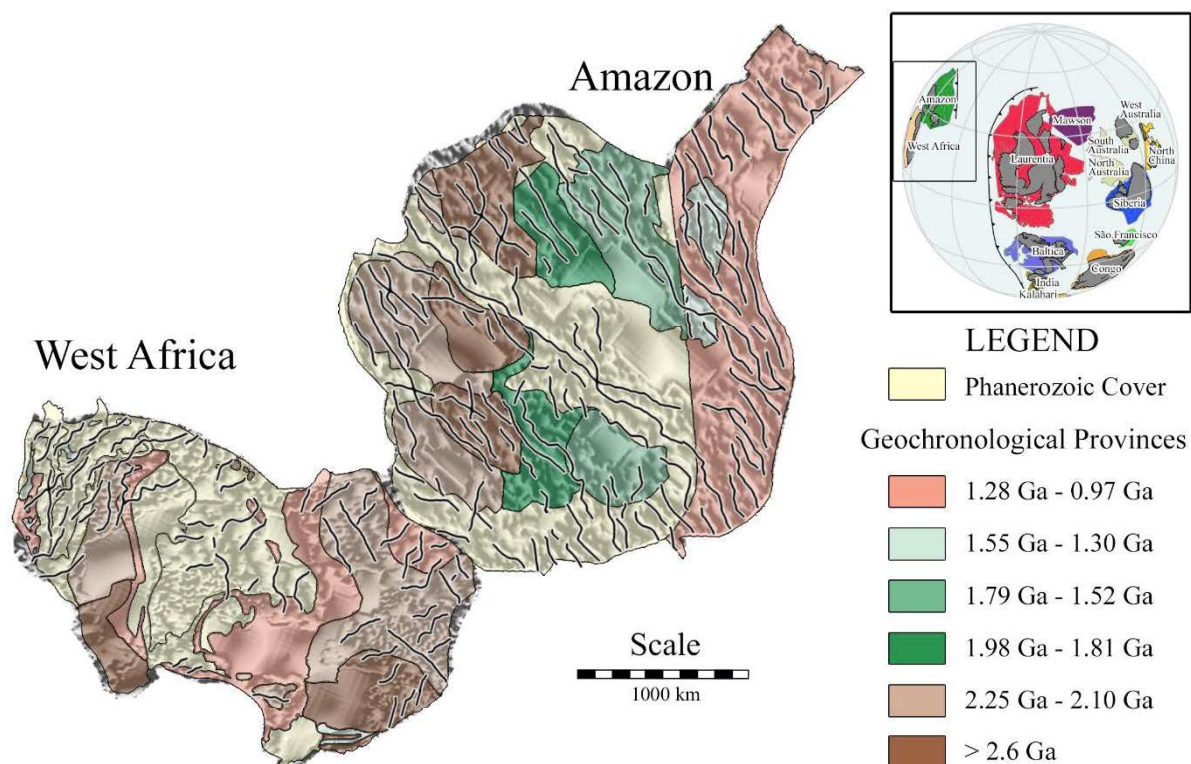
508

Fig. 13 – Nuna reconstruction at ca. 1470 Ma.

509

510 In the Pisarevsky et al. (2014) reconstruction the Amazon and the West African cratons are
 511 separate from the Nuna supercontinent. Both cratons lie northwest of the main Nuna landmass
 512 with Amazonia rotated 137° and the West Africa 74° anti-clockwise relative to their present
 513 orientation. No geological or geochronological continuity between the two cratons is visible in
 514 this reconstruction (Fig. 14). The Paleoproterozoic Maroni-Itacaiúnas (1.98 to 1.81 Ga)
 515 presents a northeast-southwest trend in the magnetic lineaments subparallel with one of the two
 516 trends shown in the Man Shield. None of the remaining domains from the West African Craton
 517 display a similar parallelism with coeval provinces in the Amazon Craton.

518



519

520 Fig. 14 – 1450 Ga Nuna reconstruction of the Amazon and the adjacent West Africa, added
 521 by the magnetic lineaments. The colours of the geological units in the West African Craton
 522 were normalized to the colours of provinces of similar age in the Amazon Craton.

523

524

525

526 5.3. *Pehrsson et al. (2015)*

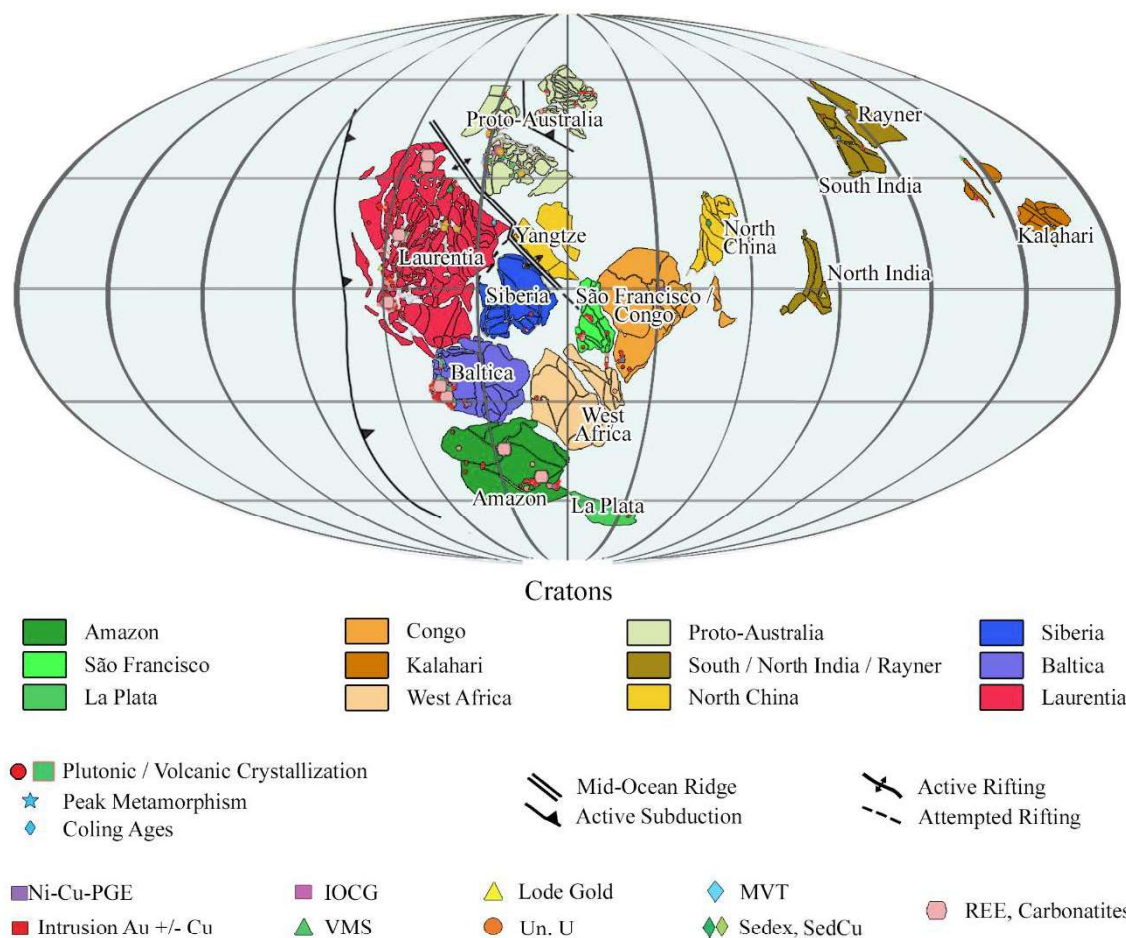
527

528 The reconstruction proposed by Pehrsson et al. (2015) attempts to integrate data from previous
529 models, including paleomagnetic data, with constraints from ore deposit as the formation and
530 preservation of such deposits is linked to the supercontinent cycle (Cawood and Hawkesworth,
531 2015). The deposits types were used to test the reconstructions, based on the expected
532 environment and age for each deposit type; i.e. volcanic-hosted massive sulphides in collisional
533 or accretionary settings, sediment-hosted copper deposits in extensional settings, and uranium
534 mineralization in subtropical latitudes.

535 Pehrsson et al. (2015) show a Nuna reconstruction from 1.6 and 1.4 Ga (Fig. 15), with a main
536 landmass composed of Laurentia, Baltic, Amazon, Rio de la Plata, West African, Siberia and
537 São Francisco/Congo cratons. Proto-Australia (South, North and West Australia) and the
538 Yangtze cratons are located northeast of the main Nuna mass and separated by a zone
539 undergoing regional extension, leading ultimately to ocean formation. North China, North and
540 South India, Rayner and the Kalahari cratons are separate from Nuna.

541

Nuna
Between 1.6 and 1.4 Ga



542

543

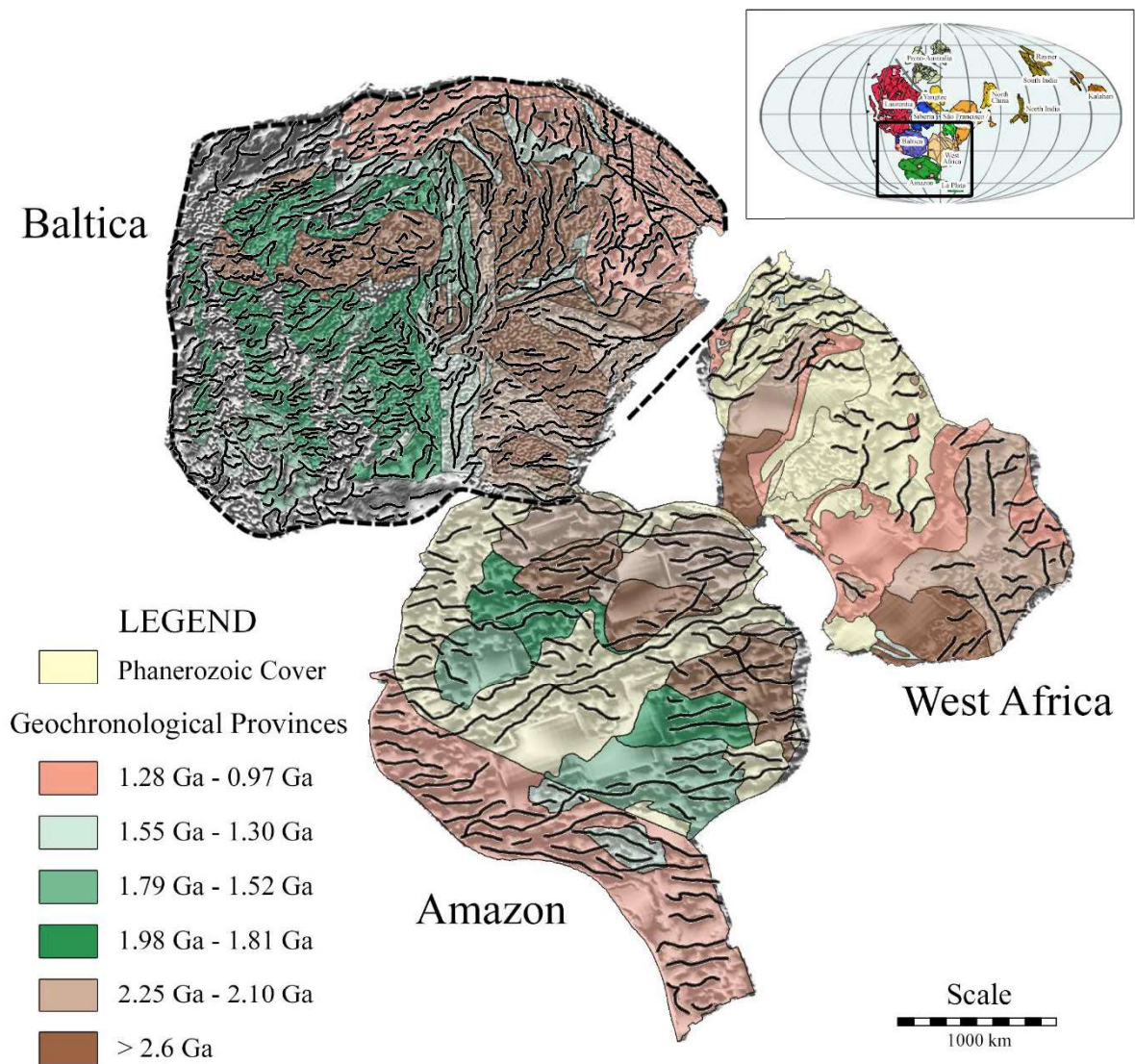
Fig. 15 – Reconstruction of Nuna for the period from 1.6 to 1.45 Ga.

544

545 The Pehrsson et al. (2015) reconstruction locates the Amazon Craton in the southern
 546 hemisphere, to the south-southeast of Baltica and to the southwest of West Africa (Fig. 16).
 547 This reconstruction involves anticlockwise rotation of the Amazon Craton by 20°, Baltica by
 548 51°, and West Africa by 48°. The WNW-ESE-oriented magnetic lineaments of the Ventuari-
 549 Tapajós province are subparallel to the lineaments in the Paleo- to Mesoproterozoic crust of
 550 Fennoscandia, so are the lineaments in the Maroni-Itacaiúnas and the Paleoproterozoic crust of
 551 Sarmatia (Fig. 5). The West African Craton, connected with the present east of the Amazon
 552 Craton, displays a similar parallelism between the lineaments of the coeval Man Shield (West
 553 Africa), the Maroni-Itacaiúnas province (Amazon) and the Sarmatia Paleoproterozoic crust
 554 (Baltica). Lineaments from the south of the Central Amazon province also show a subparallel

555 trend to the lineaments of the Archean domain in the southern part of West Africa. In this last
 556 case, however, the parallelism is speculative, given the small number and size of the lineaments
 557 in the West Africa due to absence of magnetic field data.

558



559

560 Fig. 16 – Southern area of Nuna reconstruction for the period of 1.60 to 1.40 Ga, added by
 561 the magnetic lineaments. This area presents the Amazon Craton adjacent to Baltica and West
 562 Africa. The colours of the geological units in Baltic and West African cratons were
 563 normalized to the colours of provinces of similar age in the Amazon Craton.

564

565

6. Discussion

566
567

568 Magnetic anomaly patterns of sources in blocks of different cratons should be different of each
569 other, unless they were together during their formation and/or overprinted during reworking by
570 younger events. The comparison of anomalies for the Amazon, West African, Baltic and North
571 China cratons shows that coeval and possibly related Paleo- to Mesoproterozoic domains in
572 the different cratons have different sizes of anomalies. Thus, the wavelength of anomalies for
573 Amazon and West Africa are predominantly larger than those in Baltica (Figs. 7 to 9; compare
574 the Maroni-Itacaiúnas, Man Shield and the Paleo- to Mesoproterozoic crust of Fennoscandia).
575 Reasons for these differences could include distortion caused by different projections of large
576 landmasses, and the different resolution and amount of data of the compiled magnetic surveys.

577 In the Mertanen and Pesonen (2012) reconstruction, the approximately coeval Paleo- to
578 Mesoproterozoic provinces in Amazon, Baltic and North China cratons show north-south
579 continuity between the first two cratons, and northwest-southeast with the last two. The
580 Longgang Block of the North China Craton is well aligned with the Archean crust of
581 Fennoscandia, and the Mesoproterozoic terranes (1.79 to 1.52 Ga) of Amazon and
582 Fennoscandia also maintain continuity. The continuity does not, however, extend to the
583 Archean Western Block of North China Craton, which has no counterpart in either Amazon or
584 Baltica. These latter two cratons were still accreting younger provinces until 1.53 Ga, whereas
585 the North China was already stabilized by this time. The lineaments in the 1.98 to 1.81 Ga
586 domains in Amazon and Baltica are well aligned but not with the North China Craton, which
587 are almost orthogonal orientation to those in the other two cratons. The Amazon and Baltica
588 domains show concordant magnetic regimes, which again cannot be extended to those of the
589 North China Craton.

590 The model of Pisarevsky et al. (2014) is the only one in which the Amazon Craton, along with
591 West Africa, is not included within Nuna in the Mesoproterozoic (Figs. 1 and 14). The relative
592 orientation and juxtaposition of Amazonia and West Africa proposed by Pisarevsky et al.
593 (2014) is not supported by the geological and magnetic data which lack continuity between the
594 two cratons, except perhaps for a small number of lineaments in the Maroni-Itacaiúnas
595 province and Man Shield due to 2.15-2.14 Ga calc-alkaline magmatism in the former (da Rosa-
596 Costa et al., 2006), and the 2.15 Ga Eburnean orogeny in the latter (Abouchami et al., 1990).
597 The Maroni-Itacaiúnas province and the Man Shield, however, show divergent magnetic

598 regimes, the Amazonic domain shows an agitated behaviour, whereas the West African Man
599 Shield presents a calm regime.

600 Pehrsson et al. (2015), like Mertanen and Pesonen (2012), locate Baltica to the north of the
601 Amazon Craton but with a further additional rotation of Baltica to further enhance geological
602 compatibility and continuity of the 1.98 to 1.81 Ga Ventuari-Tapajós province of the Amazon
603 Craton with the coeval terranes of Fennoscandia. This rotation promoted the contact of the 2.25
604 to 2.10 Ga Maroni-Itacaiúnas with the reworked 2.20 to 2.00 Paleoproterozoic crust of
605 Sarmatia. This contact, in the Tilt map (Fig. 14), reveals possible lineament continuity in the
606 extreme north of the Amazonic domain with the Sarmatian crust to the southwest. As discussed
607 with respect to the Mertanen and Pesonen (2012) reconstruction, the connection of Baltica with
608 the Amazon Craton is supported by the magnetic regimes of the coeval domains. The West
609 African Craton, which is significantly rotated from the position proposed by Pisarevsky et al.
610 (2014), allows the alignment of the lineaments from the Central Amazon and the Maroni-
611 Itacaiúnas provinces with the Archean domain and Man Shield, respectively. Evaluating the
612 continuity and parallelism of lineaments between the West Africa and Baltica is impaired by
613 the absence of data in several areas of the West African Craton.

614

615 7. Conclusions

616

617 The configuration of the Nuna supercontinent is a matter of ongoing debate as indicated by the
618 diverse distribution of cratonic blocks in the recent reconstructions of Mertanen and Pesonen
619 (2012), Pisarevsky et al. (2014), and Pehrsson et al. (2015). These models, as well as many
620 others (e.g. D'Agrella-Filho et al., 2012; Evans and Mitchell, 2011; Johansson, 2009; Rogers
621 and Santosh, 2002; Zhao et al., 2004), involve a similar configuration for the supercontinents
622 cratonic core juxtaposing northeast Laurentia and northern Baltica, with Siberia occupying an
623 adjacent or nearby position (e.g. Fig. 1). But the configuration of other continental blocks with
624 respect to this core assemblage, and even if these other cratonic fragments were part of Nuna
625 or separate continents, is unresolved. Most attempts to reconstruct Nuna are based on a
626 combination of geologic, geochemical, paleomagnetic, ore deposit data, with variations
627 between models often reflecting differences in the emphasis placed on the different data sets.
628 Thus, in the models evaluated here in, Mertanen and Pesonen (2012) and Pisarevsky et al.
629 (2014) integrated a combination of geological and paleomagnetic data, while Pehrsson et al.

630 (2015) also used isotopic and ore deposit data. In our evaluation of models of Nuna
631 reconstruction, we incorporated a worldwide compilation of magnetic field data (magnetic field
632 EMAG2). We used this to analyse the magnetic regime of each of the lithotectonic domains
633 recognized in the Amazon, West African, Baltic and North China cratons, as well as the
634 wavelength of the magnetic anomalies, and magnetic lineaments, which we then compare with
635 proposed paleogeographic configurations for these blocks.

636 Similarities in the geology, age, magnetic regime, and lineaments between Archean to
637 Mesoproterozoic domains of the Amazon and Baltic cratons are consistent with the
638 reconstructions of Mertanen and Pesonen (2012) and Pehrsson et al. (2015). The geological
639 data for the North China Craton shows some similarities to the adjoining Amazonia and Baltic
640 cratons in the configuration proposed by Mertanen and Pesonen (2012), but not in the magnetic
641 field evidence. The connections between the West African and Amazon cratons proposed by
642 Pisarevsky et al. (2014) and Pehrsson et al. (2015) are not entirely supported by the magnetic
643 field data. However, juxtaposition of the present western or southern border of the West
644 African Craton with the northeast of the Amazon Craton would align the magnetic features of
645 the two cratons.

646 Of three Nuna evaluated reconstructions, the model of Pehrsson et al. (2015) agrees best with
647 the magnetic field data. It locates the Amazon Craton towards the southern portion of the Nuna
648 supercontinent, connected to the West African and Baltic cratons, with an open ocean to its
649 west, where continuous accretion would occur until the mid-Neoproterozoic.

650

651 **8. Acknowledgements**

652

653 This work was done with the support of the CNPq, National Council for Technological and
654 Scientific Development – Brazil [grant numbers 443355/2014-2, 200473/2015-
655 8,141587/2013-0]; Peter A. Cawood acknowledges support from the Australian Research
656 Council [grant number FL160100168].

657

658

659 **9. References**

660

661 Abouchami, W., Boher, M., Michard, A. and Albarede, F., 1990. A major 2.1 Ga event of mafic
662 magmatism in west Africa: An Early stage of crustal accretion. *Journal of Geophysical*
663 *Research: Solid Earth*, 95(B11): 17605-17629.

664 Bahlburg, H., Vervoort, J.D., Du Frane, S.A., Bock, B., Augustsson, C. and Reimann, C., 2009.
665 Timing of crust formation and recycling in accretionary orogens: Insights learned from
666 the western margin of South America. *Earth-Science Reviews*, 97(1–4): 215-241.

667 Beckinsale, R.D., Gale, N.H., Pankhurst, R.J., Macfarlane, A., Crow, M.J., Arthurs, J.W. and
668 Wilkinson, A.F., 1980. Discordant Rb-Sr and Pb-Pb whole rock isochron ages for the
669 Archaean basement of Sierra Leone. *Precambrian Research*, 13(1): 63-76.

670 Bettencourt, J.S., Leite Jr, W.B., Ruiz, A.S., Matos, R., Payolla, B.L. and Tosdal, R.M., 2010.
671 The Rondonian-San Ignacio Province in the SW Amazonian Craton: An overview.
672 *Journal of South American Earth Sciences*, 29(1): 28-46.

673 Bingen, B., Andersson, J., Soderlund, U. and Moller, C., 2008. The Mesoproterozoic in the
674 Nordic countries. *Episodes*, 31(1): 29-34.

675 Bispo-Santos, F., D'Agrella-Filho, M.S., Pacca, I.I.G., Janikian, L., Trindade, R.I.F., Elming,
676 S.-A., Silva, J.A., Barros, M.A.S. and Pinho, F.E.C., 2008. Columbia revisited:
677 Paleomagnetic results from the 1790 Ma colider volcanics (SW Amazonian Craton,
678 Brazil). *Precambrian Research*, 164(1–2): 40-49.

679 Bispo-Santos, F., D'Agrella-Filho, M.S., Trindade, R.I.F., Elming, S.-Å., Janikian, L.,
680 Vasconcelos, P.M., Perillo, B.M., Pacca, I.I.G., da Silva, J.A. and Barros, M.A.S., 2012.
681 Tectonic implications of the 1419 Ma Nova Guarita mafic intrusives paleomagnetic
682 pole (Amazonian Craton) on the longevity of Nuna. *Precambrian Research*, 196–197:
683 1-22.

684 Bogdanova, S., De Waele, B., Bibikova, E., Postnikov, A. and Popova, L., 2005. Volgo-Uralia:
685 SHRIMP evidence of strong Palaeoproterozoic reworking of the Archaean crust,
686 Supercontinents and Earth Evolution: Fremantle, Western Australia, Geological
687 Society of Australia Inc., Symposium 2005, Abstracts, pp. 118.

688 Bogdanova, S., Gorbatshev, R., Grad, M., Janik, T., Guterch, A., Kozlovskaya, E., Motuza,
689 G., Skridlaite, G., Starostenko, V., Taran, L., EUROBRIDGE and *, P.W.G., 2006.
690 EUROBRIDGE: new insight into the geodynamic evolution of the East European
691 Craton. *Geological Society, London, Memoirs*, 32(1): 599-625.

- 692 Bogdanova, S.V., Bingen, B., Gorbatshev, R., Kheraskova, T.N., Kozlov, V.I., Puchkov, V.N.
693 and Volozh, Y.A., 2008. The East European Craton (Baltica) before and during the
694 assembly of Rodinia. *Precambrian Research*, 160(1–2): 23-45.
- 695 Boger, S.D., Raetz, M., Giles, D., Etchart, E. and Fanning, C.M., 2005. U–Pb age data from
696 the Sunsas region of Eastern Bolivia, evidence for the allochthonous origin of the
697 Paragua Block. *Precambrian Research*, 139(3–4): 121-146.
- 698 Cawood, P.A. and Hawkesworth, C.J., 2015. Temporal relations between mineral deposits and
699 global tectonic cycles. *Geological Society, London, Special Publications*, 393(1): 9-21.
- 700 Cawood, P.A. and Pisarevsky, S.A., 2017. Laurentia-Baltica-Azononia relations during
701 Rodinia assembly. *Precambrian Research*.
- 702 Cordani, U.G., Fraga, L.M., Reis, N., Tassinari, C.C.G. and Brito-Neves, B.B., 2010. On the
703 origin and tectonic significance of the intra-plate events of Grenvillian-type age in
704 South America: A discussion. *Journal of South American Earth Sciences*, 29(1): 143-
705 159.
- 706 Cordani, U.G. and Teixeira, W., 2007. Proterozoic accretionary belts in the Amazonian Craton.
707 *Geological Society of America Memoirs*, 200: 297-320.
- 708 D'Agrella-Filho, M.S., Trindade, R.I.F., Elming, S.A., Teixeira, W., Yokoyama, E., Tohver,
709 E., Geraldes, M.C., Pacca, I.I.G., Barros, M.A.S. and Ruiz, A.S., 2012. The 1420 Ma
710 Indiavai Mafic Intrusion (SW Amazonian Craton): Paleomagnetic results and
711 implications for the Columbia supercontinent. *Gondwana Research*, 22(3-4): 956-973.
- 712 da Rosa-Costa, L.T., Lafon, J.M. and Delor, C., 2006. Zircon geochronology and Sm–Nd
713 isotopic study: Further constraints for the Archean and Paleoproterozoic geodynamical
714 evolution of the southeastern Guiana Shield, north of Amazonian Craton, Brazil.
715 *Gondwana Research*, 10(3–4): 277-300.
- 716 Dong, C., Liu, D., Li, J., Wang, Y., Zhou, H., Li, C., Yang, Y. and Xie, L., 2007.
717 Palaeoproterozoic Khondalite Belt in the western North China Craton: New evidence
718 from SHRIMP dating and Hf isotope composition of zircons from metamorphic rocks
719 in the Bayan Ul-Helan Mountains area. *Chinese Science Bulletin*, 52(21): 2984-2994.
- 720 El Bahat, A., Ikenne, M., Söderlund, U., Cousens, B., Youbi, N., Ernst, R., Soulaïmani, A., El
721 Janati, M.h. and Hafid, A., 2013. U–Pb baddeleyite ages and geochemistry of dolerite
722 dykes in the Bas Drâa Inlier of the Anti-Atlas of Morocco: Newly identified 1380 Ma
723 event in the West African Craton. *Lithos*, 174: 85-98.
- 724 Emslie, R.F., Hamilton, M.A., Th, xe and riault, R.J., 1994. Petrogenesis of a Mid-Proterozoic
725 Anorthosite-Mangerite-Charnockite-Granite (AMCG) Complex: Isotopic and

726 Chemical Evidence from the Nain Plutonic Suite. *The Journal of Geology*, 102(5): 539-
727 558.

728 Ennih, N. and Liégeois, J.-P., 2008. The boundaries of the West African craton, with special
729 reference to the basement of the Moroccan metacratonic Anti-Atlas belt. *Geological*
730 *Society, London, Special Publications*, 297(1): 1-17.

731 Evans, D.A.D. and Mitchell, R.N., 2011. Assembly and breakup of the core of
732 Paleoproterozoic–Mesoproterozoic supercontinent Nuna. *Geology*, 39(5): 443-446.

733 Grant, F.S., 1985a. Aeromagnetism, geology and ore environments, I. Magnetite in igneous,
734 sedimentary and metamorphic rocks: An overview. *Geoexploration*, 23(3): 303-333.

735 Grant, F.S., 1985b. Aeromagnetism, geology and ore environments, II. Magnetite and ore
736 environments. *Geoexploration*, 23(3): 335-362.

737 Guerrak, S., 1989. Time and space distribution of Palaeozoic oolitic ironstones in the Tindouf
738 Basin, Algerian Sahara. *Geological Society, London, Special Publications*, 46(1): 197-
739 212.

740 Hurley, P.M., Rand, J.R., Pinson, W.H., Fairbairn, H.W., de Almeida, F.F.M., Melcher, G.C.,
741 Cordani, U.G., Kawashita, K. and Vandoros, P., 1967. Test of Continental Drift by
742 Comparison of Radiometric Ages. A pre-drift reconstruction shows matching geologic
743 age provinces in West Africa and Northern Brazil, 157(3788): 495-500.

744 Hynes, A. and Rivers, T., 2010. Protracted continental collision — evidence from the Grenville
745 Orogen This article is one of a series of papers published in this Special Issue on the
746 theme Lithoprobe — parameters, processes, and the evolution of a continent. *Canadian*
747 *Journal of Earth Sciences*, 47(5): 591-620.

748 Johansson, Å., 2009. Baltica, Amazonia and the SAMBA connection—1000 million years of
749 neighbourhood during the Proterozoic? *Precambrian Research*, 175(1–4): 221-234.

750 Karlstrom, K.E., Bowring, S.A., Dehler, C.M., Knoll, A.H., Porter, S.M., Marais, D.J.D., Weil,
751 A.B., Sharp, Z.D., Geissman, J.W., Elrick, M.B., Timmons, J.M., Crossey, L.J. and
752 Davidek, K.L., 2000. Chuar Group of the Grand Canyon: Record of breakup of Rodinia,
753 associated change in the global carbon cycle, and ecosystem expansion by 740 Ma.
754 *Geology*, 28(7): 619-622.

755 Key, R.M., Loughlin, S.C., Gillespie, M., Del Rio, M., Horstwood, M.S.A., Crowley, Q.G.,
756 Darbyshire, D.P.F., Pitfield, P.E.J. and Henney, P.J., 2008. Two Mesoarchean terranes
757 in the Reguibat shield of NW Mauritania. *Geological Society, London, Special*
758 *Publications*, 297(1): 33-52.

- 759 Kouyaté, D., Söderlund, U., Youbi, N., Ernst, R., Hafid, A., Ikenne, M., Soulaïmani, A.,
760 Bertrand, H., El Janati, M.h. and R'Kha Chaham, K., 2013. U–Pb baddeleyite and
761 zircon ages of 2040 Ma, 1650 Ma and 885 Ma on dolerites in the West African Craton
762 (Anti-Atlas inliers): Possible links to break-up of Precambrian supercontinents. *Lithos*,
763 174: 71-84.
- 764 Maus, S., Barckhausen, U., Berkenbosch, H., Bournas, N., Brozena, J., Childers, V., Dostaler,
765 F., Fairhead, J.D., Finn, C., von Frese, R.R.B., Gaina, C., Golynsky, S., Kucks, R.,
766 Lühr, H., Milligan, P., Mogren, S., Müller, R.D., Olesen, O., Pilkington, M., Saltus, R.,
767 Schreckenberger, B., Thébault, E. and Caratori Tontini, F., 2009. EMAG2: A 2–arc min
768 resolution Earth Magnetic Anomaly Grid compiled from satellite, airborne, and marine
769 magnetic measurements. *Geochemistry, Geophysics, Geosystems*, 10(8): 1-12.
- 770 Mertanen, S. and Pesonen, L.J., 2012. Paleo-Mesoproterozoic Assemblages of Continents:
771 Paleomagnetic Evidence for Near Equatorial Supercontinents. In: I. Haapala (Editor),
772 From the Earth's Core to Outer Space. Springer Berlin Heidelberg, Berlin, Heidelberg,
773 pp. 11-35.
- 774 Nemčok, M., 2016. Rifts and Passive Margins: Structural Architecture, Thermal Regimes, and
775 Petroleum Systems. Cambridge University Press.
- 776 Olesen, O., Ebbing, J., Lundin, E., Maurant, E., Skilbrei, J.R., Torsvik, T.H., Hansen, E.K.,
777 Henningsen, T., Midbøe, P. and Sand, M., 2007. An improved tectonic model for the
778 Eocene opening of the Norwegian–Greenland Sea: Use of modern magnetic data.
779 *Marine and Petroleum Geology*, 24(1): 53-66.
- 780 Parker Jr, E., 2014. Crustal magnetism, tectonic inheritance, and continental rifting in the
781 southeastern United States. *GSA Today*, 24(4).
- 782 Pehrsson, S.J., Eglington, B.M., Evans, D.A.D., Huston, D. and Reddy, S.M., 2015.
783 Metallogeny and its link to orogenic style during the Nuna supercontinent cycle.
784 Geological Society, London, Special Publications, 424.
- 785 Pisarevsky, S.A., Elming, S.-Å., Pesonen, L.J. and Li, Z.-X., 2014. Mesoproterozoic
786 paleogeography: Supercontinent and beyond. *Precambrian Research*, 244: 207-225.
- 787 Reis, N.J., Teixeira, W., Hamilton, M.A., Bispo-Santos, F., Almeida, M.E. and D'Agrella-
788 Filho, M.S., 2013. Avanavero mafic magmatism, a late Paleoproterozoic LIP in the
789 Guiana Shield, Amazonian Craton: U–Pb ID-TIMS baddeleyite, geochemical and
790 paleomagnetic evidence. *Lithos*, 174: 175-195.
- 791 Roest, W.R., Verhoef, J. and Pilkington, M., 1992. Magnetic Interpretation Using the 3-D
792 Analytical Signal. *Geophysics*, 57(1): 116-125.

- 793 Rogers, J.J.W. and Santosh, M., 2002. Configuration of Columbia, a Mesoproterozoic
794 Supercontinent. *Gondwana Research*, 5(1): 5-22.
- 795 Rotherham, J.F., 1997. A metasomatic origin for the iron-oxide Au-Cu Starra orebodies,
796 Eastern Fold Belt, Mount Isa Inlier. *Mineralium Deposita*, 32(3): 205-218.
- 797 Sadowski, G.R. and Bettencourt, J.S., 1996. Mesoproterozoic tectonic correlations between
798 eastern Laurentia and the western border of the Amazon Craton. *Precambrian Research*,
799 76(3): 213-227.
- 800 Shchipansky, A.A., Samsonov, A.V., Petrova, A.Y. and Larionova, Y.O., 2007. Geodynamics
801 of the eastern margin of Sarmatia in the Paleoproterozoic. *Geotectonics*, 41(1): 38-62.
- 802 Söderlund, U., Ibanez-Mejia, M., El Bahat, A., Ernst, R.E., Ikenne, M., Soulaïmani, A., Youbi,
803 N., Cousens, B., El Janati, M.h. and Hafid, A., 2013. Reply to Comment on “U–Pb
804 baddeleyite ages and geochemistry of dolerite dykes in the Bas-Drâa inlier of the Anti-
805 Atlas of Morocco: Newly identified 1380 Ma event in the West African Craton” by
806 André Michard and Dominique Gasquet. *Lithos*, 174: 101-108.
- 807 Soulaïmani, A. and Burkhard, M., 2008. The Anti-Atlas chain (Morocco): the southern margin
808 of the Variscan belt along the edge of the West African craton. *Geological Society*,
809 London, Special Publications, 297(1): 433-452.
- 810 Tassinari, C.C.G. and Macambira, M.J.B., 1999. Geochronological provinces of the
811 Amazonian Craton. *Episodes*, 22(3): 174-182.
- 812 Teixeira, W., Geraldes, M.C., Matos, R., Ruiz, A.S., Saes, G. and Vargas-Mattos, G., 2010. A
813 review of the tectonic evolution of the Sunsas belt, SW Amazonian Craton. *Journal of*
814 *South American Earth Sciences*, 29(1): 47-60.
- 815 Tohver, E., Teixeira, W., van der Pluijm, B., Geraldes, M.C., Bettencourt, J.S. and Rizzotto,
816 G., 2006. Restored transect across the exhumed Grenville orogen of Laurentia and
817 Amazonia, with implications for crustal architecture. *Geology*, 34(8): 669-672.
- 818 Van der Voo, R., 1990. The reliability of paleomagnetic data. *Tectonophysics*, 184(1): 1-9.
- 819 Verduzco, B., Fairhead, J.D., Green, C.M. and MacKenzie, C., 2004. New insights into
820 magnetic derivatives for structural mapping. *The Leading Edge*, 23(2): 116-119.
- 821 Wilde, S.A., Cawood, P.A., Wang, K. and Nemchin, A.A., 2005. Granitoid evolution in the
822 Late Archean Wutai Complex, North China Craton. *Journal of Asian Earth Sciences*,
823 24(5): 597-613.
- 824 Williams, H., Hoffman, P.F., Lewry, J.F., Monger, J.W.H. and Rivers, T., 1991. Anatomy of
825 North America: thematic geologic portrayals of the continent. *Tectonophysics*, 187(1):
826 117-134.

827 Windley, B.F., 1987. Geology and mineral resources of West Africa by J.B. Wright et al., Allen
828 & Unwin, 1985. No. of pages: 187. Price: £30.00 (hardback). Geological Journal,
829 22(S1): 211-212.

830 Wu, K.K., Zhao, G., Sun, M., Yin, C., He, Y. and Tam, P.Y., 2013. Metamorphism of the
831 northern Liaoning Complex: Implications for the tectonic evolution of Neoproterozoic
832 basement of the Eastern Block, North China Craton. *Geoscience Frontiers*, 4(3): 305-
833 320.

834 Youbi, N., Kouyaté, D., Söderlund, U., Ernst, R.E., Soullaimani, A., Hafid, A., Ikenne, M., El
835 Bahat, A., Bertrand, H., Rkha Chaham, K., Ben Abbou, M., Mortaji, A., El Ghorfi, M.,
836 Zouhair, M. and El Janati, M.h., 2013. The 1750 Ma Magmatic Event of the West
837 African Craton (Anti-Atlas, Morocco). *Precambrian Research*, 236: 106-123.

838 Zhao, G. and Cawood, P.A., 2012. Precambrian geology of China. *Precambrian Research*, 222–
839 223: 13-54.

840 Zhao, G., Cawood, P.A., Li, S., Wilde, S.A., Sun, M., Zhang, J., He, Y. and Yin, C., 2012.
841 Amalgamation of the North China Craton: Key issues and discussion. *Precambrian*
842 *Research*, 222–223: 55-76.

843 Zhao, G., Cawood, P.A., Wilde, S.A. and Sun, M., 2002. Review of global 2.1–1.8 Ga orogens:
844 implications for a pre-Rodinia supercontinent. *Earth-Science Reviews*, 59(1–4): 125-
845 162.

846 Zhao, G., Sun, M., Wilde, S.A. and Li, S., 2004. A Paleo-Mesoproterozoic supercontinent:
847 assembly, growth and breakup. *Earth-Science Reviews*, 67(1–2): 91-123.

848 Zhao, G., Wilde, S.A., Cawood, P.A. and Sun, M., 2001. Archean blocks and their boundaries
849 in the North China Craton: lithological, geochemical, structural and P–T path
850 constraints and tectonic evolution. *Precambrian Research*, 107(1–2): 45-73.

851 Zhao, G. and Zhai, M., 2013. Lithotectonic elements of Precambrian basement in the North
852 China Craton: Review and tectonic implications. *Gondwana Research*, 23(4): 1207-
853 1240.

5. Conclusions

A few questions were raised in the introduction of this thesis. The questions argued about how much a single suite can tell about itself and the environment around it, about honest mistakes in during geophysical modelling, and the Earth evolution. Three papers were presented proposing answers for these questions. First, a study considering the effects that using inaccurate constraints have in the outcome of potential field data modelling. Then, the development of a geophysical model from this suite, and a geochemical analysis of the tectonic framework and parental magma that resulted in the intrusion of the Figueira Branca Suite. The third and last part of the thesis consisted on using magnetic field data to evaluate supercontinent reconstruction models.

The Figueira Branca Suite is a 1425 Ma layered mafic-ultramafic complex intruded in the Alto Jauru group, southwest Amazon Craton. This suite has been focus of isotopic and paleomagnetic studies, and was the centre of the three studies that composed this thesis. The suite is composed by four northwest-southeast-oriented bodies: Indivaí, Azteca, Figueira Branca and Jauru, from southeast to northwest. The environment that surrounds the Figueira Branca Suite consists in the 1.8 Ga Alto Jauru meta-volcanosedimentary group that hosts the suite, the granite-gneiss Santa Helena (to the west) and Água Clara (to the east) suites.

Modelling, in Earth Sciences, is the ultimate effort to represent a part of the Earth that cannot be entirely seen. Geophysics and geochemistry are two of the sciences that most frequently use modelling. This thesis repeatedly used this resource, from testing how a microscopic analysis affects the constraints used in the modelling, to the evaluation of supercontinent reconstruction models with magnetic field data.

Preliminary data showed abnormally low values of density and magnetic susceptibility in hand samples of the Figueira Branca Suite. A preliminary model was developed using these values as constraints. The shape, depth and remanent magnetization from this model, however, did not agree with geological observations and paleomagnetic data. Hand samples did not display clear signs of weathering or evidences that could explain the low properties, so thin sections were extracted to investigate their possible cause. The thin sections displayed intense weathering and serpentization in some samples. This process justified a deeper investigation on how and how much an inaccurate constraint affect the outcome from modelling. In this case, the density and the magnetic susceptibility were evaluated for gravity (Bouguer anomaly) and magnetic field respectively.

The investigation of the effects of inaccurate constraints was made using a synthetic model and real data from the Indiavaí body, the southernmost intrusion of the Figueira Branca Suite. The investigated cases proved that using inaccurate constraints can produce errors about 50% higher than the correct and shapes significantly different than the reality. The results also showed that in cases that a more thorough analysis in the sources of the constraints, the best solution is to perform the modelling setting the constraints free, instead of fixing inaccurate values and forcing the reduction of the error through the variation of depth and shape of the models.

With a reliable modelling methodology and constraints, it was possible to model the remaining anomalies of the suite. Previous studies of the Figueira Branca Suite suggest that it extended further to the north and northeast of the four cited bodies. However, no other analogue geophysical signature in the Jauru Terrane represented an intrusion of the same geological characteristics of the Figueira Branca Suite bodies.

The geophysical models obtained for the suite intrusive bodies displayed very shallow sill-like shapes extending 8 km on average in the northwest direction. Mineralogy and geochemical data indicated gabbroic rocks with predominance of plagioclase, olivine, and variable amounts of intergrown pyroxene. The increasing presence of pyroxene indicated a fractionation in the parental magma, whereas the change in the slope of the REE normalized to chondrites suggested an increase in the amount of melt. Both datasets together permitted to propose the sequence of magma extraction that generated the bodies of the Figueira Branca Suite was: Indiavaí, Figueira Branca, Azteca and Jauru. Trace elements completed the data, displaying evidences of hydrous melts in the parental magma, typical from supra-subduction environments. This geochemical signature for the parental magma, associated with the tectonic framework where the suite is hosted, was interpreted as a magmatism in the back-arc zone of the Santa Helena Orogen.

The answers for how much a suite can tell about itself and the environment that hosts it, and the larger scale analysis of the Jauru Terrane raised the last question: what about the Earth evolution? Where was the Amazon Craton by the time of the Santa Helena orogeny, and when was the Figueira Branca Suite intrusive event? The supercontinent Nuna position and the cratonic fragments that composed it are a matter of ongoing debate. By consequence, the debate extends to the Amazon Craton. Supercontinent reconstructions varies depending the amount and kind of data used to constraint them (e.g. combination of geologic, geochemical, paleomagnetic, and ore deposit data). Three recent reconstructions Mertanen and Pesonen (2012), Pisarevsky et al. (2014), and Pehrsson et al. (2015) suggest different configurations for the Nuna supercontinent, where Amazonia is adjacent to the West African, Baltic and/or the North China cratons. Using a worldwide compilation of magnetic field data (EMAG2), these reconstructions were analysed based on the magnetic regimes and lineaments of each block, and then the proposed paleogeographic configurations for these blocks.

None of the reconstructions were entirely supported by the magnetic field data, however Pehrsson et al. (2015) reconstruction agrees best with it. This reconstruction locates the Amazon Craton towards the southern portion of the supercontinent, connected in the northeast to the West Africa, and in the north to Baltica cratons. In this reconstruction, the southwest of the Amazon Craton has open ocean to its west, where continuous accretion would occur until the mid-Neoproterozoic, forming the Santa Helena Orogen and, later, the back-arc extension that permitted the intrusion of the Figueira Branca Suite.

6. References

- Bettencourt, J. S., Leite Jr, W. B., Ruiz, A. S., Matos, R., Payolla, B. L., & Tosdal, R. M. (2010). The Rondonian-San Ignacio Province in the SW Amazonian Craton: An overview. *Journal of South American Earth Sciences*, 29(1), 28-46. doi:<http://dx.doi.org/10.1016/j.jsames.2009.08.006>
- Maus, S., Barckhausen, U., Berkenbosch, H., Bournas, N., Brozena, J., Childers, V., . . . Caratori Tontini, F. (2009). EMAG2: A 2-arc min resolution Earth Magnetic Anomaly Grid compiled from satellite, airborne, and marine magnetic measurements. *Geochemistry, Geophysics, Geosystems*, 10(8), 1-12. doi:10.1029/2009GC002471
- Mertanen, S., & Pesonen, L. J. (2012). Paleo-Mesoproterozoic Assemblages of Continents: Paleomagnetic Evidence for Near Equatorial Supercontinents. In I. Haapala (Ed.), *From the Earth's Core to Outer Space* (pp. 11-35). Berlin, Heidelberg: Springer Berlin Heidelberg.
- Pehrsson, S. J., Eglinton, B. M., Evans, D. A. D., Huston, D., & Reddy, S. M. (2015). Metallogeny and its link to orogenic style during the Nuna supercontinent cycle. *Geological Society, London, Special Publications*, 424. doi:10.1144/sp424.5
- Pisarevsky, S. A., Elming, S.-Å., Pesonen, L. J., & Li, Z.-X. (2014). Mesoproterozoic paleogeography: Supercontinent and beyond. *Precambrian Research*, 244, 207-225. doi:<http://dx.doi.org/10.1016/j.precamres.2013.05.014>
- Tassinari, C. C. G., Bettencourt, J. S., Geraldès, M. C., Macambira, M. J. B., & Lafon, J. M. (2000). *The Amazonian Craton*. Paper presented at the 31st International Geological Congress, Rio de Janeiro.
- Tassinari, C. C. G., & Macambira, M. J. B. (1999). Geochronological provinces of the Amazonian Craton. *Episodes*, 22(3), 174-182.
- Teixeira, W., Ernst, R. E., Hamilton, M. A., Lima, G., Ruiz, A. S., & Geraldès, M. C. (2016). Widespread ca. 1.4 Ga intraplate magmatism and tectonics in a growing Amazonia. *Gff*, 138(1), 241-254. doi:10.1080/11035897.2015.1042033
- Teixeira, W., Geraldès, M. C., D'Agrella, M. S., Santos, J. O. S., Barros, M. A. S., Ruiz, A. S., & da Costa, P. C. C. (2011). Mesoproterozoic juvenile mafic-ultramafic magmatism in the SW Amazonian Craton (Rio Negro-Juruena province): SHRIMP U-Pb geochronology and Nd-Sr constraints of the Figueira Branca Suite. *Journal of South American Earth Sciences*, 32(4), 309-323. doi:10.1016/j.jsames.2011.04.011
- Teixeira, W., Geraldès, M. C., Matos, R., Ruiz, A. S., Saes, G., & Vargas-Mattos, G. (2010). A review of the tectonic evolution of the Sunsas belt, SW Amazonian Craton. *Journal of South American Earth Sciences*, 29(1), 47-60. doi:10.1016/j.jsames.2009.09.007

Attachment 1

Aerogamaespectrometria e suas aplicações no mapeamento geológico

Vanessa Biondo Ribeiro

IAG/USP, Brasil

vanessa.ribeiro@usp.com

Marta S. M. Mantovani,

IAG/USP, Brasil

msmmanto@usp.br

Vinicius Hector Abud Louro,

IAG/USP, Brasil

vilouro@usp.br

ABSTRACT *AEROGAMMASPECTROMETRY AND ITS APPLICATIONS IN GEOLOGICAL MAPPING. The substantial increase of geological information in recent years contributed a lot to understand the Brazilian mineral potential. However, much remains to be studied. The geophysics, based especially on potential methods and gamma-spectrometry, has wide applicability on delimiting geotectonic structures and on locating mineral exploration targets. In this work, we focus on interpreting the natural emission of gamma radiation detected on the surface associated to the main radioelements. To this, we presented a description of the main characteristics and data corrections used for an airborne survey. The interpretation of gamma-spectrometric data allows characterizing regions with undifferentiated lithological units, detecting the presence of outcropping igneous intrusions, hydrographic elements, hydrothermal alteration and/or intense erosive processes, contributing significantly on the understanding of a region. To illustrate the contribution, we present as case studies the analysis of data from the region of the Santa Helena Granitic Batholith (MT) and from the Alkaline-Carbonatite Complex of Tapira (MG). Citation: Ribeiro V.B., Mantovani M.S.M., Louro V.H.A. 2014. Aerogamaespectrometria e suas aplicações no mapeamento geológico. *Terræ Didática*, 10(1):29-51. <<http://www.ige.unicamp.br/terraedidatica/>>.*

KEYWORDS: *Gamma ray spectrometry, aerial survey, interpretation of radiometric data.*

RESUMO *O aumento substancial de informações geológicas nos últimos anos contribuiu muito para o conhecimento do potencial mineral do Brasil. Entretanto, ainda há muito a ser estudado. A geofísica, especialmente baseada em métodos potenciais e gamaespectrométricos, tem grande aplicabilidade na delimitação de estruturas geotectônicas e na localização de alvos exploratórios minerais. Neste trabalho focalizamos a interpretação da emissão de radiação gama natural detectada na superfície associada aos principais radioelementos. Para tal, apresentamos uma descrição das características do aerolevanteamento e das correções realizadas. A interpretação de dados gamaespectrométricos permite caracterizar regiões com unidades litológicas indivisas, detectar a presença de intrusões ígneas aflorantes, elementos hidrográficos, alteração hidrotermal e/ou intensos processos erosivos, contribuindo significativamente para o entendimento de uma região. Para ilustrar a contribuição, apresentamos como estudos de caso a análise de dados da região do Batólito Granítico de Santa Helena (MT) e do Complexo Alcalino-Carbonatítico de Tapira (MG).*

PALAVRAS-CHAVES: *Gamaespectrometria, aerolevanteamento, interpretação de dados radiométricos.*

Magnetic field analysis of Morro do Leme nickel deposit

Vinicius Hector Abud Louro¹, Marta Silvia Maria Mantovani¹, and Vanessa Biondo Ribeiro¹

ABSTRACT

The Morro do Leme laterite nickel deposit lies inside the western border of the Parecis Basin (Brazil). This deposit is characterized by high concentrations of lateritic Ni (about 1.8%) and anomalous contents of Pd, Au, Cu, Na, Co, Zn, and Pt in a peridotite and dunite layered intrusion. Besides the existence of geochemical and drilling data, the 3D distribution in the subsurface of this layered intrusion is still unknown. An airborne magnetic survey revealed three east–west elongated magnetic anomalies, characterized by a significant remanent magnetization. The sources of these anomalies were delimited laterally and had their depths estimated between 90 and 150 m, using techniques that use derivatives. Further, the total magnetization direction was obtained from a distortion analysis of the magnetic anomalies. All these data were united in an initial model for the 3D inversion of the magnetic data. The total and induced magnetization directions were attributed to the inverted model of 0.12 (SI) susceptibility, allowing indirect estimation of the remanence. The model, defined by the depth, the inversion, and the remanence estimates, linked the intrusion to analogue events in the Rondonian-San Ignácio Province. The results indicated that to explore for laterite Ni, the best locations are the southern part of the main anomaly and in the cover above the two smaller anomalies, whereas to explore for Pd, Au, Cu, Na, Co, Zn, and/or Pt, the indicated region is the central portion of the main anomaly.

In the west portion of the Mato Grosso state (Brazil) is the Comodoro Nickel District, characterized by the deposits of Morro do Leme and Morro do Sem Boné, with known occurrences of lateritic nickel. The Morro do Leme total reserves are 14,306,000 t with Ni concentrations of 1.8% (Nunes, 2000).

The Morro do Leme deposit encompasses three hills comprised essentially of dunites and peridotites covered by a laterite layer. Nunes (2000) indicates that the main Ni concentration is located in this layer, the thickness of which ranges from 20 to 40 m. In deeper horizons (approximately 150 m deep), there are intercalated magmatic concentrations of sulfides and chromites, presenting anomalous values for Pd, Au, Cu, Na, Co, Zn, and Pt.

This work analyzed the magnetic field of the deposit considering previous geologic surface mapping and borehole data from its southeastern portion. A procedure using enhanced horizontal derivatives (EHDs) (Fedi and Florio, 2001), to estimate the source border and, further, its depth — named here as the *EHD-depth* — is based on Hsu et al. (1998). The MaxiMin technique (Fedi et al., 1994) used to estimate the angles of the magnetization components. Using these estimates, we composed an initial model for a further inversion of the magnetic data to determine the susceptibility. The magnetization components (geomagnetic and directions estimated through the MaxiMin), when applied to the distribution of susceptibility, generated a scenario in which it was possible to indicate an apparent remanent magnetization that explained the anomaly.

This analysis and its results evidenced regional magnetic field features for the time of crystallization of the deposit's protolith along the best exploration zones for the laterite Ni and for the Pd, Au, Cu, Na, Co, Zn, and Pt-rich horizons.

INTRODUCTION

Nickel laterite deposits are derived from the chemical alteration of olivine-bearing mafic and ultramafic rocks such as dunites and olivine-pyroxene peridotites (Brand et al., 1998).

GEOLOGIC CONTEXT

In the Alto Guaporé belt from the Rondonian-San Ignácio Igneous Province (RSIP), lies the Alto Guaporé Sequence, characterized by Phanerozoic sediments; such types of sediments usually have very low magnetic susceptibility (10^{-5} to 10^{-4} SI) (Telford et al.,

Manuscript received by the Editor 17 March 2014; revised manuscript received 16 August 2014; published online 28 October 2014.

¹Universidade de São Paulo, Instituto de Astronomia, Geofísica e Ciências Atmosféricas, São Paulo, Brazil. E-mail: vilouro@usp.br; msmanto@usp.br; vanessa.ribeiro@usp.br.

© 2014 Society of Exploration Geophysicists. All rights reserved.

Geophysical analysis of Catalão I alkaline–carbonatite complex in Goiás, Brazil

M.S.M. Mantovani¹, V.H.A. Louro^{1*}, V.B. Ribeiro¹, H.S. Requejo²
and R.P.Z. dos Santos¹

¹Rua do Matão, 1226, Cidade Universitária, São Paulo, SP, 05508-090, Brazil, and ²Rua Barão do Triunfo, 550, cj. 56, Campo Belo, São Paulo, SP, 04602-002, Brazil

Received June 2013, revision accepted February 2015

ABSTRACT

The Catalão I alkaline–carbonatite complex, which is located in Central Brazil, is one of the main producers of niobium and phosphates in the world. It has been intensely studied geologically and geochemically for its economic potential. This work presents a geophysical analysis over this complex, identifying its behaviour in the subsurface and in portions that have not been explored yet. Different geophysical methods and techniques were applied to achieve the most reliable results possible: at the surface, through radiometric, geological, and topographic data, and at depth, by geological, magnetic, and gravimetric data. The analysis was successfully completed with inversions of gravity and magnetic data that resulted in quite similar models, both in volume and shape. Their density and magnetic susceptibility contrasts were consistent with the expected dunite–pyroxenite lithology from the original mafic intrusion and indicated (by exclusion) the volume of the carbonatite body, which along with the known contents of phosphates and niobium allowed an indirect estimate of the reserves and resources of the complex.

Key words: Magnetism, Gravity, Inversion.

INTRODUCTION

Catalão I is an ultra-mafic alkaline carbonatite complex, approximately circular, emplaced in the Proterozoic granite–gneiss basement and covered by schists from the Araxá Group along the 125AZ lineament, SE of Goiás State. Rich in Ti, Nb, P, rare-earth elements (REEs) and vermiculite, it is surrounded by kimberlites (Biondi 2003). K–Ar data dates the complex between 82.9 ± 4.2 and 85.0 ± 6.9 Ma (Hasui and Cordani 1968; Sonoki and Garda 1988; Gomes, Ruberti, and Morbidelli 1990).

Alkaline igneous rocks are formed from cooling of magmas derived by small degrees of partial melting of rocks in the Earth's mantle. The formation of alkaline rocks is reported as a geologic process that extracts and concentrates elements

that do not fit into the structure of the common rock-forming minerals. The alkaline magmas are enriched in elements such as zirconium, niobium, strontium, barium, lithium, and the REEs. When these magmas rise through the crust, their chemical composition undergoes further changes resulting in a large diversity of rock types that are variably enriched in economic elements (Long *et al.* 2010).

Alkaline and alkaline–carbonatite complexes dated early to late Cretaceous occur along lineaments in and around the Paraná Basin (South America), with their emplacement regulated by extensional tectonics. In this context, Catalão I was included in the Alto Paranaíba Igneous Province (APIP). According to Gibson *et al.* (1995), the Minas-Goiás Alkaline Province, which includes the APIP, represents one of the most voluminous potassium provinces of the world (larger than 10^6 km³) where, James *et al.* (1993) obtained a crustal thickness of 40 km and a 130-km-thick lithosphere from seismic data.

*E-mail: vilouro@usp.br

Geophysics

Decision Letter (GEO-2016-0345.R4)

From: msacchi@ualberta.ca

To: vilouro@usp.br, vilouro@hotmail.com

CC: arthurcheng@alum.mit.edu, geopapers@seg.org, vilouro@usp.br, vilouro@hotmail.com, msmmanto@usp.br, vanessa.ribeiro@usp.br, msacchi@ualberta.ca

Subject: GEO-2016-0345.R4 Acceptance Pending

Body: 15-Feb-2017

Re: GEO-2016-0345.R4, "Integrated geological and geophysical interpretation of the Buraco da Velha Copper Deposit (Rondônia - Brazil): A basis for exploring in related environments"

Dear Mr. Vinicius Louro,

Your manuscript listed above has been accepted for publication pending SEG's receipt of the final version with minor revisions, production-quality figure files, and all author forms, including completed copyright forms and author-charge forms.

Please upload all files to the system and follow the instructions carefully.

Editor and Reviewer Comments

PLEASE NOTE: Some reviewers and editors may have uploaded or "attached" separate review documents or edits of your manuscript in addition to their comments provided below. To retrieve editor/reviewer attachments, if any were provided, please enter your Author Center at <https://mc.manuscriptcentral.com/geophysics>. The paper will be listed under "Manuscripts Accepted for First Look." Under "status," click "view decision letter." Scroll to the bottom of the screen to view attachments if any were provided.

Body of Manuscript

Preferred formats for production are Microsoft Word and LaTeX, in that order. If your paper is formatted in LaTeX, an SEG LaTeX package is available at <http://reproducibility.org/wiki/SEGTeX>. If your manuscript is formatted in LaTeX, you must also upload a double-spaced PDF file of the text. Also, all LaTeX files, except figures and tables, must be included in one file. The lists of figure and table captions also should be included in this file.

When formatting your paper, please follow "Instructions to Authors" at <http://seg.org/Publications/Journals/Geophysics/Information-for-Authors/Instructions-to-authors>. Be advised your paper will be returned to you if the items below are not submitted in the correct format.

- Author names and affiliations should be listed on the title page of your paper exactly as they should be published.
- The right-running head should be listed on the title page of your paper.
- References should be formatted correctly.
- Tables should be submitted as separate Microsoft Word or Excel files and not embedded in the body of the manuscript.

References

Please also take this opportunity to update your reference list. In the first version of your paper, you may have cited proceedings and abstracts because journal papers were not yet available at that time. If it is possible to replace such citations by citations to journal papers, we encourage you to do so. If necessary, make minor alterations in the text at places where you refer to these papers.

Figures

See Preparation of Illustrations in "Instructions to Authors" at <http://seg.org/Publications/Journals/Geophysics/Information-for-Authors/Instructions-to-authors#preparationofillustrations> for detailed figure instructions and examples. Following these requirements will allow readers a clearer understanding of the ideas you are trying to communicate through your figures.

Please note that figures must be submitted in EPS or TIFF format with color and grayscale images at a resolution of at least 300 dots per inch (dpi) and line art of at least 600 dpi (1200 dpi is preferred) at approximately 4.33 inches wide. If you are uploading TIFF files, please enable LZW compression while saving. Submit each figure in a separate digital file, named according to the figure number (Figure 1, Figure 2, etc.). Do not embed figures in documents. Figures will not be accepted in Microsoft Word, PowerPoint, or Canvas.

130

Publication Forms

Please see the attached Final Submission Guide for links to publication forms. Forms also are

Please see the attached final submission guide for links to publication forms. Forms also are located at <http://seg.org/Publications/Journals/Geophysics/Information-for-Authors/Publication-Forms>. These must be completed and uploaded with your manuscript files.

Uploading Final Documents

When you have made all corrections and prepared all forms and files, please enter your Author Center at <https://mc.manuscriptcentral.com/geophysics> and upload the final production files, forms, etc., to the system.

You will find your manuscript in your Author Center under the list "Manuscripts Accepted for First Look." Click on the link to "submit updated manuscript" and follow the steps as you would during a manuscript-submission process.

Please upload the files to your Author Center at <https://mc.manuscriptcentral.com/geophysics> within 14 days or earlier. Delays without advance notice may result in the withdrawal of your paper.

Proofs

During the production phase of your paper, you are expected to submit your galley-proof corrections within seven business days. Failure to respond on time may result in delayed publication. Be sure to update your coauthors' information within ScholarOne Manuscripts so that staff will have an alternate contact if the primary author is unavailable. If you are the sole author, please provide an alternative contact who can respond in your absence.

Please e-mail geopapers@seg.org with any questions about these instructions.

Thank you and best regards,
Editor Prof. Mauricio Sacchi

 Additional comments of Editor to Author:
(There are no comments)

Assistant Editor: 1
Assistant Editor`s Comment to Author:
(There are no comments.)

Associate Editor: 2
Associate Editor`s Comments for Authors:
(There are no comments.)

Date Sent: 15-Feb-2017

File 1: * [GEO-FinalSubmissionGuide.pdf](#)

 Close Window

Integrated geological and geophysical interpretation of the Buraco da Velha Copper Deposit (Rondônia - Brazil): A basis for exploring in related environments

Journal:	<i>Geophysics</i>
Manuscript ID	GEO-2016-0345.R3
Manuscript Type:	Case Histories
Date Submitted by the Author:	02-Feb-2017
Complete List of Authors:	Louro, Vinicius; Instituto de Astronomia, Geofísica e Ciências Atmosféricas - Universidade de São Paulo, Dept. of Geophysics; University of St. Andrews, Department of Earth and Environmental Sciences Mantovani, Marta; Instituto de Astronomia, Geofísica e Ciências Atmosféricas - Universidade de São Paulo, Dept. of Geophysics Ribeiro, Vanessa; Universidade Federal de Pernambuco, Geologia; Instituto de Astronomia, Geofísica e Ciências Atmosféricas - Universidade de São Paulo, Dept. of Geophysics
Keywords:	magnetics, modeling, sediment, radiometrics, South America
Area of Expertise:	Case Histories

1
2
3
4
5 **Integrated geological and geophysical interpretation of the Buraco da Velha**
6
7 **Copper Deposit (Rondônia - Brazil): A basis for exploring in related environments**
8
9

10
11
12 **Vinicius Hector Abud Louro^{1,2}, Marta Silvia Maria Mantovani¹ and Vanessa**
13
14 **Biondo Ribeiro^{1,3}**
15

16
17
18
19
20 ¹ Instituto de Astronomia, Geofísica e Ciências Atmosféricas, Universidade de São
21
22 Paulo, São Paulo, Brazil.

23
24
25
26 ² Department of Earth and Environmental Sciences, University of St. Andrews, St.
27
28 Andrews, KY16 9AL, UK.

29
30
31 ³ Universidade Federal de Pernambuco, Geologia, Recife, Pernambuco, Brazil.

32
33
34 E-mails: vilouro@usp.br; msmanto@usp.br; van.biondo@gmail.com.
35
36
37
38
39

40 **Corresponding author:** Vinicius Hector Abud Louro.

41
42
43 **E-mail:** vilouro@usp.br
44
45

46 **Phone:** +44 (0) 79773 65802
47
48
49
50

51
52 **Date of Submission:** Original Paper: 30 June 2016
53
54

55 **Running Head:** Geology & Geophysics of Buraco da Velha
56
57
58
59
60

ABSTRACT

The Buraco da Velha copper deposit lies at the northern limit of the Parecis Basin in the Colorado Graben, Rondônia, Brazil. New geophysical data indicates the presence of a magnetic source below and to the north of the Buraco da Velha deposit, where it corresponds with high gamma-ray U, Th and K counts. The source of the magnetic anomaly was studied and delineated through derivative transforms, Euler Deconvolution, MaxiMin total magnetization direction analysis, staged inverse modeling, Th/K ratio, and radiometric ternary image. The magnetic anomaly is elongate in east-west direction and measures 23 km by 6 km, and the top of the source is estimated to lie at depths mostly between 50 and 100 meters. Based on the magnetic model, we indirectly estimate a Jurassic to Cretaceous age, which is compatible with the 180 to 80 Ma range dated for the copper mineralization. Gamma-ray data are consistent with hydrothermal alteration in the sedimentary cover and with the presence of an intrusion in the subsurface. We suggest that the intrusion of the magnetic body generated the necessary thermal energy to mix an already oxidized brine and sulfide-bearing fluids in the border of Parecis Basin, leading to copper deposition and providing a potential analogue for similar environments of mineral deposits elsewhere, such as in the Kupferschiefer deposit (Poland) and Zambia Copper Belt (Zambia).

Keywords: magnetics, modelling, sediment, radiometrics, South America

Reviews of Geophysics

AN AGU JOURNAL

Manuscript #	2016RG000548R
Current Revision #	1
Other Version	2016RG000548
Submission Date	2017-02-01 22:15:57
Current Stage	Contacting Potential Reviewers
Title	Airborne gamma spectrometry method in exploration geophysics: A review
Running Title	Gamma spectrometry method in exploration
Manuscript Type	Review Article
Special Section	N/A
Corresponding Author	Vanessa Ribeiro (UFPE)
Contributing Authors	Murray Hoggett (University of Birmingham), Vinicius Abud Louro (Universidade de São Paulo)
Abstract	<p>The gamma spectrometric method is an important geophysical exploration technique with widespread applications in the geosciences, from local environmental applications to regional geologic mapping. The method has evolved over several decades and recent advances continue to present new outbreaks in instrumentation, data processing and interpretation.</p> <p>Radioelement concentrations measured by gamma-ray spectroscopy reflect the mineral composition of an outcrop. However, magmatism, erosion, hydrothermal activity and/or tectonic events can significantly change the gamma signature. This work explores how different processes affect the emission of radioelements and how information can be extracted from this. The radiometric response of several geological terrains with different tectonic histories were compared, whereas radiometric signatures of granitic intrusions, alluvium regions, craters and shear zones were demonstrated. The results show how the gamma spectrometric method can contribute significant information, can complement and go beyond the superficial geology.</p>
Associate Editor	Assigned
Keyword(s)	Radioactivity methods, Airborne gamma spectrometry, Data processing and interpretation
Index Terms	0932, 0910, 0994
Funding Body Archiving Mandates	No Funders
Data Policy	The authors comply with AGU's data policy, and a statement is included in the acknowledgements identifying where readers can access the data.
Supporting Information (SI)	No
Key Points	<p>Please state the three key points of the article.</p> <p>Main point #1: (140 character limit including spaces) Brief review of radiometric data processing and interpretation and examples of possible errors related with incorrect processing.</p> <p>Main point #2: (140 character limit including spaces) Analyze both how and why the radiometric response can vary for the same deposit and the type of information that can be extracted</p> <p>Main point #3: (140 character limit including spaces) Characteristic signature of a number of targets, which may allow composition of a database to identify possible new targets worldwide</p>
File Permissions	Have you reproduced or modified any part of an article that has been previously published or submitted to another journal? No
Embargo	

Manuscript Items

- Response to Reviewers "Response to Reviewer" [PDF \(70KB\)](#)
- Merged File containing manuscript text and 15 Figure files. [PDF \(51967KB\)](#)
 - Article File [PDF \(24999KB\)](#)
 - Figure 1 [PDF \(1935KB\)](#)
 - Figure 2 [PDF \(356KB\)](#)
 - Figure 3 [PDF \(1232KB\)](#)
 - Figure 4 [PDF \(3787KB\)](#)
 - Figure 5 [PDF \(2128KB\)](#)
 - Figure 6 [PDF \(3880KB\)](#)
 - Figure 7 [PDF \(569KB\)](#)
 - Figure 8 [PDF \(322KB\)](#)
 - Figure 9 [PDF \(5421KB\)](#)
 - Figure 10 [PDF \(2884KB\)](#)
 - Figure 11 [PDF \(560KB\)](#)
 - Figure 12 [PDF \(987KB\)](#)
 - Figure 13 [PDF \(551KB\)](#)
 - Figure 14 [PDF \(699KB\)](#)
 - Figure 15 [PDF \(1403KB\)](#)
- Parsed Citations [Parsed Citations](#)
- Article Tracked Changes "Article - Tracked Changes" [PDF \(24512KB\)](#)

[Previous Decision Letter \(Blind reviews at bottom of letter\)](#)

More Manuscript Info and Tools

- [Send Manuscript Correspondence](#)
[Check Status](#)



Terms of Service
 Licensed under Patent #US
 7,539,000

Copyright ©2001-2014 American Geophysical Union.
[Privacy Policy](#)



1 **Airborne gamma spectrometry method in exploration geophysics: A review**
2
3

4 **V. B. Ribeiro^{1,3}, M. Hoggett², V.H.A. Louro^{3,4}**
5
6

7 ¹ Universidade Federal de Pernambuco – UFPE. Rua Hélio Ramos, s/n, Cidade Universitária,
8 Recife, Pernambuco, Brazil. CEP 50740-53.
9

10 ² Universidade de São Paulo – USP. Instituto de Astronomia, Geofísica e Ciências Atmosféricas,
11 Rua do Matão, 1226, Cidade Universitária, São Paulo, São Paulo, Brazil. CEP 05508-090.
12

13 ³ University of Birmingham, Edgbaston, Birmingham, UK. B15 2TT
14

15 ⁴ University of St. Andrews. School of Earth and Environmental Sciences, Irvine Building, North
16 Street, St. Andrews, Fife, Scotland, KY16 9AL.
17

18
19 Corresponding author: Vanessa B. Ribeiro (van.biondo@gmail.com)
20
21
22

23 **Key Points:**

- 24 • A brief review of radiometric data processing and interpretation and, for the first time,
25 examples of possible errors related with incorrect processing.
26 • This paper is the first to analyze both how and why the radiometric response can vary for
27 the same deposit and the type of information that can be extracted.
28 • Description of the characteristic signatures of a number of exploration targets, which may
29 allow composition of a database to identify possible new targets worldwide.
30 • Examples described in this work vary from the study of geomorphology and weathering
31 influence, undifferentiated lithologies, mineral, hydrocarbon and geothermal exploration,
32 crustal structure, impact craters, and environmental monitoring.
33

Abstract

The gamma spectrometric method is an important geophysical exploration technique with widespread applications in the geosciences, from local environmental applications to regional geologic mapping. The method has evolved over several decades and recent advances continue to present new outbreaks in instrumentation, data processing and interpretation.

Radioelement concentrations measured by gamma-ray spectroscopy reflect the mineral composition of an outcrop. However, magmatism, erosion, hydrothermal activity and/or tectonic events can significantly change the gamma signature. This work explores how different processes affect the emission of radioelements and how information can be extracted from this. The radiometric response of several geological terrains with different tectonic histories were compared, whereas radiometric signatures of granitic intrusions, alluvium regions, craters and shear zones were demonstrated. The results show how the gamma spectrometric method can contribute significant information, can complement and go beyond the superficial geology.

1 Introduction

The gamma spectrometric method considers the natural decay of K, equivalent Th and U (eTh and eU, respectively) and maps these element's distribution spatially. The method has a broad range of applications, such as: identifying outcropping points of igneous intrusions [Ribeiro, 2014], characterization of undifferentiated intrusions [Ulbrich *et al.*, 2009], mineral prospecting [Fornazzari Neto and Ferreira, 2003; Carrino *et al.*, 2007], study of impact craters [Vasconcelos *et al.*, 2012], environmental studies [Conceição and Bonotto, 2003], oil exploration [Saunders *et al.*, 1987; Lüning and Kolonic, 2003], study of hydrothermal alteration zones [Biondi *et al.*, 2001] and study of radioactive accidents impact [IAEA, 2003].

Although the limited penetration in the first dozens of centimeters, gamma-rays are the most penetrating form of radiation available. The shallow reach makes the gamma-spectrometry a reliable source of data for near-surface geophysical studies. Large scale structural analyses [Nóbrega *et al.* 2011; Ribeiro *et al.* 2013], mineral, oil and gas exploration [Saunders *et al.* 1987; 1993, 1994], astrophysical phenomena [Maziviero *et al.* 2013; Bose *et al.* 2013] and environmental monitoring [Sanderson *et al.* 2004; Rachkovskij and Revunova 2011] are only a few of the fields which the gamma-ray spectrometry has been successfully applied over the last eighty years.

Several minerals of economic interest (such as Au, Zn, Ag, Cu) do not present a strong geophysical signature, but are associated with specific geological processes (such as hydrothermal activity) and thus techniques which can indicate the geological process can provide an important vector for exploration. For example, Ostrovsky [1975] highlights the antagonism in K and eTh behaviors under this activity, and this characteristic was then used by several authors to propose different techniques to enhance the hydrothermal signature in radiometric data, such as F parameter [Gnojek and Prichystal, 1985]. The correct application of F factor techniques can provide an important tool to optimize the exploration of hydrothermal deposits.

Filtering parameters (leveling and microleveling - Hogg, 1979; Paterson and Reeves, 1985; Urquhart, 1988; Minty, 1991] and gridding techniques (such as minimum curvature and kriging - Briggs, 1974; Hansen, 1993] have a direct influence on the final map and can introduce pseudo-anomalies not related with geological structures. Although the correct application of these procedures is a make or break moment for gamma spectroscopy, it is not easy to find